Study on Efficient Control of Charge Transports in Photovoltaics of Lead-based and Lead-free Perovskite Materials

Ashish Kulkarni

A thesis submitted in fulfilment of the requirements for the degree of *Doctor of Philosophy* at the Toin University of Yokohama

SUPERVISOR

Professor Tsutomu MIYASAKA

Graduate School of Engineering, Toin University of Yokohama

2017

CONTENTS

CHAPTER 2 Revealing the Possible Recombination Loss at FTO/TiO_2 by Incorporating Thin Layer of MgO in Lead Halide Perovskite Solar Cells.

- 2.1 Introduction
- 2.2 Experimental methods
  - 2.2.1 Methylammonium iodide synthesis
  - 2.2.2 Device fabrication
  - 2.2.3 Characterization
- 2.3 Results and discussion
  - 2.3.1 Thin film characterization
  - 2.3.2 Photovoltaic performance analysis
  - 2.3.3 Proposed recombination mechanism and open-circuit voltage decay (OCVD) measurement
- 2.4 Conclusion
- 2.5 References

CHAPTER 3 Study The Effect of Various TiO_2 Electron Transporting Materials on $(CH_3NH_3)_3Bi_2I_9$ – A Zero Dimensional Perovskite Material for Photovoltaic Applications.

- 3.1 Introduction
- 3.2 Experimental methods
  - 3.2.1 Methylammonium iodide synthesis
  - 3.2.2 Device fabrication
    - 3.2.2.1 TiO_2 compact layer coating
    - 3.2.2.2 Various TiO_2 mesoporous layer coating
    - 3.2.2.3 Bismuth perovskite ($(CH_3NH_3)_3Bi_2I_9$) and HTM coating
  - 3.2.3 Characterization
- 3.3 Results and discussion
  - 3.3.1 Characterization of $(CH_3NH_3)_3Bi_2I_9$ perovskite on various TiO_2 ETL
  - 3.3.2 Device performance and long-term stability
- 3.4 Conclusion
- 3.5 References

CHAPTER 4 Studying the Effect of Tuned Morphology of Methylammonium Iodobismuthate ($(CH_3NH_3)_3Bi_2I_9$) on the Photovoltaic Device Performance

- 4.1 Introduction
- 4.2 Experimental methods
  - 4.2.1 Synthesis of methylammonium iodide
  - 4.2.2 $(CH_3NH_3)_3Bi_2I_9$ perovskite device fabrication
  - 4.2.3 Characterization
- 4.3 Results and discussion

Chapter 1

Introduction

Abstract

This chapter gives an overview of adverse effect of currently used fossil fuels: a non-renewable energy source, on the environment and health and the importance of renewable energy source. Further it limelight the key sources of renewable energy and the significance of abundantly available solar energy Vs other key renewable energy sources. It also gives a brief introduction to different ways of harnessing solar energy. Further, photoelectric effect, the birth of photovoltaic (PV) technology, different kinds of photovoltaic absorbers, and the stemming history of organic-inorganic lead halide perovskite (OILHP) as light-harvesting material, are discussed in brief. In addition to various device architectures, exceptional optoelectronic properties of OILHP in comparison to already existing photovoltaic materials and widely used neighboring charge extraction layers in perovskite solar cells are introduced. Lastly, the issues in perovskite PV devices and the challenges to overcome the issues, motivation of current thesis work concludes this introductory chapter.

1.1 Use of Non-renewable Energy and the Need for Renewable Energy

The proliferation of world's population from 7 billion to nearly 10 billion by 2030 has been gauged according to a study reported by United Nations.[1] With a day to day increase in population, the global energy consumption is expected to increase by 56% in between 2010 and 2040 which demands large energy generation capacity.[2] Ancient forests and swamps which existed on Earth over 400 million years ago were trapped under multiple layers of rocks and sediments beneath the Earth's surface due to changes in climate and geology resulting in the formation of organic matter. The exposure of immense heat and pressure from the Earth's interior on to the sequestered organic matter for over millions of years physically transformed the original decaying biomass into coal, petroleum, and natural gas which are categorized under fossil fuels.[3,4] The energy content of an energy source is the available energy per unit of weight or volume, and the challenge is to effectively extract and use this energy without significant losses in conversion, transportation or utilization. Thus, the more the energy is consumed; greater is the amount of work accomplished. The energy consumption is at a very high rate in the developed country and developing countries such as India and China began to use more and more energy for nation building developments. Out of world's total power production, 36% accounts for petroleum, 26.4% for coal and 23% for natural gas summing to an 86.4% share for fossil fuels in the primary energy consumption of the world.[5] Processing of fossil fuels comprises of several stages accounting for significant and multiple hazards for health and the environment due to the release of carbon dioxide (CO_2) and other toxic gases during the combustion process. Much of the environmental issues such as global warming, acid rain, oil spills, air quality deterioration etc. we face today results from our over-dependence on fossil fuels.[6] Also, the global average temperature has increased from 0.5-1.1 degrees Fahrenheit (0.3-0.6 degree Celsius) due to the release of CO_2 in the air.[7] Additionally, carbon monoxide, nitrogen oxides, sulfur oxides, and hydrocarbons are also released during the combustion process of fossil fuels and are responsible for the formation of tropospheric ozone, the major constituent of smog.[6] Moreover, people have got aware of the limitations of fossil fuels after 1973 oil crisis and the search for alternative energy sources started, which has triggered most of the researchers towards the development of alternative energy source to avoid

economic chaos by ensuring adequate global energy supply.[8] In order to avoid the most serious consequence by 2050, at least 20 terawatts of carbon-free energy are required.[9]

Any substantial energy source that naturally comes from the environment is termed as renewable energy. The name itself suggests that the source of energy exists perpetually and are in abundant in the environment which can be readily harnessed and are inexhaustible as they can be trapped from the Sun, wind, ocean, hydropower, biomass, geothermal resource, and biofuels whose resources are copiously available in wide geographical areas, in contrast to other energy sources which are concentrated in a limited number of countries.[10, 11] Rapid deployment of renewable energy and technological diversification of energy sources would indeed result in significant energy security and economic benefits. Basically, there are various types of a renewable energy source as shown in the schematic (Figure 1.1).

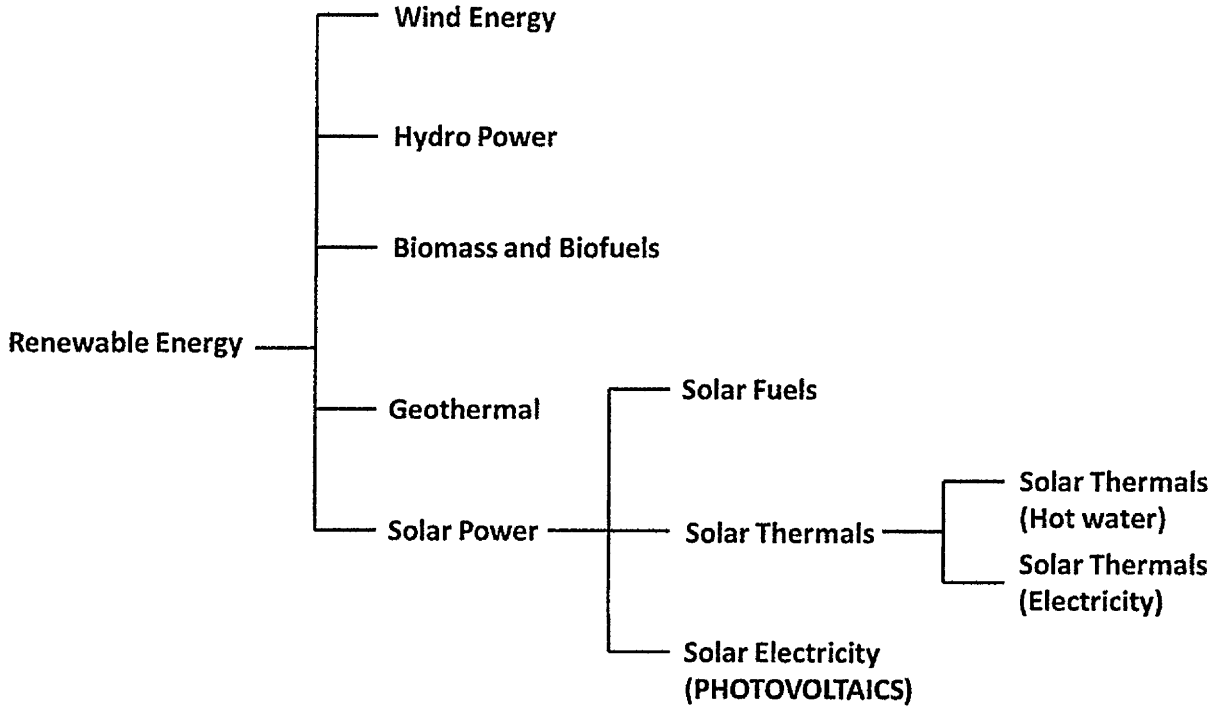

Figure 1.1: Flow-chart showing various kinds of renewable energy.[10, 11]

1.2 Solar Electricity: Photovoltaics

1.2.1 Solar radiation

The Sun – our nearest star – is by far the most abundant source of energy. However, it has been merely 200 years since it was realized that it can be used to create the electricity. Every hour Earth receives 4.3 x 10^{20} J of energy from the sunlight out of which 4.1 x 10^{20} J of solar energy is used every year indicating a huge gap between the Earth receiving and present usage of solar energy.[12] The Sun can be perceived as a black-body which emits at T~5500 K following the Planck's law. Solar radiation spectrum stretches out from the X-rays up to the radio waves with its peak at 525 nm (2.36 eV). However, the main fraction of the wavelength lies between 100 nm to 1 mm – where half of the light is in the infrared region and from the other half 40% and 10% accounts to visible light and ultraviolet respectively. Various layers of the atmosphere, though, protects the Earth's surface from the excessively high energy radiation it eventually affects the shape of solar spectrum as shown in Fig. 1.2 which are mainly caused by three effects:

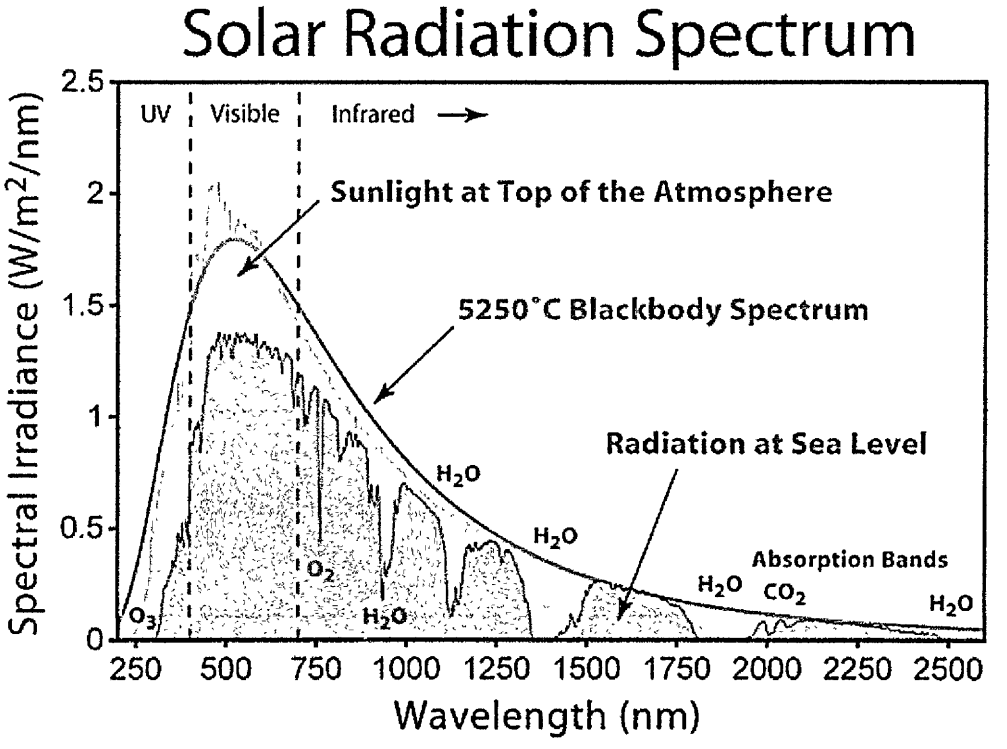

Figure 1.2: A comparison of black-body radiation at 5250 ^{O}C (grey line) with the solar irradiance spectrum, at the top of the Earth's atmosphere (yellow) and after passing through the atmosphere (red).

1. Scattering by aerosols, e.g. dust particles.
2. Telluric absorption: basically termed as molecular absorption – H_2O, CO_2, water vapour, O_2, CH_4, N_2O and fluorinated hydrocarbons which absorb in the infrared and ozone (O_3) that absorbs in the ultraviolet.
3. Rayleigh scattering by air molecules (which is the reason for the blue colour appearance of the sky).

The attenuation depends on the path length and the coefficient which defines this optical path length is called air mass (AM) (Equation 1.1)

$$AM = l/l_o \sim 1/\cos z' \quad (1.1)$$

l_o = path length normal to Earth's surface at sea level

z = zenith angle

Solar irradiation outside the atmosphere value is assigned as AM0 and AM1 is referred to the Sun shining directly overhead at the sea level ($z = 0^O$, the thickness of one atmosphere). AM1.5, another important value, corresponds to the zenith angle of 48.2^O and at this Sun irradiation angle, most of the humans' habitats are situated. Thus it represents the overall yearly average solar irradiation. Therefore, performing photovoltaic measurements at AM1.5 solar spectrum ought to sun spectrum which is very close possibility to the reality.

1.3 Photoelectric or photovoltaic effect

At the age of 19, Alexandre-Edmond Becquerel discovered the photovoltaic effect – a silver coated platinum electrode immersed in the electrolyte generated photovoltage and photocurrent. Later on, this effect was widely studied using different materials such as selenium (Se), lead sulfide (PbS), copper oxide films etc. Today most popular photovoltaic devices are based on semiconductors based on p-n (p-positively doped and n-negatively doped) junctions (Fig. 1.3). There are no net current flows when two pieces of oppositely doped (p and n) semiconductors are brought to an intimate contact (thermal equilibrium and with no external bias), however, there exist two balanced currents of the majority charge carriers induced by diffusion. The flow of the majority carriers lead to the equilibration as the Fermi level in each type of the semiconductors are different and thus forming a difference in potential which is termed as *built-in-potential*. Due to the displacement of charges and exposition of the stationary charges, the electric field will continue to flow and inhibits the current flow. *Space-charge region* is the thin layer in which majority of the

charge carriers diffuse out to the outer side and within this region, an exciton (electron and hole pair) is generated upon the photon absorption and the effective separation of charges occurs thanks to the electric field, allowing for the drift as shown in Fig. 1.4

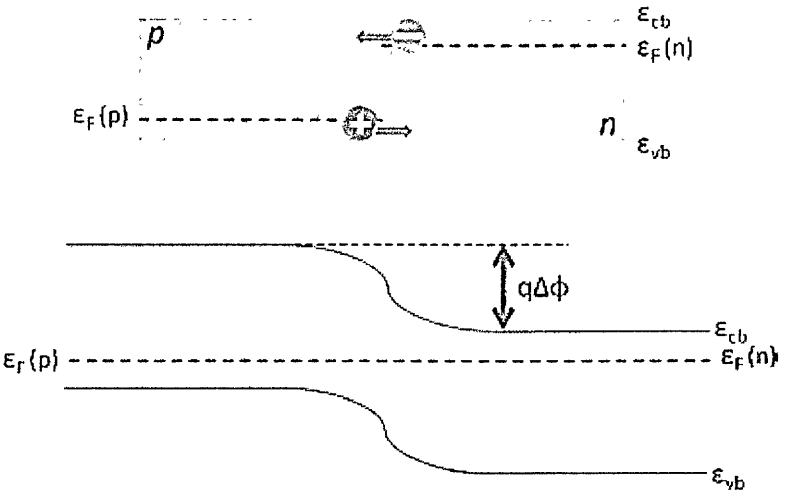

Figure 1.3: Above: n- and p-type semiconductors in contact. Majority charge carriers diffuse through the junction in opposite directions – no net current is observed. Below: The creation of the uniform Fermi level throughout the material results in the generation of the built-in potential.

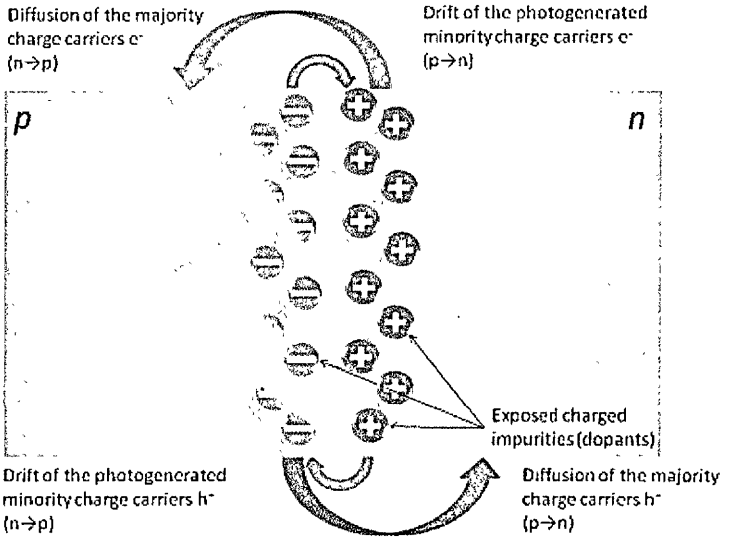

Figure 1.4: p-n junction after the absorption of a photon: the arrows show the types and directions of the currents flowing through the junction.

1.4 Evolution of photovoltaic systems

In 1883, Charles Fritts constructed first solar cell by depositing gold (Au) on Se layer with efficiency below 1%. Later the concept of conversion of abundant and free sunlight to electricity was revisited during the golden era of quantum mechanics and a Polish scientist, Jan Czochralski, developed a method to grow ultrapure silicon (Si) semiconductor crystals. However, the photovoltaic field bloomed in 1950's when Bell Laboratories demonstrated first modern semiconductor cell based on p-n junction. The research further enthused with the "space-race" and solar energy was found to be an ideal solution for powering the satellites. In early days, in 1978, Bell Laboratories introduced calculators based on solar energy and today photovoltaic technology is not only used to supply electricity to small portable devices but whole solar power plants are being constructed in many places around the world. Though silicon solar cells are for now ruling the market of the solar industry, researchers have developed new materials, road mapped and conceptualized the way to stop wasting the free abundant energy. The current record efficiencies of solar conversion technologies that have been developed to date are presented in Fig. 1.5 and their brief introduction are described below.

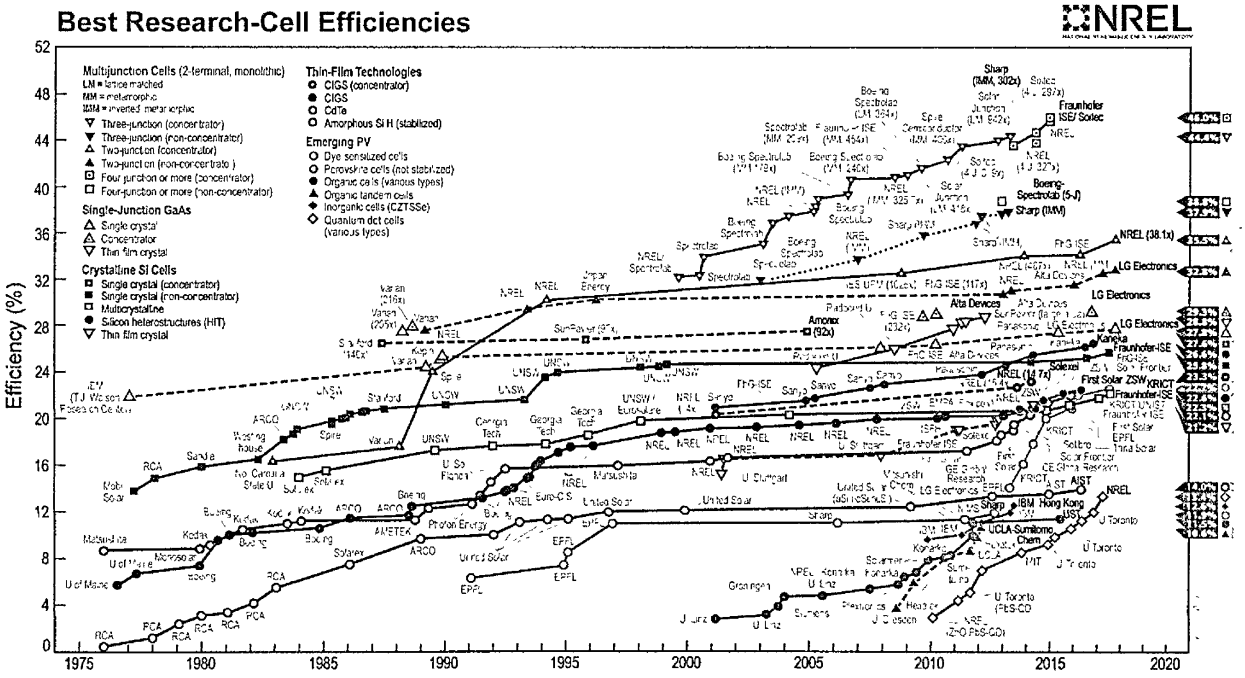

Figure 1.5: NREL chart showing record efficiencies to date various solar conversion technologies.

Depending on the type of the absorbing material used, type of junction formed, manufacturing techniques adopted, the photovoltaic technologies have been broadly categorized into (also depicted in flow chart (Fig. 1.5))

a. 1st generation solar cells: Classic solar cells, Si, GaAs
b. 2nd generation solar cells: Thin film technologies.
c. 3rd generation solar cells: Emerging low cost, simple processable technologies.

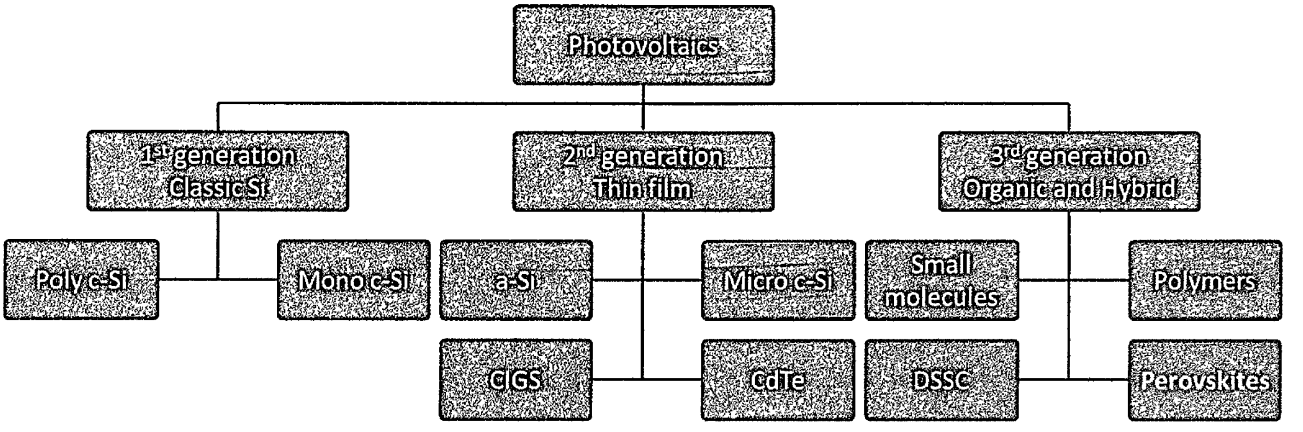

Figure 1.5: Flowchart representation of various generations of photovoltaic technologies.

1.4.1 1st generation solar cells: Classic solar cells

This is the most established, robust and efficient solar cell technologies till date in which pure single crystals of silicon (Eg = 1.1 eV) based solar cells are fabricated by Czochralski's method reaching efficiencies up to ~25% (reaching almost the theoretical limit of ~29%).[13, 14] Even though they possess several advantages such as longevity, greater heat resistance and ability to generate more electricity, the cost of crystal growth and subsequent material loss during the cutting of the ingots are too large, this makes it very expensive. Additionally, the Czochralski's method is highly tedious and suffers from high production cost.[15] To date, GaAs single crystal solar cell is the most efficient one with efficiency reaching up to 26.4%. This material is used almost exclusively for extraterrestrial application due to its high production costs. The use of less pure multi-crystalline Si would

reduce the cost; however, the efficiencies are much lower due to a highly disordered structure which provides more recombination channels.

1.4.2 2nd generation solar cells: Thin film technologies

In order to reduce the costs of material production and device fabrication the new, natural concept of employing thinner, polycrystalline layers emerged.[16, 17] The thickness range of thin film based solar cell varies from nanometers (nm) to tens of micrometers (μm). In addition to amorphous silicon (a-Si), the range of applications has been expanded to CdTe, Cu(InGa)Se2 (CIGS) or Cu2ZnSn(SSe) (CZTS) and they can be obtained with simplified manufacturing process in contrast to 1st generation solar cells thus reducing cost. Also, with the content of Ga, the band gap can be tuned ranging from 1.04 eV to 2.4 eV. Among all the explored material CIGS is an indubitable leader, reaching a conversion efficiency of 20.4% while the a-Si shows lower performance (13%)[16] mainly because of persisting problems with degradation upon exposure to light. However, to date, the origin of this phenomenon is not very clear and it is suspected that escape of hydrogen bind from the material leads to dangling (unsaturated bonds). Continuous light illumination accelerates this process leading to increasing in the density of defects, and as a result, leads to increasing in recombination current (Staebler-Wronski effect).[18]

1.4.3 3rd generation solar cells: Emerging technologies

This generation categorizes photo-electrochemical devices involving photo excitations and electrochemical reactions. Few new approaches have entered the photovoltaic arena with the blossom of nanotechnology, material science and abundant materials which further reduces manufacturing process and cost. The efficiency (%) vs cost (US$/m2) plot of solar electricity costs as a function of module electricity is shown in Fig. 1.6

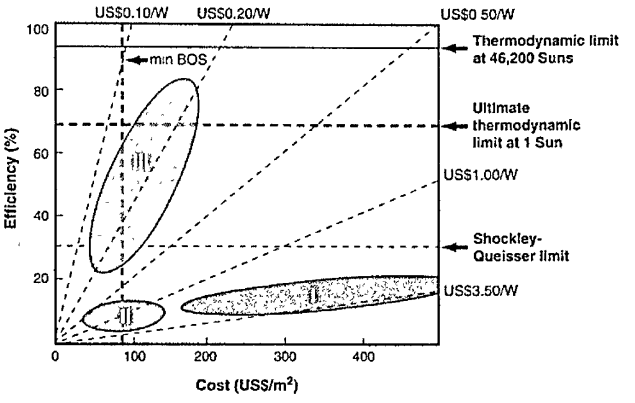

Figure 1.6: Solar electricity costs as a function of module efficiency and costs.[19]

The shift from crystalline and a-Si to organic small and polymeric materials manifested itself in organic solar cells. This concept is based on the conjugated system who's spatially distributed energy levels (HOMO and LUMO) resembles a conduction and a valence band in a classic semiconductor. The conversion efficiency in this system went up to 11.5%, however, minor charge diffusion length and poor stability remain as a major issue.[20, 21] Further, the concept of dye-sensitized solar cells was also developed based on Nature's principle of photosynthesis. The chemical way of depositing device stacking layers and assembling the cell architecture allows facile and cost-effective processing which further reduces the cost in comparison to 1st and 2nd generation solar cells. Liquid electrolyte and the solid-state hole transporting material (HTM) are employed as a p-type material. To date, the best efficiency recorded ~13% using cobalt redox shuttle as the electrolyte.[22] However, evaporation of liquid electrolyte and poor performance of solid-state DSSC are major drawbacks.

In 3rd generation solar cells, the champion is irrefutably a perovskite solar cell, to which this thesis is devoted in its entirety.

1.5 Perovskite solar cells:

Inorganic lead halide perovskites have been studied since the nineteenth century while organic-inorganic halide perovskites have been of interest since the early twentieth century.[23, 24] In 1978 after Weber reported two perovskite hybrid halide compounds,

$CH_3NH_3PbX_3$ ($X = Cl^-, Br^-, I^-$) and $CH_3NH_3SnBr_{1-x}I_x$, much of the research work were carried out in context of their usual chemistry and physics[25] with the first report on solar cell appearing in 2009.[26] Perovskite solar cell (PSC) is a photo-electrochemical device in which carrier generations occurs within the active layer in the presence of light which is separated in n- and p-type transporting layer and are finally collected at the back electrodes, respectively. Perovskite possesses exceptional optoelectronic properties ideally suitable for photovoltaics such as long carrier diffusion length, low exciton binding energy, high extinction coefficient, photon recyclability, ambipolar charge mobility, low lying valance band which attributes to high voltage and compatibility with simple solution process all of which contribute to a widespread fascination for PSCs.[27, 28, 29, 30, 31]

1.5.1 Historical background of Perovskites:

Perovskite is a type of mineral that was first found in the Ural Mountains and named after Russian mineralogist Lev Perovski who discovered it. In 1839 Gustav Rose discovered the crystal structure in calcium titanate ($CaTiO_3$) which consist of TiO_6^- octahedral sharing corner of the unit cell with Ca^{2+} occupying the cubo-octahedral cavity and from then on, all the materials possessing crystal structure of $CaTiO_3$ was known as perovskites. Perovskite material possesses a general formula of AMX_3 where M is the metal cation in the center of corner-sharing MX_6 octahedral network whereas X and A are oxides or halide anions and cations in the interstices respectively as shown in Fig. 1.7.

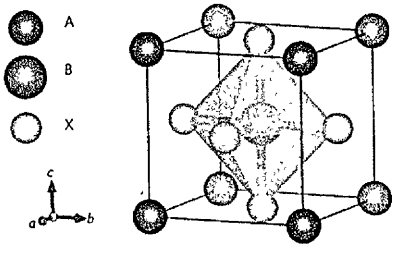

Fig. 1.7: AMX_3 perovskite crystal structure.

Basically, perovskite possess cubic geometry phase, however at lower temperature distortion of MX_6 octahedra takes place and lower symmetric structure of orthorhombic or tetragonal phase is formed. Optical and electronic properties of perovskite material are highly dependent on the size of each component, that is, changes in the M-X bond strongly

affects the bandgap as it is very sensitive to the MX_6 octahedral network. "A" component acts to neutralize the total charge within the lattice and is not a critical motif to determine the band structure. Additionally, A cation size governs the lattice expansion and contraction. In other words, the distortion and stability of perovskite crystal structure is assessed by tolerance factor, *t*,

$$t = \frac{r_A + r_X}{\sqrt{2}(r_M + r_X)}$$

Where r_A, r_X and r_M are the radius of A, X and M, respectively. The cubic phase is stabilized when the tolerance factor equals to 1 and when it deviates from 1 then the distortion of octahedral three-dimensional framework (AMX_3) is expected and forms two- and lower-dimensional structure instead.

Three dimensional organic-inorganic hybrid lead halide perovskite (OLHP) which also possess a general formula of AMX_3, where A = $CH_3NH_3^+$, Cs^+, M = Pb^{2+}, Sn^{2+}, Ge^{2+} and X = Cl^-, Br^-, I^-, were explored intensively by Mitzi et al.[32, 33] The lattice structure, material bandgap, optical and electronic properties of (OLHP) can be tuned by changing the alkyl group, central metal ions and halides. The aforementioned advantages make them flexible to versatile applications such as field effect transistors,[32] electroluminescent devices,[33] LEDs, water splitting etc. Currently, OLHP has attracted substantial attention in photovoltaic application because of their tunable optical and electronic properties, long carrier diffusion length, ambipolar charge mobility, high extinction coefficient, and above all due to the simple solution fabrication process which allows facile device engineering protocols.[27-31]

1.5.2 Development of perovskite solar cells:

Streaming from the field of DSSC, in 2009, the first device architecture incorporating $CH_3NH_3PbX_3$ (X = I^- and Br^-) was reported by Miyasaka et al. combining with liquid-electrolyte based system.[26] This work demonstrated tunable optical property of $CH_3NH_3PbX_3$ as high open-circuit voltage (V_{oc}) of 0.96 V was achieved by using bromide perovskite in contrast to iodide perovskites and power conversion efficiency (PCE) of 3.8% and 3.1% were obtained by using $CH_3NH_3PbI_3$ and $CH_3NH_3PbBr_3$ respectively.[26] Although

the PCE was high in comparison to quantum dot solar cells, the poor lifetime was a major drawback. In subsequent years, Park et al. increased the weight percent of the precursor components along with lead nitrate surface modification with which the efficiency improved to 6.54%.[34] Perovskite and liquid electrolyte interfacial modification by thin aluminum oxide (Al_2O_3) layer prevented the perovskite corrosion by the electrolyte and improved the stability.[35] Despite many efforts, the PCE was poor compared to DSSC as liquid electrolyte causes perovskite corrosion or dissolution and this inevitably became an obstacle to improving the efficiency.

In 2012, a major breakthrough was accomplished by Miyasaka et al. and Park et al. independently in terms of efficiency and stability by replacing liquid electrolyte with widely used 2,2',7,7' –tetrakis(N,N-p-dimethoxy-phenylamino)-9,9'-spirobifluorene (spiro-OMeTAD) – a solid state HTM. Miyasaka et al. incorporated mixed halide perovskite system, that is, $CH_3NH_3PbI_{3-x}Cl_x$ in both mesoporous TiO_2 and Al_2O_3 meso-superstructure architecture and surprisingly higher efficiency of 11% was obtained in the device incorporating Al_2O_3 layer.[36] On the other hand, Park et al. incorporated $CH_3NH_3PbI_3$ as a light absorbing layer with 600 nm TiO_2 mesoporous layer and the device showed conversion efficiency of 9.7% with long-term stability up to 500 hours.[37] These two results made a remarkable move into research of perovskite solar cells which ignited the perovskite storm. With the advantage of various device architectures, perovskite material properties, simple device fabrication protocols, last five years witnessed an unprecedented rise in conversion efficiency of perovskite solar cell with a recently certified value of 22.7%.

1.6 "A" site substitution in AMX_3 – A path towards tuning the dimensionality:

Structural dimensionality, optical and electronic properties, and stability of the material are highly governed by monovalent cation (A) in AMX_3 perovskite structure. Due to the cubo-octahedral cavity, in 3D perovskite structure, only small organic/inorganic cations can be intercalated. Maximum ionic radii for the organic/inorganic cation with stable structure can be governed by Goldschmidt tolerance factor (t). The tolerance factor for cubic perovskite phase ranges from 0.78 to 1.05 as it can tolerate slight expansion due to the distorted structure. Widely studied methylammonium (MA) lead iodide ($CH_3NH_3PbI_3$) perovskite has tolerance factor of 0.91 and is slightly distorted while replacing MA with

formamidinium (FA) shifts the tolerance factor value to 0.99 which is nearly perfect cubic.[38] The monovalent cation acts as a charge compensation part in the crystal lattice and does not have any contribution to the band structure of the material. The size of cation plays a crucial role as it can affect the optical properties as the size of cation causes changes in M-X bond length with which the bandgap of the material changes. In order to fit corner sharing metal octahedral cavity, the size of cation "A" may not be larger than 2.6 Å. Incorporation of large size cation can lead to the formation of lower dimensional or confined perovskite structure.

To date, MA^+, FA^+, potassium (K^+), cesium (Cs^+), rubidium (Rb^+) have been incorporated to form stable 3D perovskite phase and among all Cs^+ possess smallest ionic radius in contrast to other cations and has absorption at a lower wavelength.[39]

1.7 "X" site substitution in AMX_3 – A path towards tuning the bandgap:

The bandgap of the perovskite material can be tuned in complete visible spectra by partial or complete substitution of halide ions from I^- to Br^- and Cl^- and the difference in lattice constant is determined by moving from Cl^- to Br^- ions. The bandgap of the material is tuned majorly due to increase in covalent bonding nature of halogens which leads to increase in electronegativity. Additionally, the combination of I^- and Cl^- halide shows no shift in the bandgap, which clearly signifies that in PbI_6 octahedron Cl^- cannot replace iodine.[39]

Complete substitution of I- with Br- widens the bandgap of the material leading to a reduction in conversion efficiency for bromide based perovskites. However, the bandgap of bromide perovskite is quite suitable for tandem structure and light emission applications and they also possess long carrier diffusion length, low exciton binding energy, and energy level matching with TiO_2. On the other hand complete substitution of I- with Cl- leads to increase in bandgap up to ~3.1 eV which restricts its application as a single light absorber.[40] Table 1.1 summarizes the charge transport bandgap (E_g) along with optical bandgap (E_{opt}) and exciton binding energy of various halide ion substituted perovskite materials. Table 1.1 also significantly evidences that $MAPbI_3$ has the optimum bandgap closer to Shockley-Queisser limit.

Table 1.1: Comparison between charge transport bandgap (E_g) and optical bandgap (E_{opt}), with exciton binding energy.

Halide substitution	Δ (eV)	E_g (eV)	E_{opt} (eV)
$MAPbI_3$	0.18 ± 0.1	1.6	1.52
$MAPbBr_3$	0.48 ± 0.11	2.3	1.84
$MAPbI_{3-x}Br_x$	0.16 ± 0.1	1.96	1.8
$MAPbCl_3$	0.12 ± 0.12	3.09	2.97
$MAPbI_{3-x}Cl_x$	0.04 ± 0.11	2.64	2.6
$MAPbBr_{3-x}Cl_x$	0.14 ± 0.14	2.58	2.44

1.8 "M" site substitution in AMX_3 – A path towards lead (Pb) free perovskite solar cells:

On the front of Pb replacement, tin (Sn) based perovskite have been demonstrated as the first step with an initial efficiency of 5.7% and now scaled up to ~6.4% in pure Sn and ~15% in Pb-Sn mix perovskite system.[41, 42] Even though Sn perovskites have shown promising optoelectronic properties such as long diffusion length, superior electron mobility (~2000 $cm^2\ V^{-1}\ s^{-1}$) than traditional semiconductors such as CdTe and Si, narrow optical band gap with potential to absorb light up to 1000 nm and bulk n-type electrical conductivity (5 x 10^{-2} S cm^{-1}), Sn perovskite exhibits multivalent features i.e. it gets oxidizes in its +4 stable oxidation state, from +2, when exposed to ambient air and due to this unstable oxidation state the device fabrication has to be carried out in inert atmosphere. Additionally, the oxidized Sn^{+4} ion acts as a p-type dopant within the bulk perovskite layer causing self-doping effect and thus limiting PCE.[43] Moreover, reports have shown that Sn perovskite can be even more toxic than lead perovskite due to the release of a high amount of hydroiodic acid (HI) into the environment as a byproduct than its counterparts.[44] Germanium (Ge), another Group 14 metal, also found its place in perovskite family and has demonstrated high ionic conductivity than Pb and Sn perovskites.[45] Among all the studied Ge based perovskite only $CsGeI_3$ possess an optical band gap of 1.6 eV and incorporation of other halide ions and organic cation leads to significant widening of band gap above 2 eV. Due to the low

binding energy of its $4s^2$ electrons, alas Ge perovskite is also sensitive and becomes unstable when exposed to air and thus limiting its PCE.[45] In 3-D AMX_3 perovskite crystal structure, X-M-X bond plays an important role in determining the bandgap of the material. The bond angles for Pb, Sn and Ge are measured to be 155.19 $(6)^O$, 159.61 $(5)^O$, 166.27 $(8)^O$ respectively and $APbI_3 > ASnI_3 > AGeI_3$ is the trend for decreasing the bandgap for different metal cation based perovskite materials.

Bismuth (Bi) is the only non-toxic 6p-block element having an outer lone pair of $6s^2$ electron same as lead (Pb).[46] Ternary non-toxic metal halides based perovskite materials ($A_3M_2X_9$; A = Cs^+, MA^+, Rb^+; M = Bi^{3+}, Sb^{3+}; X = I^-, Cl^-) have emerged recently as potential candidate due to its non-toxicity and high moisture stability.[46, 47] Optical properties, crystal structure, dielectric studies and quantum physical properties of various ternary bismuth halide perovskite materials have been formerly investigated but attempts to use it in photovoltaic devices was lately addressed. On the other hand non-perovskite bismuth halide (BiI_3) and perovskite-like cubic silver-bismuth halide (Ag-Bi-I) light absorbing material based solar cells have also attracted recent attention due to their promising optoelectronic properties and suitable band gap for single junction and/or for the tandem solar cell.[48, 49] More details about $A_3M_2X_9$, BiI_3 and Ag-Bi-I materials will be discussed in their subsequent chapters.

1.9 Deposition process for lead and bismuth perovskite materials:

Initial work by Miyasaka et al. offered a significant breakthrough for the rapid development of perovskite solar cells. Current outstanding recorded power conversion efficiency (PCE) and low production cost suggest that perovskite solar cell could be next-generation photovoltaics. Tracking back to the evolution of perovskite solar cells, the reproducibility and photo-electrochemical properties of the devices are highly determined by the morphology and grain growth of the perovskite layer. The perovskite deposition techniques are mainly categorized into 1) One-step deposition process (ODP) and 2) two-step deposition process (TDP). Organic and inorganic precursor components are deposited simultaneously in ODP while in TDP, the precursor components are deposited in sequence.

1.9.1 One step deposition process:

At the early stage of perovskite research, one-step deposition process was commonly used. In this deposition process, equimolar ratio of lead iodide (PbI_2) and methylammonium iodide (CH_3NH_3I) is dissolved in a polar solvent such as N,N-dimethylformamide (DMF) or dimethyl sulfoxide (DMSO) to form a precursor solution which is then deposited on different kinds of substrates such as quartz, sapphire, silicon, plastic or FTO/glass substrate. However, many studies reported island-like morphology of as-prepared $CH_3NH_3PbI_3$ in addition to low surface coverage.[50] Additionally, substrate temperature, type of solvents and rotation speed are the parameters controlling the crystal growth and morphology of the perovskite. In order to obtain the desired thickness of perovskite layer with one step deposition process, the concentration of precursor solution can be modified while keeping the all the other parameters fixed. Snaith et al. obtained a pinhole-free layer of perovskite by depositing both inorganic and organic precursor components simultaneously by vapour process. The efficient device of 15.4% was illustrated elucidating uniform and pinhole-free perovskite layer is essential for enhancing the conversion efficiency of perovskite solar cells.[51]

Basically, low nuclei density on the substrate leading to incomplete coverage due to the exaggerated growth of few nuclei was primarily responsible for the poor morphology of perovskite layer by solution process. Therefore, controlling the nucleation rate to modify the perovskite morphology is the key to obtain uniform pinhole free perovskite grains and to effectively improve the device performance. This further paved path towards the study of nucleation behavior and solvent properties which provided further directions for achieving efficient device.

For one step deposition of bismuth perovskite materials, the precursor materials (in an equimolar ratio) are dissolved into DMF and after stirring for 1 hour at 70 ^{O}C the precursor solution is spin-coated followed by annealing step to form a thin film of bismuth perovskite.[52]

1.9.1.1 Anti-solvent drenching method:

Anti-solvent drenching is an approach that induces supersaturation in the solution promoting nucleation at room temperature. In this context, anti-solvent is typically a

nonpolar solvent which has a very low solubility of perovskite precursor but high miscibility for precursor polar solvent. Drenching of an anti-solvent, during the spin coating step of precursor solution, can extract precursor solvent rapidly. Due to which it reduces the solubility of the solutes and an intermediate phase is formed thus boosting the nucleation rate and suppressing the crystal growth of perovskite layer.

To obtain a pinhole-free layer with uniform morphology Seok et al. demonstrated solvent engineering process by drenching toluene during the spin coating process of perovskite precursor solution loaded substrate. This led to the formation of CH_3NH_3I-PbI_2-DMSO, an intermediate complex, which is then converted to uniform perovskite film during the heating step.[53] Concurrently, Cheng et al. demonstrated fast deposition-crystallization by adopting chlorobenzene as an antisolvent, which incubated rapid nucleation of perovskite film rather than formation of the intermediate complex. With this method, large uniform pinhole free grains with full coverage was obtained and devices showed ~17% with high reproducibility.[54] Another approach called solvent-solvent extraction was introduced by Padture et al. who extracted the precursor solvent, prior to heating step, by dipping perovskite coated substrate into the antisolvent (dichloromethane) bath leading to rapid nucleation of perovskite film during the solvent bathing step.[55] In addition to the above-mentioned facts, the anti-solvent scalable method provides another feature of potential scalability of perovskite solar cells.

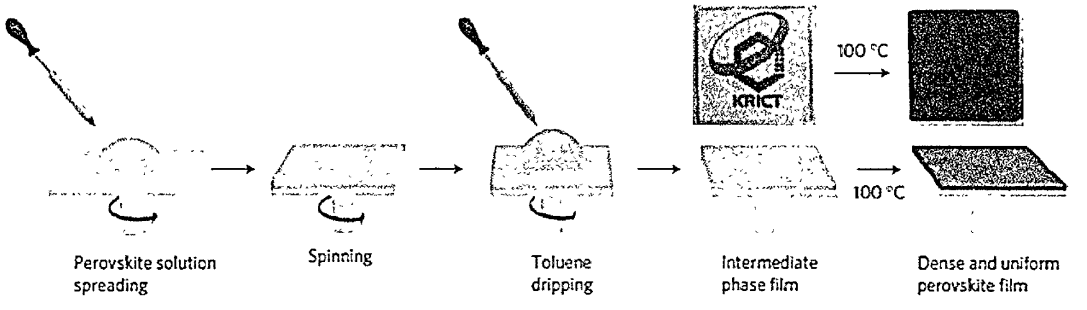

Figure 1.8: Schematic illustration of solvent engineering process for deposition of uniform perovskite thin film.[53]

1.9.2 Two-step (sequential) deposition process:

In two-step deposition process, the inorganic and organic precursor components are deposited in sequence either by solution or vacuum process. In 1997, Mitzi and coworkers developed the two-step deposition method which provides simplicity and versatility of perovskite layer deposition. In their studies, they first deposited inorganic component layer by vacuum process on to the substrate followed by immersing them in organic ammonium cation solution for a short period of time leading to the formation of perovskite layer.[56] In 2012, Grätzal and coworkers introduced this two-step deposition process for preparing perovskite solar cells.[57] In this process, the concentration of organic salt and dipping time are very crucial and stoichiometry of the precursor components does not play any significant role in determining the performance of the device. Most importantly, in contrast to one step deposition process, two-step deposition process can be performed in relative humidity of 40% atmosphere.

1.9.2.1 Two-step dip coating method:

Grätzal and coworkers deposited $CH_3NH_3PbI_3$ film by spin coating PbI_2 layer dissolved in DMF followed by dipping the PbI_2 coated substrates into CH_3NH_3I containing the 2-propanol solution. The reaction between PbI_2 and CH_3NH_3I resulted in the transition of film colour from yellow to dark brown. With this approach first certified efficiency of 15% was reported. Although with this process complete conversion of PbI_2 to perovskite was not achieved.[57] In subsequent years, Han et al. replaced solvent DMF with DMSO to dissolve PbI_2 which retarded the crystallization of PbI_2 by forming PbI_2-DMSO complex which led to complete conversion of PbI_2 to $CH_3NH_3PbI_3$ after dipping in CH_3NH_3I/IPA solution for 10 minutes. The resultant film obtained with this approach composed of uniform, pinhole free perovskite crystals further demonstrating the efficiency of ~17%.[58]

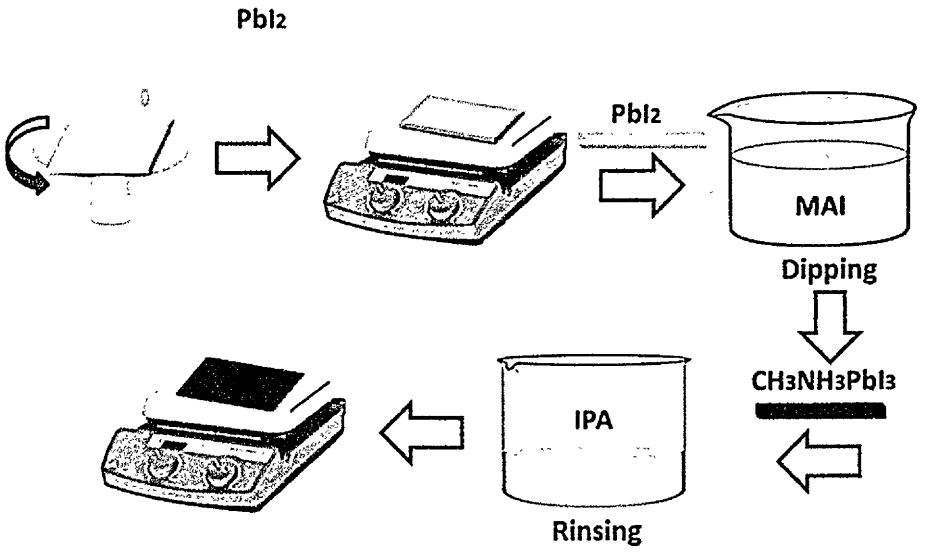

Figure 1.9: Schematic illustration of two-step (sequential) dip coating technique for perovskite deposition.

1.9.2.2 Two-step spin coating process:

This process is analogous to sequential deposition method which replaces the dipping step with spin-coating with short period (20-30 sec) of loading time. Park et al. initially introduced this process and demonstrated device efficiency of 17% with high reproducibility. Although two-step spin coating process and sequential deposition process has no much significant difference between them, research reports claimed that gaps between the crystals can be filled with the spreading flow of CH_3NH_3I/IPA solution under the action of centrifugal force leading to sufficiently connected and dense perovskite capping layer. Figure 1.10 depicts the schematic illustration of two-step spin coating process.[59]

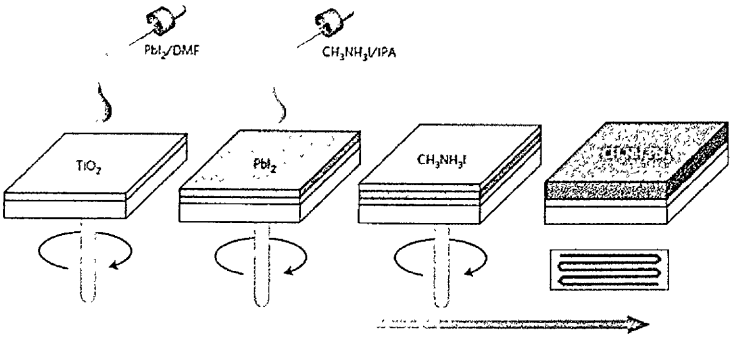

Figure 1.10: Schematic illustration of two-step spin coating process for perovskite deposition.[59]

1.10 Device architectures:

1.10.1 Mesoporous cell architecture:

Mesoporous cell architecture which is widely employed to fabricate organo-lead halide perovskite solar cells is composed of a complete p-i-n junction with perovskite infiltrated within an n-type mesoporous layer as shown in Fig. 1.11. Initially, a dense compact electron transporting layer is deposited on the top of fluorine doped tin oxide (FTO) or indium doped tin oxide (ITO) coated glass substrate. Titanium dioxide (TiO_2) is widely employed n-type electron transporting material which is deposited either by spray pyrolysis[60] or spin coating the precursor solution such as titanium isopropoxide or titanium diisopropoxide bis(acetylacetonate) solution in 2-propanol or ethanol. Other methods such as atomic layer deposition and chemical bath deposition[61] have also been demonstrated in the various literature. Deposition of pinhole-free and uniform compact electron transporting layer is crucially important because its main purpose is to prevent recombination between perovskite and FTO.[62] Due to the merits of high conductivity and low-temperature process other electron transporting materials such as TiO_x, SnO_2,[63] ZnO has also been explored as an alternative electron transporting materials.

TiO_2 mesoporous layer is deposited on top of the dense compact layer by spin coating a nanoparticle TiO_2 paste followed by sintering to remove the binders and additives. Perovskite material and other light absorbing materials are then deposited by the spin-coating process to infiltrate the porous structure and form an over capping layer. The hole

transporting material (HTM) is deposited above the perovskite layer which completes a p-i-n junction. Small organic molecules and polymers such as spiro-OMeTAD,[57] poly 3-hexylthiophene (P3HT)[64] without and with appropriate dopants are commonly used HTMs and are deposited by a spin-coating process. Finally, a metal electrode is thermally evaporated on the top to complete the cell. To date, perovskite device based on mesoporous architecture showed conversion efficiency of 22.1%.[65]

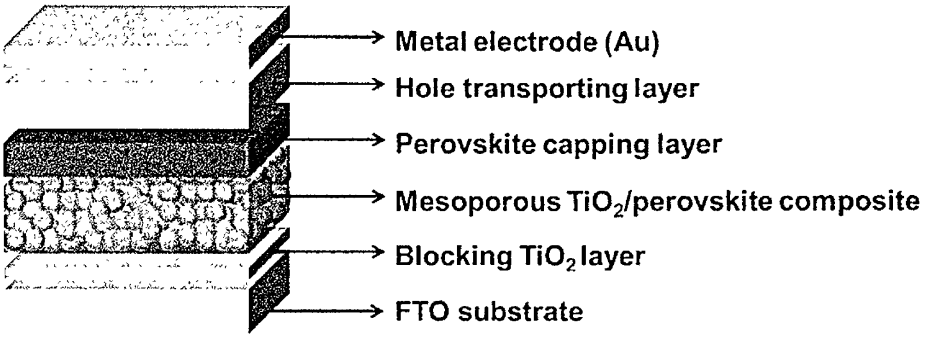

Figure 1.11: Schematic depiction of mesostructured perovskite solar cells.

1.10.2 Meso-superstructured cell architecture:

Miyasaka and co-workers pioneered meso-superstructured architecture by replacing commonly used semiconducting TiO_2 mesoporous layer with insulating aluminum oxide (Al_2O_3).[66] The key feature of the meso-superstructured architecture is that Al_2O_3 acts only as a scaffold layer rather than involving in charge separation or carrier injection. A wide variety of insulating layers such as zirconium oxide (ZrO_2)[67] can also be employed as a scaffold layer. In addition to aforementioned advantage, the merit of using nanoparticle suspension as a precursor solution allows deposition of scaffold layer relatively at low temperature (<150 ^{O}C).[68] However, in this case, mixed halide perovskite, $CH_3NH_3PbI_{3-x}Cl_x$, was employed due to its higher carrier diffusion length in comparison to pristine iodide perovskite.[29] Later on researchers have demonstrated high efficiency up to ~16% which further indicated that Al_2O_3 acts as a buffer layer inhibiting leakage current between two electrodes. This approach confirmed efficient self-electron transport ability of perovskite itself in addition to charge generation within the inner porous structure.

Advantageously, high V_{oc} can be obtained with this architecture which is attributed to low fundamental loss during charge transport. Also, Bisquert at al. disclosed that charge carriers accumulate in the perovskite layer which can probably be another reason for higher V_{oc} contrasting mesoscopic device architecture.[69] The schematic illustration of meso-superstructured device is depicted in Fig. 1.12.

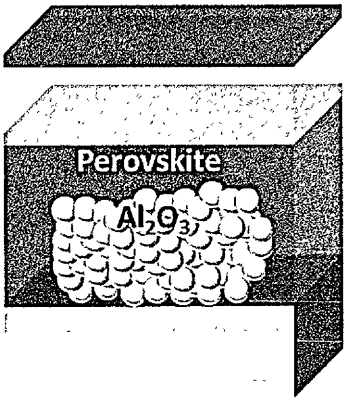

Figure 1.12: Schematic representation of meso-superstructured perovskite solar cell.

1.10.3 Planar architecture:

1.10.3.1 Normal planar structure

The success of meso-superstructured architecture and bipolar nature of organic-inorganic lead halide perovskite stemmed the development of thin film configuration without using a porous scaffold, thus further simplifying the device processing route. Miyasaka et al. pioneered the planar architecture employing $CH_3NH_3PbI_{3-x}Cl_x$ based perovskites. However, the device merely showed relatively low conversion efficiency of 1.8%.[28] Depositing pinhole free perovskite layer and avoiding the shunting path is the most important criterion to develop the planar structured device and improve the efficiency.

Yang et al. demonstrated a surface modification of ITO surface along with appropriate doping of TiO_2 CL and perovskite growth in a compatible environment which leads to efficiency enhancement of planar structured cell to 19.3%.[70] Kelly et al. replaced TiO_2 CL with zinc oxide (ZnO) ETM and demonstrated that absence of mesoporous layer avoids the constrained perovskite crystal growth resulting in large crystal size corresponding to higher electron-hole diffusion length and high conversion efficiency of ~16%. Moreover,

device incorporating ZnO allows device fabrication at room temperature without any calcination or sintering step which further leads to the fabrication of flexible perovskite solar cell with efficiency reaching up to 10.2%.[65]

1.10.3.2Inverted planar architecture

Alternate device architecture which complete p-i-n junction thin film structure was widely employed among organic photovoltaic research community. Chen et al. pioneered inverted cell structure by sandwiching organic-inorganic lead halide perovskite in between poly(3,4-ethylenedioxythiophene):poly-(styrenesulfonic acid) (PEDOT:PSS) and (6,6)-phenyl C_{61}-butyric acidmethyl ester (PCBM) acting as p-type and n-type transporter respectively. However the initial efficiency was low (~4%) which was attributed to poor perovskite layer formation onto a PEDOT:PSS layer. Later on, by means of device optimization and perovskite deposition by solvent engineering process, a high efficiency of 18% was recorded in same configuration.[71]

In this structure, a consequent V_{oc} loss is inevitable due to slightly acidic nature of PEDOT:PSS and imperfect ohmic contact of perovskite/PEDOT:PSS interface. Hence further research direction towards replacing PEDOT:PSS with polymers such as poly(N-9′-heptadecanyl-2,7-carbazole-alt-5,5-(4′,7′ -di(thien-2-yl)-2′,1′,3′- benzothiadiazole)) (PCDTBT)[72] became more attractive, however, these polymers are usually hydrophobically leading to inefficient perovskite crystal growth which deteriorates long-term stability of the cell. To enhance the device stability, replacement of organic n- and p-type transporting layers with inorganic one was a welcome approach. In addition to charge transporting, incorporating metal oxide layers improved the stability against water which eventually leads to enhanced efficiency beyond 16% and long-term stability up to 1000 hours.[73] Fig. 1.13 depicts the schematic representation of normal and inverted structured planar device architecture.

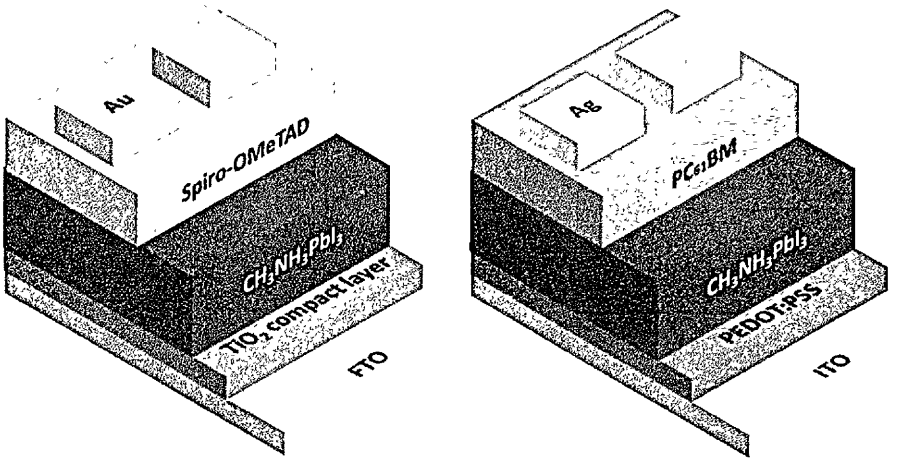

Figure 1.13: Schematic illustration of normal planar structure (left) and inverted planar structure (right)

1.10.4 HTL and ETL free architecture

In addition to above mentioned device architectures, hole- and electron transporting layer free devices have also been demonstrated (Fig. 1.14). Etgar et al. demonstrated HTM layer free perovskite device by using TiO_2 nanosheets as an electron transport material with efficiency reaching up to 5.5%.[74] It also unveiled p-type transporting characteristic of perovskite material. Further halide tuning by incorporating Br- boosted the device performance to 8.5% efficiency. Nevertheless, short-circuit current density (J_{sc}) and open-circuit voltage (V_{oc}) values were relatively lower in comparison to devices employing spiro-OMeTAD HTM layer, further revealing the importance of HTM layer in carrier collection and recombination.

On the other hand, after the success of planar architecture, an extensive device configuration of the incomplete p-i-n junction was concerned due to bipolar nature of organo-lead halide perovskite material. Fang et al. demonstrated ETL free device by depositing perovskite layer by one step deposition while Kelly et al. deposited by sequential deposition.[75] The higher electron mobility of neat $CH_3NH_3PbI_3$ in comparison to perovskite infiltrated in the TiO_2 mesoporous layer was said as the reason in former case while later one suggested due to the presence and blocking the effect of the remnant PbI_2 layer. In both the reports, uniform, large and pinhole-free perovskite layer were grown which demonstrated high V_{oc}. Surprisingly, devices incorporating TiO_2 as ETM didn't improve the

V_{oc} and slight enhancement in J_{sc} and fill factor (FF) was observed.[76] These results further suggested that TiO_2 may not be the ultimate ETM for efficient perovskite solar cells which further lead to the search for alternative new ETM layers.

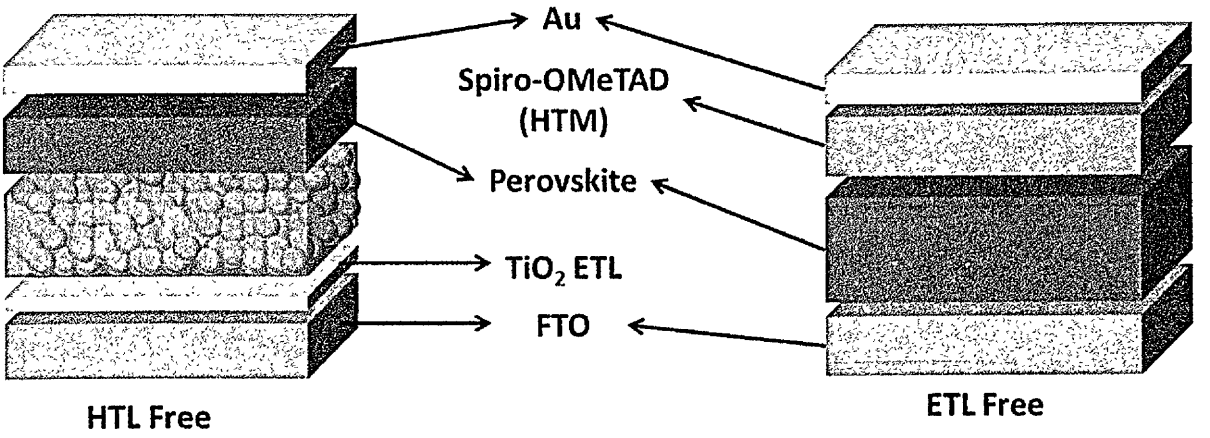

Figure 1.14: Schematic representation of (left) HTL- and (right) ETL-free perovskite solar cells.

1.11 Problems associated with lead perovskites and need for lead-free light absorbers: Motivation of thesis.

1.11.1 Lead-based perovskites

Organic-inorganic hybrid lead halide solar cells have attracted worldwide attention due to their exceptional light harvesting properties such as high optical absorption, bandgap tenability, high diffusion length and high carrier mobility. The power conversion efficiency (PCE) has no sooner scaled from 3.9% to 22.7% in a period of eight years.[26,27] Mesoporous and inverted planar architecture (as discussed earlier) mainly dominates high performing perovskite solar cells with efficiency reaching up to 22.7% certified PCE in mesostructured cell and uncertified efficiency up to 19.3% in the inverted planar structured cell. There is still a gap between presently recorded efficiency and theoretical limit predicted by Schottky-Queisser limit. Theoretical limits of short-circuit current density (J_{sc}) and fill factor (FF) has already been achieved (J_{sc} = 24 mA/cm^2 and FF = 85), however, improvement in open-circuit voltage offers room for efficiency enhancement to reach theoretical limit. To date,

maximum V_{oc} of ~1.2 V has been achieved which can be pushed up to 1.5 V. To date most of the high-efficiency work employed mesostructured architecture with TiO_2 mesoporous as under scaffold layer. Reports have suggested that TiO_2 blocking layer and the high surface of mesoporous metal oxide scaffold layer may benefit the recombination between perovskite and FTO and formation of uniform perovskite layer respectively offering a lower contact resistance for the forward electron transfer from the perovskite to the anode. In order to enhance the V_{oc} and to simplify the device fabrication process efforts have been made to replace commonly used TiO_2 with SnO_2, Al_2O_3 or ZrO_2. However, the V_{oc} of the device was not enhanced much.[64, 28, 27]

1.11.2 Lead-free perovskites:

Despite achieving PCE comparable to that of the conventional commercial silicon-based device and becoming "first high-quality halide semiconductors" – a promising candidate for next-generation photovoltaic technology, perovskite solar cell suffers from long-term stability when exposed to moisture, oxygen, continuous light illumination, and heat. Hygroscopic nature of organic cation reacts with water molecules and oxygen from the environment leading to degradation.[77] In addition to aforementioned reasons, intrinsic instable nature and low formation energy of perovskite material result in the formation of defect states within the perovskite material. These defect states or vacancies induce ion migration across the grain boundaries during device operating condition leading to degradation of the device under continuous light illumination. While exposing to high temperature causes lattice expansion of the perovskite material further accelerating the ion migration process and ultimately the cation escapes from the Pb-I framework. Lattice expansion during exposure to high temperature causes inter-diffusion of oxygen molecules further accelerating the degradation process.[78] Additionally, the chemical binding energies of atoms at the grain boundaries are almost half than those of the atoms within the crystals. The bonds, especially at the grain boundaries, having less binding energy is very sensitive to the external factors, as a result, the degradation initiates from the grain boundaries. As a result of the above-mentioned issues; photoactive perovskite material degrades into its non-photoactive components, that is, PbI_2, CH_3NH_2 and releases HI as a byproduct. The exposure of toxic degraded products, PbI_2 and HI, to the environment threatens human life.

A recent study demonstrates exposure of PbI_2 can cause a breakdown in the nervous and reproductive system and severely damages the brain.[44] Hence, it is indispensable to replace toxic lead (Pb) with non-toxic metals without compromising the photovoltaic properties and performance of the material.

Lately, Group 15 metals, bismuth (Bi) based perovskite have been theoretically and experimentally investigated. Sitting in the neighborhood of Pb, Bi possess similar electronic configuration and comparable ionic radii with that of Pb allowing them to incorporate effectively into the perovskite lattice.[46] Ternary non-toxic metal halides based perovskite materials ($A_3M_2X_9$; A = Cs^+, MA^+, Rb^+; M = Bi^{3+}, Sb^{3+}; X = I^-, Cl^-) have emerged recently as potential candidate due to its non-toxicity and high moisture stability. Optical properties, crystal structure, dielectric studies and quantum physical properties of various ternary bismuth halide perovskite materials have been formerly investigated but attempts to use it in photovoltaic devices was lately addressed. Firstly, Park et. al. integrated three different ternary bismuth halide absorbers; $Cs_3Bi_2I_9$, $(CH_3NH_3)_3Bi_2I_9$ and $(CH_3NH_3)_3Bi_2I_{9-x}Cl_x$ into the photovoltaic device and achieved 1%, 0.1%, and 0.01% respectively.[79] Low conversion efficiency was ascribed to poor dendrite-like morphology, a large number of defect states, and the relatively high bandgap of the material. Also, among the studied different materials $(CH_3NH_3)_3Bi_2I_9$ possess Wannier-Mott exciton binding energy of 70 meV which is slightly higher than lead halide perovskites (25-50 meV) and much less than $Cs_3Bi_2I_9$ and $(CH_3NH_3)_3Bi_2I_{9-x}Cl_x$.[81] Further Lyu et al. employed $(CH_3NH_3)_3Bi_2I_9$ perovskite material into TiO_2 mesostructured architecture and investigated its fundamental properties; however, high background carrier concentration, low carrier mobility, and wide bandgap resulted in low efficiency.[80] A perusal of various reported literature clearly corroborates that

1. $(CH_3NH_3)_3Bi_2I_9$ possess bandgap of ~2.1 eV which is almost same as lead bromide perovskite (~2.3 eV). The efficiency of lead bromide perovskite has been reported to be ~10% indicating a lot of room for performance enhancement of $(CH_3NH_3)_3Bi_2I_9$ based devices.
2. Due to high bandgap, $(CH_3NH_3)_3Bi_2I_9$ perovskite material has promising applications in tandem device architecture.

3. Studying and improving the morphology of $(CH_3NH_3)_3Bi_2I_9$ is highly desired to enhance the photophysical properties and performance of the device.
4. Developing low bandgap material is also highly desired for high efficient eco-friendly single junction solar cell.

1.12 Challenges and ideas to overcome – overview of subsequent thesis chapters.

Despite many efforts have been carried out to deposit suitable electron transporting layer and enhance the V_{oc}, few reports have demonstrated electron transporting layer (ETL) free perovskite solar cells, that is, perovskite layer was deposited directly on FTO substrates (without any electron transport layer). In addition to simple device fabrication process, devices without ETL demonstrated conversion efficiency more than 15%. Interestingly, as discussed in ETL free architecture section (1.10.4), devices showed high open-circuit voltage (V_{oc}) up to 1 V and devices didn't show any significant V_{oc} enhancement after incorporating TiO_2 CL. This evidently suggests that TiO_2 CL is not the appropriate material for enhancing the V_{oc} and studies on recombination pathways can provide further direction to enhance the V_{oc} and simultaneously the conversion efficiency of perovskite solar cells. Therefore, to overcome this challenge we fabricated perovskite solar cells by employing magnesium oxide (MgO) thin layer at various interfaces and based on the obtained results we proposed a mechanism for possible recombination channel in widely used TiO_2 ETL based perovskite solar cells. The details of these results will be discussed in **chapter 2.**

In case of bismuth-based lead-free perovskite solar cells, efforts have been made to enhance the efficiency by replacing $CH_3NH_3^+$ with NH_4^+, [py][BiI_4], [mepy][BiI_4]. Even attempts were made to develop double perovskite material by combining monovalent metals such as silver and copper with trivalent bismuth metal to form $Cs_2AgBiBr_6$. However, due to the high bandgap of these materials, and large carrier effective masses theoretical studies have reported its limitations. Herein, studies on the morphological evolution of $(CH_3NH_3)_3Bi_2I_9$ – a bismuth-based lead-free perovskite material is performed. The obtained results will be covered in **chapter 3 and 4.**

The high bandgap of $(CH_3NH_3)_3Bi_2I_9$ – a zero-dimensional material limit its application to tandem device architecture and in order to enhance the efficiency of single

junction device eco-friendly materials with desirable photovoltaic properties are highly desired. Towards this path, studies have also been carried out to explore bismuth-based low band gap material including bismuth iodide (BiI_3) and series of Ag-Bi-I compounds. BiI_3 is a two-dimensional material having a bandgap of ~1.8 eV and possess interesting optoelectronic properties. We incorporated BiI_3 in mesostructured architecture and studied its temperature dependent morphological evolution. The results will be discussed in **chapter 5**. Because of low bandgap and lower exciton binding energy, three dimensional (3D) materials demonstrates better optical properties for light harvesting than 2D one. Hence, efforts were made to combine monovalent silver and trivalent bismuth in different stoichiometric ratios to form a series of Ag-Bi-I materials. Studies on various Ag-Bi-I materials will be discussed in **chapter 6**. Lastly, thesis summary and future scope conclude **chapter 7**.

1.13 References

1 World Population Policies 2013, *United Nations Publication,* **2013**

2 International Energy Outlook 2013, *U.S. Energy Information Administration,* **2013.**

3 Evans, A.; Strezov, V.; Evans, T., J., *Renewable and Sustainable Energy Reviews*, **2009**, *13*, 1082.

4 Wuerfel, P., *Physics of solar cells: from principles to new concepts* (Wiley-VCH, 2005).

5 U.S. Energy Information Administration

6 http://www.ucsusa.org/clean_energy/our-energy-choices/coal-and-other-fossil-fuels/thehidden-cost-of-fossil.html

7 Harvard School of public health http://chge.med.harvard.edu/category/nature-healthbuilt-environment

8 Armaroli, N.; Balzani, V., *Angew. Chem., Int. Ed.,* **2007**, *46,* 52-60.

9 Balzani, V.; Credi, A.; Venturi, M., *ChemSusChem,* **2008**, *1,* 26-58.

10 Chen, Z.; Blaabjerg, F., *Renewable and Sustainable Energy* Reviews, **2009**, *13,* 1288.

11 Solangi, K., H.; Islam, M., R.; Saidur, R.; Rahim, N., A.; Fayaz, H., *Renewable and Sustainable Energy Reviews*, **2011**, *15*, 2149.

12 Etgar, L., *Materials*, **2013**, *6*, 445-459.

13 Green, M. A.; Emery, K.; Hishikawa, Y.; Warta, W.; Dunlop, E. D., *Prog. Photovoltaics*, **2012**, *20*, 606-612.

14 Xiang, H. J.; Huang, B.; Kan, E. J.; Wei, S. H.; Gong, X. G., *Phys. Rev. Lett.*, **2013**, *110*, 118702-118710.

15 Surek, T., *J. Cryst. Growth*, **2005**, *275*, 292.

16 Aberle, A., G., *Thin Solid Films.*, **2009**, *517*, 4706–4710

17 Chopra, K., L.; Paulson, P., D.; Dutta, V., *Prog. Photovolt: Res. Appl.*, **2004**,*12*,69–92

18 Wronski, C., R.; Pearce, J., M.; Deng, J.; Vlahos, V.; Collins, R., W., *Thin Solid Films*, **2004**,*451*, 470-475.

19 Lewis, N. S., *Science*, **2007**, *315*, 798-801.

20 Poa, R.; Carboneraa, C.; Bernardia, A.; Tintib, F.; Camaioni, N., *Solar Energy Materials and*

Solar Cells, **2012**, *100*, 97-114.

21 Scharber, M., C.; Mühlbacher, D.; Koppe, M.; Denk, P.; Waldauf, C.; Heeger, A., J.; Brabec, C., J., *Adv. Mater.*, **2006**, 18, 789–794.

22 Yella, A.; Lee, H., W.; Tsao, H., N.; Yi, C.; Chandiran, A., K.; Nazeeruddin, M., K.; Wei-

Guang,E., D.; Yeh, C.-Y.; Zakeeruddin, S., M.; Grätzel, M., *Science* , **2011**, *3344.*

23 Cava, R. J.; Batlogg, B.; Espinosa, G. P.; Ramirez, A. P.; Krajewski, J. J.; Peck, W. F., Jr; Rupp, L. W., Jr., *Nature,* **1989**, *339*, 291–293.

24 Schilling, A.; Cantoni, M.; Guo, J. D.; Ott, H. R., *Nature,* **1993**, *363*, 56–58.

25 Weber, D., *Z. Naturforsch*, **1978,** *33 b*, 1443-1445.

26 Kojima, A.; Teshima, K.; Shirai, Y; Miyasaka, T., *JACS,***131**, 6050-6051 (2009).

27 Yang, W. S.; Park, W. B.; Jung, E. H.; Jeon, N. J.; Kim, Y. C.; Lee, D. U.; Shin, S. S.; Seo, J.; Kim, E. K.; Noh, J. H.; Seok, S. I., *Science*, **2017**, *356*, 1376-1379

28 Lee, M. M.; Teuscher, J.; Miyasaka, T.; Murakami, T. N.; Snaith, H. J., *Science*, **2012**, *338 (6107)*, 643-647

29 Stranks, S. D.; Eperon, G. E.; Grancini, G.; Menelaou, C.; Alcocer, M. J. P.; Leijtens, T.; Herz, L. M.; Petrozza, A.; Snaith, H. J., *Science*, **2013**, *342*, 341-344.

30 Pazos-Outon, A. M.; Szumilo, M.; Lamboll, R.; Richter, J. M.; Crespo-Quesada, M.; Abdi-Jalebi, M.; Beeson, H. J.; Vrucinic, M.; Alsari, M.; Snaith, H. J.; Ehrler, B.; Friend, R. H.; Deschler, F., *Science*, **2016**, *351 (6280)*, 1430-1433.

31 G. C. Xing, N. Mathews, S. Y. Sun, S.S. Lim, Y. M. Lam, M. Grätzel, S. Mhaisalkar and T.C. Sum, *Science*, **2013**, *342*, 344.

32 Kagan, C.; Mitzi, D.; Dimitrakopoulos, C., *Science*, **1999**, *286*, 945-947.

33 Chondroudis, K.; Mitzi, D. B., *Chemistry of materials*, **1999**, *11*, 3028-3030.

34 Im, J.-H.; Lee, C.-R.; Lee, J.-W.; Park, S.-W.; Park, N.-G., *Nanoscale*, **2011**, *3*, 4088-4093.

35 Li, W. *et al. Journal of Materials Chemistry A*, **2013**, *1*, 11735-11740.

36 Lee, M. M.; Teuscher, J.; Miyasaka, T.; Murakami, T. N.; Snaith, H. J., *Science*, **2012**, *338*, 643-647.

37 Kim, H.-S.; Lee, C.-R.; Im, J., H.; Lee, K.-B.; Moehl, T.; Marchioro, A.; Moon, S.-J.; Baker, R., H.; Yum, J.-H.; Moser, J., E.; Graetzel, M.; Park, N.,G., *Scientific reports*, **2012**, *2*, 591.

38 Boix, Pablo P.; Agarwala, S.; Koh, T., M.; Mathews, N.; Mhaisalkar, S., G., *J. Phys. Chem. Lett.*, **2015**, *6 (5)*, 898–907.

39 Gao, Peng, Michael Grätzel, and Mohammad K. Nazeeruddin, *Energy & Environmental Science*, **2014**, *7*, 2448-2463.

40 Kazim, Samrana, Nazeeruddin, M., K.; Graetzel, M.; Ahmad, S., *Angewandte Chemie International Edition*, **2014**, *53*, 2812-2824.

41 Song, T.-B.; Yokoyama, T.; Aramaki, S.; Kanatzidis, M., G., *ACS Energy Lett.*, **2017**, *2 (4)*, 897–903.

42 Zhao, D.; Yu, Y.; Wang, C.; Liao, W.; Shreshtha, N.; Grice, C., R.; Cimaroli, A., J.; Guan, L.; Ellingson, R., J.; Zhu, K.; Zhao, X.; Xiong, R.-G.; Yan, Y., *Nature Energy*, **2017**, *2*, 17018.

43 Konstantakou, M.; Stergiopolous, T., *J. Mater. Chem. A*, **2017**, *5*, 11518-11549

44 Babayigit, A.; Ethirajan, A.; Muller, M.; Conings, B., *Nature Materials;* **2016**, *15*, 247-251.

45 Krishnamoorthy, T.; Ding, H.; Yan, C.; Leong, W. L.; Baikie, T.; Zhang, Z.; Sherburne, M.; Li, S.; Asta, M.; Mathews, N.; Mhaisalkar, S. G., *J. Mater. Chem. A*, **2015**, *3*, 23839-23832.

46 M. Lyu, J-H. Yun, M. Cai, Y. Jiao, P. V. Bernhardt, M. Zhang, Q. Wang, A. Du, H. Wang, G. Liu and L. Wang, *Nano Res.*, DOI: 10.1007/s12274-015-0948-y.

47 Choi, T.; Lee, S.; Choi, Y., J.; Kiryukhin, V.; Cheong, S.-W, *Science,* **2009**, 324, 63-66

48 Hamdeh, U. M.; Nelson, R. D.; Ryan, B. J.; Bhattacharjee, U.; Petrich, J. W.; Panthani, M. G., *Chem. Mater.*, **2016**, *28 (18)*, 6567-6574.

49 Turkevych, I.; Kazaoui, S.; Ito, E.; Urano, T.; Yamada, K.; Tomiyasu, H.; Yamagishi, H.; Kondo, M.; Aramaki, S., *ChemSusChem,* **2017**, DOI: 10.1002/cssc.201700980.

50 Eperon, G. E.; Burlakov, V. M.; Docampo, P.; Goriely, A.; Snaith, H. J., *Advanced Functional Materials*, **2014**, *24*, 151-157.

51 Liu, M.; Johnston, M. B.; Snaith, H. J., *Nature*, **2013**, *501*, 395-398.

52 Kulkarni, A.; Singh, T.; Ikegami, M.; Miyasaka, T., *RSC Adv.*, **2017**, *7*, 9456-9460.

53 Jeon, N. J.; Noh, J. H.; Kim, Y., C.; Yang, W., S.; Ryu, S.; Seok, S., I., *Nat Mater*, **2014**, *13*, 897-903.

54 Xiao, M.; Huang, F.; Huang, W.; Dkhissi, Y.; Zhu, Y.; Etheridge, J.; Gray-Weale, A.; Bach, U.; Cheng, Y.-B.; Spiccia, L., *Angewandte Chemie*, **2014**, *126*, 10056-10061.

55 Zhou, Y.; Yang, M.; Wu, W.; Vasiliev, A., L.; Zhu, K.; Padture, N., P., *Journal of Materials Chemistry A,* **2015**, *3*, 8178-8184.

56 Liang, K.; Mitzi, D., B.; Prikas, M., T., *Chemistry of materials*, **1998**, *10*, 403-411.

57 Burschka, J.; Pellet, N.; Moon, S.-J.; Baker, R., H.; Gao, P.; Nazeeruddin, M., K.; Graetzel, M., **2013**, *499*, 316-319.

58 Wu, Y.; Islam, A.; Yang, X.; Qin, C.; Liu, J.; Zhang, K.; Peng, W.; Han, L., *Energy & Environmental Science*, **2014**, *7*, 2934-2938.

59 Im, J.-H.; Jang, I.-H.; Pellet, N.; Grätzel, M.; Park, N.-G., *Nature nanotechnology*, **2014**, *9*, 927-932.

60 Kavan, L.; Grätzel, M., *Electrochimica Acta*, **1995**, *40*, 643-652.

61 Chandiran, A. K.; Yella, A.; Mayer, M., T.; Gao, P.; Nazeeruddin, M., K.; Graetzel, M., *Advanced Materials,* **2014**, *26*, 4309-4312.

62 Kavan, L.; Tétreault, N.; Moehl, T.; Grätzel, M., *The Journal of Physical Chemistry C*, **2014**, *118*, 16408-16418.

63 Pinpithak, P.; Chen, H.-W.; Kulkarni, A.; Sanehira, Y.; Ikegami, M.; Miyasaka, T., *Chem. Lett.*, **2017**, *46(3)*, 382-384.

64 Zhang, Y.; Elawas, M.; Yu, Z.; Jiang, X.; Lai, J.; Sun, L., *RSC Adv.*, **2016**, *6*, 108888-108895

65 Yang, W. S.; Park, W. B.; Jung, E. H.; Jeon, N. J.; Kim, Y. C.; Lee, D. U.; Shin, S. S.; Seo, J.; Kim, E. K.; Noh, J. H.; Seok, S. I., *Science*, **2017**, *356*, 1376-1379.

66 Ball, J. M.; Lee, M. M.; Hey, A.; Snaith, H. J., *Energy & Environmental Science,* **2013**, *6*, 1739-1743.

67 Bi, D.; Moon, S.-J.; Haeggman, L.; Boschloo, G.; Yang, L.; Johansson, E., M., J.; nazeeruddin, M., K.; Graetzel, M.; Hagfeldt, A., *RSC Advances,* **2013**, *3*, 18762-18766.

68 Wojciechowski, K.; Saliba, M.; Leijtens, T.; Abate, A.; Snaith, H. J., *Energy & Environmental Science*, **2014**, *7*, 1142-1147.

69 Kim, H.-S.; Mora-Sero, I.; Gonzalez-Pedro, V.; Fabregat-Santiago, F.; Juarez-Perez, E., J.; Park, N.-G.; Bisquert, J., *Nature communications*, **2013**, *4,* doi:10.1038/ncomms3242.

70 Zhou, H.; Chen, Q.; Li, G.; Luo, S.; Song, T.-B.; Duan, H.-S.; Hong, Z.; You, J.; Liu, Y.; Yang, Y., *Science*, **2014**, *345*, 542-546.

71 Heo, J. H.; Han, H. J.; Kim, D.; Ahn, T. K.; Im, S. H., *Energy & Environmental Science*, **2015**, *8*, 1602-1608.

72 Malinkiewicz, O.; Yella, A.; Lee, Y., H.; Espallargas, G., M.; Graetzel, M.; Nazeeruddin, M., K.; Bolink, H., J., *Nature Photonics*, **2014**, *8*, 128-132.

73 You, J.; Meng, L.; Song, T.-B.; Huo, T.-F.; Yang, Y.; Chang, W.-H.; Hong, Z.; Chen, H.; Zhou, H.; Chen, Q.; Liu, Y.; Marco, N., D.; Yang, Y., *Nature nanotechnology*, **2016**, *11*, 75-81.

74 Etgar, L.; Gao, P.; Xue, Z.; Peng, Q.; Chandiran, A., K.; Liu, B.; Nazeeruddin, M., K.; Graetzel, M., *J. Am. Chem. Soc.,* **2012**, *134 (42),* 17396–17399.

75 Liu, D.; Yang, J.; Kelly, T. L., *Journal of the American Chemical Society*, **2014**, *136*,

17116-17122.

76 Ponseca Jr, C. S.; Savenije, T., J.; Abdellah, M.; Zheng, K.; Yartsev, A.; Pascher, T.; Harlang, T.; Chabera, P.; Pullerits, T.; Stepanov, A.; Wolf, J.-P.; Sundstrom, V., *J. Am. Chem. Soc.*, **2014**, *136 (14)*, 5189–5192.

77 Chaudhary, B.; Kulkarni, A.; Jena, A. J.; Ikegami, M.; Udagawa, Y.; Kunugita, H.; Ema, K.; Miyasaka, T., *ChemSusChem*, **2017**, DOI: 10.1002/cssc.201700271.

78 Niu, G.; Li, W.; Li, J.; Liang, X.; Wang, L., *RSC Adv.*, **2017**, *7*, 17473-17479.

79 B.-W. Park, B. Philippe, X. Zhang, H. Ransmo, G. Boschloo and E. M. J. Johansson, *Adv. Mater.*, **2015**, *27*, 6806.

Chapter 2

Revealing the Possible Recombination Loss at FTO/TiO_2 by Incorporating Thin Layer of MgO in Lead Halide Perovskite Solar Cells.

Abstract

In this work, studies have been carried out on origin of loss in open-circuit voltage (V_{oc}) in perovskite solar cells due to possible trap-assisted recombination within the widely used TiO_2 compact layer (CL) and at its interface with FTO substrates. A thin layer (TL) of MgO was employed to investigate the recombination mechanism. A TL of MgO in place of TiO_2 CL (~50-60 nm) enhances V_{oc} of the cell significantly while the MgO layer on TiO_2 CL (TiO_2-MgO bilayer) does not change the V_{oc} much in comparison to only TiO_2 CL based device. In combination with open-circuit voltage decay (OCVD) measurements, we reveal that recombination at FTO/TiO_2 interface is a major factor regulating the voltage and efficiency in commonly used TiO_2 mesostructured perovskite solar cells.

2.1 Introduction

After the pioneering report on perovskite (CH3NH3PbX3, X = I^-, Br^-) as visible light absorber in liquid junction solar cells with 3.8% efficiency,[1,2] the drive for research on this material became tremendously fast with the use of this material in solid junction devices and a certified power conversion efficiency (PCE) of 22.1% was achieved.[3] Moreover, the fabrication of such high efficiency perovskite solar cells involves simple and inexpensive solution methods. Therefore, this new photovoltaic technology shows enormous potential as a cheaper alternative to existing conventional photovoltaic technologies. The intrinsic electronic properties, such as ambipolar charge mobility and long carrier diffusion length of the perovskite semiconductor are two major attributes to high PCE of the devices.[4,5,6] In addition, well-suppressed recombination of photoexcited charge carriers, which is strongly affected by the surrounding carrier collecting materials, leads to generation of large photocurrent as well as high voltage. In other words, surrounding carrier collecting materials play equally an important role in maximizing the current and voltage by minimizing the recombination loss.

Generally, a thin compact layer (CL) or a hole blocking layer (BL) ((~50-60 nm) is required to be deposited on fluorine doped tin oxide (FTO) conductive substrate in order to avoid direct contact between FTO and perovskite and/or hole transporting material (HTM). Moreover, such dense CLs made on FTO are also believed to prevent recombination caused by back transfer of electron from FTO to either perovskite or HTM. To avoid such recombination, even modification of TiO_2 CL,[7] ZnO layer with self-assembled monolayers[8] have been found to enhance the overall PCE. MgO is an insulating material and has been employed in perovskite solar cells to reduce recombination.[9,10] It has been reported that CL made of Mg-doped TiO_2 which improves open-circuit voltage (V_{oc}) by up-shift of the conduction band edge of TiO_2 and thereby reducing recombination.[9] A recent study employing MgO in mesoscopic perovskite solar cell has shown enhancement in V_{oc} by avoiding direct contact between FTO and perovskite.[11] However, there are several reports that contradict the presumption of recombination at conductive substrates and perovskite interface. For instance, planar architecture cells made with perovskite directly grown on FTO[12] and indium doped tin oxide (ITO)[13] have been found to generate V_{oc} as high as 1 V,

suggesting that the recombination at this interface is improbable. Further, SnO_2 having lower conduction band edge than TiO_2 has been found to generate V_{oc} of above 1 V in perovskite solar cells[14] indicating that the recombination between CL and perovskite or HTM interface is also small. Therefore, the mechanisms of recombination in perovskite solar cells are still unclear and need to be investigated with various CL and device configuration for better understanding. Studies have focused on the relevance of TiO_2 CL to electron transfer rectification by inserting a thin non-conductive layer of MgO at the interface of FTO-TiO_2 mesoporous layer and TiO_2 CL-mesoporous TiO_2 layer. Although the role of MgO in carrier transport regulation has not been clear, the present study reveals that TiO_2 CL itself is responsible for reasonable voltage loss in TiO_2 based perovskite solar cells, which is a major finding here in addition to the passivation effect of MgO.

2.2 Experimental Methods

Unless otherwise stated, all the required materials were purchased from Sigma-Aldrich or Wako and were used as received. Spiro-OMeTAD was purchased from Merck and used as received.

2.2.1 Methylammonium iodide synthesis

24 mL of methylamine solution (33% in ethanol) was diluted with 100 mL of ethanol (anhydrous). Under constant stirring, 10 mL of hydroiodic acid (57 wt. %) was added drop by drop to the prepared solution. After the reaction time of 1 hour at room temperature, the methylammonium iodide (MAI) was obtained by evaporating ethanol by using a rotor evaporator. The obtained white solid was washed twice with dry diethyl ether and finally re-crystallized from ethanol.

2.2.2 Device fabrication

FTO-coated transparent glass sheets (8 Ω sq^{-1}, Nippon Sheet Glass, 1.1 mm in thickness) were patterned by etching off FTO with Zn powder and 3 M HCl. Then, the substrates were cleaned with ultrasonication in 2% hellmax soap solution, deionised water and ethanol for 15 min each. After oxygen plasma treatment done to remove the traces of organic residues for 10 min, ~50-60 nm TiO_2 CL was deposited by spin coating 0.15 M and

0.3 M titanium diisopropoxide bis(acetylacetonate) (75 wt% in isopropanol, Aldrich) in isopropanol (Wako). First, 0.15 M solution was spin coated at 2000 rpm for 30 sec followed by annealing at 125 ^{O}C for 5 min. The same procedure was followed twice to deposit 0.3 M and finally the substrates were annealed at 550 ^{O}C for 30 minutes. 80 mM $TiCl_4$ treatment was given at 70 ^{O}C for 30 minutes and again the cells were annealed at 550 ^{O}C for 30 minutes. In case of MgO thin layer, on FTO, 25 mM solution of magnesium acetate tetrahydrate was dissolved in ethanol and was stirred at 100^{O}C for 1 min prior to deposition at 3000 rpm for 30 sec followed by annealing at 100^{O}C for 5 min. In case of bilayer, after deposition of TiO_2 CL, 25 mM magnesium acetate solution in ethanol was deposited by spin coating at 3000 rpm for 30 sec followed by annealing at 100 ^{O}C for 5 min.

For all the devices, mesoporous layer was obtained by spin-coating a commercially available TiO_2 paste (Dyesol, 18NR-T) in ethanol (1:3) at 4000 rpm for 30 sec and annealing at 550 ^{O}C for 30 min. Perovskite was deposited by sequential deposition method (Bruschka et. al., 2013; Yantara et. al., 2015). First, 1M PbI_2 solution in DMF was deposited on mesoporous coated substrate at 6500 rpm for 30 sec followed by drying at 70 ^{O}C for 30 min. After cooling down, the substrates were dipped in methylammonium iodide solution in 2-propanol (10 mg/ml) for 50 sec. Then, the perovskite coated substrates were rinsed in 2-propanol and were dried using spin coater at 4500 rpm for 10 sec. The substrates were then heated at 70^{O}C for 30 min. The HTM solution was prepared by dissolving 84 mg of spiro-OMeTAD, 14.053 µl of 4-*tert*-butylpyridine (TBP, Aldrich), 27.013 µl of a stock solution of 520 mg/ml of lithium bis(trifluoromethylsulfonyl)imide in acetonitrile in 1 ml of chlorobenzene. The prepared spiro-OMeTAD solution was deposited on perovskite by spin-coating at 3000 rpm for 30 seconds. After spiro-OMeTAD coating, the substrates were stored in dark and ambient atmosphere overnight before the deposition of 80 nm Au as back contact electrode by thermal evaporation. All the perovskite deposition preparative work was carried out under ambient atmosphere with uncontrolled humidity.

2.3 Device Characterization

Photovoltaic characterization of the devices was done by measuring current on voltage scan in forward (-0.1 V to 1.1 V) and backward (1.1 V to 0 V) directions both under light (100 mW/cm^2 AM1.5, 1 sun intensity) provided by a solar simulator (Peccell

Technologies PEC-L01) and dark. A Keithley source meter (Model 2400) was used for all electrical measurements. The voltage scan speed used to obtain photocurrent density-voltage (J-V) curves was kept at 200 mV/s. The active area of the device was 0.09 cm^2. The cross-sectional scanning electron microscopy images and Energy dispersive X-ray spectroscopy (EDX) of all the devices were taken with a HITACHI SEM instrument (SU8000).

2.3 Results and discussion

2.3.1 Thin film characterization

To investigate the back transfer and loss in V_{oc} at FTO/TiO_2 CL interface thin layer (TL) of MgO was deposited, both as an independent layer directly on FTO and as a bilayer with TiO_2 CL as bottom layer by spin coating 25 mM solution of $Mg(CH_3COO)_2$ in ethanol. The device structures are depicted in Fig. 2.1. From the cross sectional scanning electron micrograph (SEM) (Fig. 2.2), it is evident that a thick (~50-60 nm) TiO_2 CL (Fig. 2.2a) was formed while MgO layer was too thin to be visible (Fig. 2.2b). However, small MgO particles are seen in the valleys between large FTO grains as shown in Fig. 2.3a and SEM energy dispersive X-ray (EDX) (Fig. 2.2 d) mapping of the surface confirms coverage of the FTO substrates with Mg as MgO. In case of bilayer, MgO layer coated on TiO_2 CL (TiO_2-MgO) bilayer) also showed MgO particles that were spread over the TiO_2 under layer (Fig. 2.3 c).[15] In spin coating TiO_2 CL many pores were seen (Fig. 2.3 a), which were partially covered by MgO particles and some MgO aggregates of rod shape were also seen scattered over the substrates (Fig. 2.3 c). Bilayer morphology also shows that TiO_2-MgO bilayer has some places where TiO_2 can have electrical contact with perovskite layer.

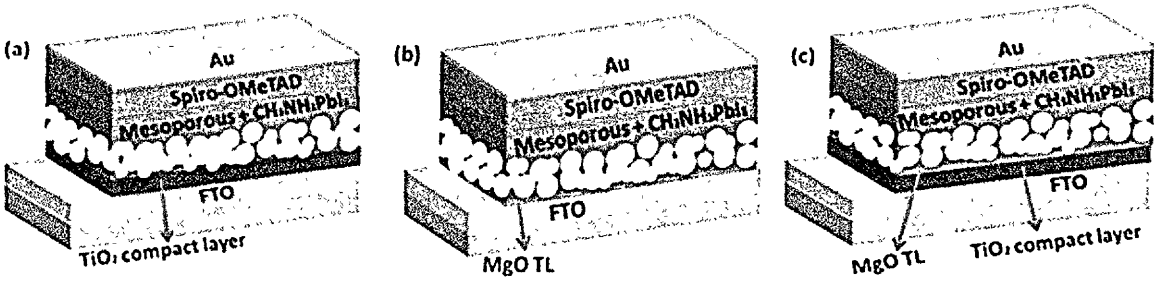

Fig. 2.1: Schematics of device architecture of (a) TiO_2 CL, (b) MgO TL, and (c) TiO_2-MgO bilayer incorporated perovskite devices.

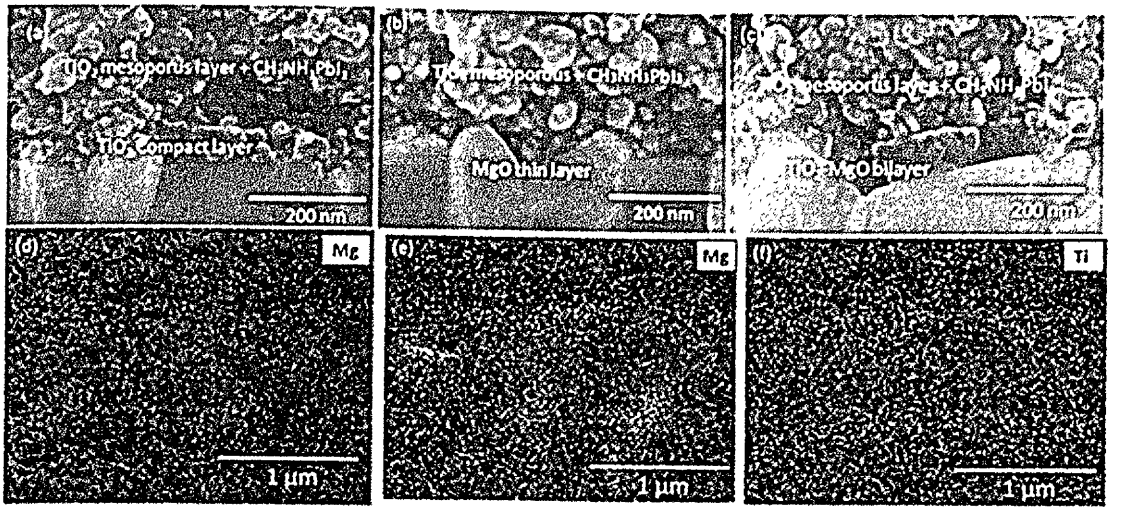

Figure 2.2: Cross sectional SEM images of TiO_2 mesoscopic $CH_3NH_3PbI_3$ perovskite solar cells with (a) TiO_2 CL, (b) MgO TL, (c) TiO_2-MgO bilayer as interlayers between FTO and TiO_2 mesoporous layer. Top surface SEM-Energy Dispersive X-ray (EDX) spectroscopic images of (d) MgO TL and TiO_2-MgO bilayer showing mapping of (e) Mg and (f) Ti.

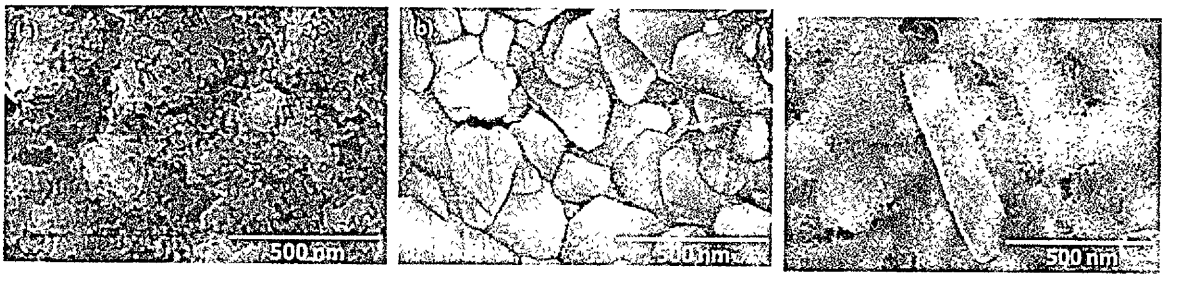

Figure 2.3: Top surface SEM images of TiO_2 mesoscopic $CH_3NH_3PbI_3$ solar cells with (a) TiO_2 CL, (b) MgO TL and (c) TiO_2-MgO bilayer interlayer's between FTO and TiO_2 mesoporous.

2.3.2 Photovoltaic performance analysis

The MgO TL on the FTO substrate as a substitute to ~50-60 nm thick TiO_2 CL enhanced V_{oc} of the device significantly (~16%) despite of not covering completely, that is, having many pinholes where perovskite can directly touch FTO. On the contrary, a dense ~50-60 nm thick layer of TiO_2 exhibited lower V_{oc}. As shown in the histogram plot (Fig. 2.4a) for the cells with TiO_2 CL, V_{oc} varied from 0.8 V to 0.9 V with majority of the samples showing the V_{oc} of 0.86 V while the values for the cells with MgO TL varied from

0.9 V to 1.02 V and majority of samples showed a V_{oc} of 0.98 V. Moreover, increase in V_{oc} in case of MgO TL was accompanied with slight reduction in short-circuit current density (J_{sc}) (from ~18.5 mA/cm^2, in TiO_2 CL devices, to ~17.5 mA/cm^2) (Fig. 2.4 b). Slight increase in resistance to electron transfer through MgO to FTO, which happens via tunneling, can be the reason for decrease in J_{sc} as well as concomitant decrease in fill factor (FF).[16] As a result the overall PCE of these cells were found to be same in both the cases; MgO TL and TiO_2 CL. It was believed that MgO blocked the back transfer of electron from FTO to perovskite and thereby improved V_{oc}. This result was then compared with the TiO_2-MgO bilayer structure in which FTO surface was coated TiO_2 CL followed by TL of MgO on top of it. Although with the use of double blocking structure (TiO_2 and MgO) against recombination we expected further improvement in V_{oc}, we found decrease in V_{oc} with this structure. The majority of the TiO_2-MgO bilayer samples showed a V_{oc} of 0.9 V (Fig. 2.4a), which is slightly higher than 0.86 V for cells with TiO_2 CL but lower than V_{oc} (0.98 V) of the cell wih MgO TL. This evidently indicated that MgO on FTO and TiO_2 CL worked differently and there is a reasonable loss in V_{oc} due to the presence of TiO_2 CL itself. The main difference between TiO_2-MgO bilayer and MgO TL is that the electron is finally collected, after passing the blocking layer, by TiO_2 in case of TiO_2-MgO bilayer and by FTO in case of MgO TL, respectively.

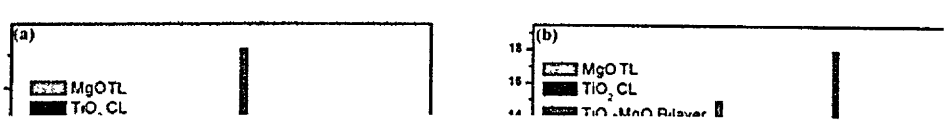

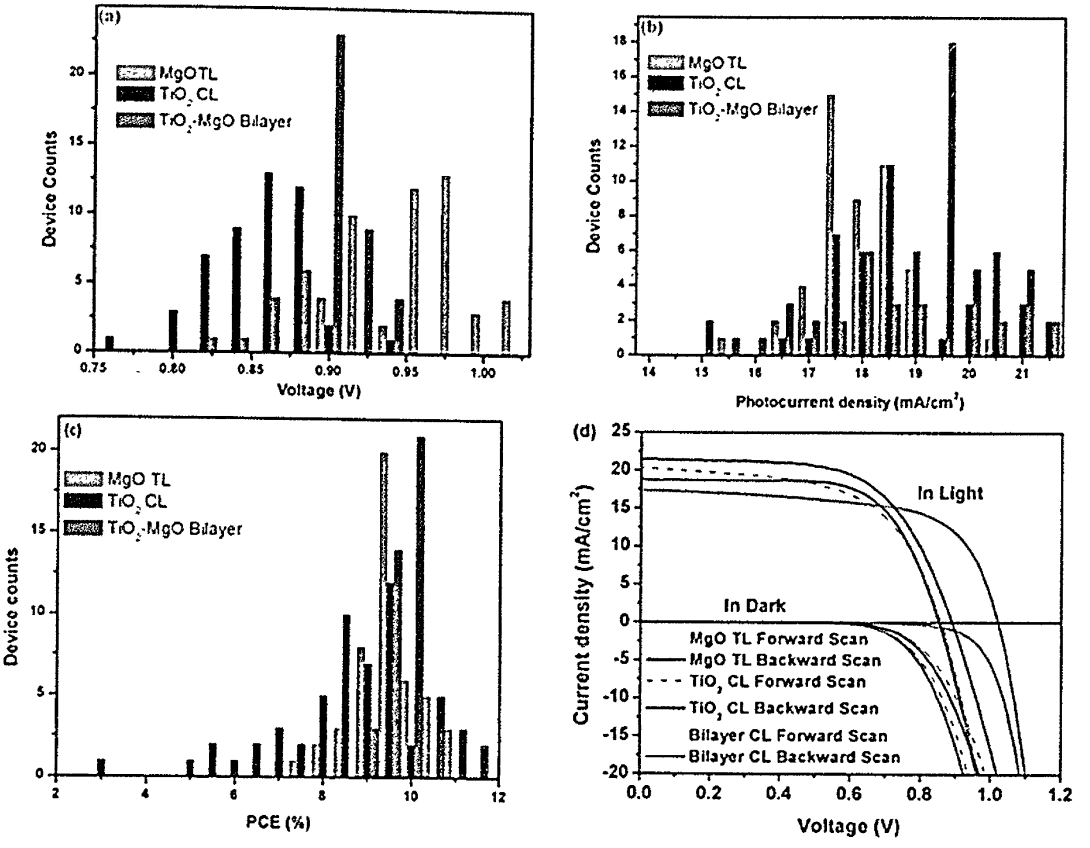

Figure 2.4: Histogram plot of (a) V_{oc}, (b) J_{sc}, and (c) PCE of 48 devices of each kind of TiO_2 mesoporous perovskite solar cells; with TiO_2 CL (black), MgO TL (red) and TiO_2-MgO bilayer (green). (d) J-V curves of best performing devices with TiO_2 CL, MgO TL and TiO_2-MgO bilayer.

Table 1 Photovoltaic characteristic (J_{sc}, V_{oc}, FF, PCE) of champion devices of each kind of TiO_2 mesoscopic perovskite solar cells; with TiO_2 CL, MgO TL and TiO_2-MgO bilayer. FS and BS stands for forward scan (i.e. from short circuit to open circuit) and backward scan (i.e. from open circuit to short circuit) respectively.

Cases Studied	Scan Direction	J_{sc} (mA/cm^2)	V_{oc} (V)	FF	PCE (%)
TiO_2 CL	FS	20.3	0.85	0.58	10.1
	BS	18.8	0.85	0.67	10.8
MgO TL	FS	16.65	0.99	0.53	8.89
	BS	17.3	1.02	0.65	11.53
TiO_2-MgO Bilayer	FS	21.6	0.9	0.58	11.3
	BS	21.4	0.89	0.62	11.8

To study the active role of TiO_2 CL, devices with thinner TiO_2 CL (not visible in SEM) (Fig. 2.5 a) and without CL (CL-free) (i.e. mesoporous layer directly deposited on FTO) (Fig. 2.5 b), were fabricated. J-V curves (under light and dark) of the best devices with TiO_2 Cl (~50-60 nm), thin TiO_2 CL (not visible in SEM) and without TiO_2 CL are depicted in Fig. 2.6 a. The histogram plot of V_{oc}, J_{sc} and PCE for 48 devices of each of the above three structures (CL free, thin and thick TiO2 CL) are shown in Fig. 2.6 b, c, d. Surprisingly, presence of TiO_2 CL (thick or thin) did not essentially improve any of the photovoltaic parameters in the cell and showed same V_{oc} of 0.85 V, as for the cells without CL. This implied that either the recombination between FTO and perovskite is improbable or the bottom of the TiO_2 porous layer is sufficiently dense to act like CL to prevent perovskite from touching FTO directly.[12, 13] Additionally, in all the three cases, possible role of remnant PbI_2 layer, which is generally formed on FTO and TiO_2 in two-step deposition process, is also considered in preventing recombination by blocking back transfer of electron.[17] All the above results suggests that back transfer of electron from FTO or TiO_2 to perovskite is not

significant and the lower V_{oc} of the cells with TiO_2 CL compared to that with MgO TL is due to loss by TiO_2 CL itself.

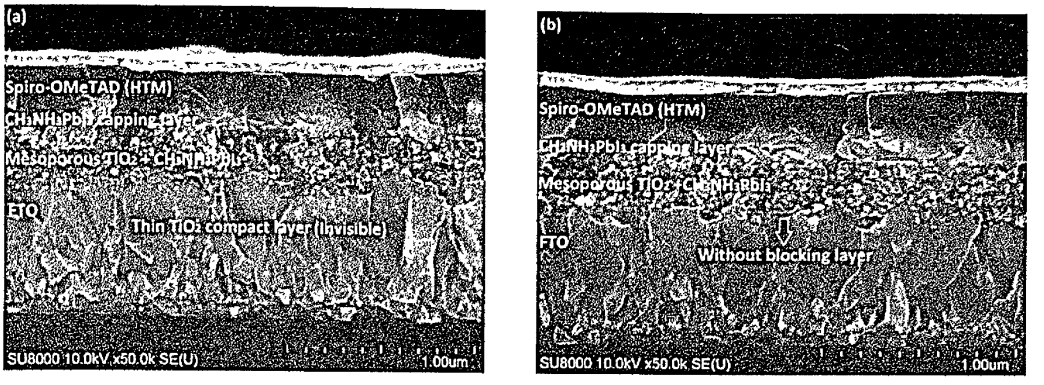

Figure 2.5: Cross-sectional SEM images with (a) thin TiO_2 CL and (b) without CL in TiO_2 mesoscopic $CH_3NH_3PbI_3$ solar cells.

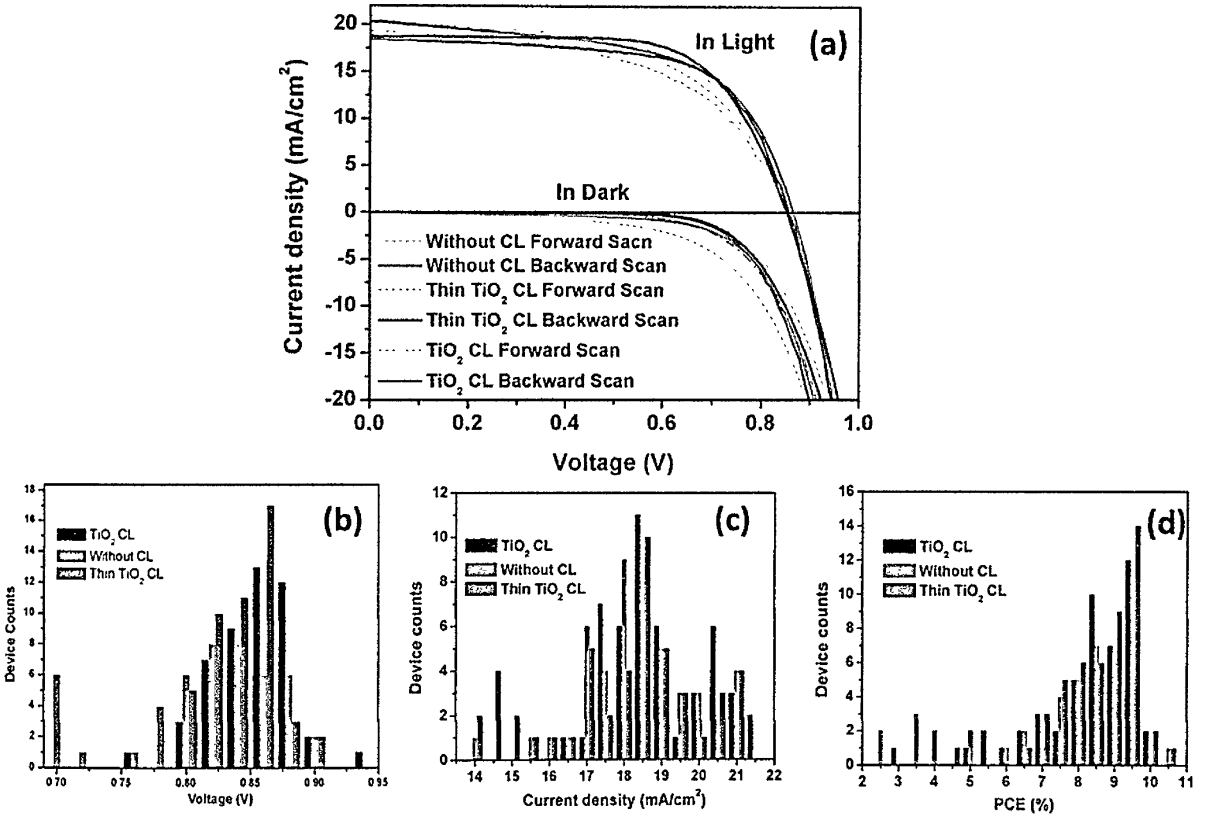

Figure 2.6: (a) Best performing device J-V characteristic curves and histogram plot of (b) V_{oc}, (c) J_{sc}, and (d) PCE of 48 devices of each kind of TiO_2 mesoporous perovskite solar cells; with TiO_2 CL (black), thin TiO_2 CL (blue), and without TiO_2 CL (orange).

2.3.3 Proposed recombination mechanism and open-circuit voltage decay (OCVD) measurement

Schematics of possible recombination mechanism in a TiO_2 based perovskite solar cells are shown in Fig. 2.7. The main recombination loss in TiO_2 mesostructured perovskite solar cells can be by the carriers recombining between excited electron in mesoporous TiO_2 and holes in perovskite or hole transporting layer (HTM) as shown in Fig. 2.7a. Such recombination process can be suppressed by surface passivation of TiO_2 particles.[10] However, TL of MgO, either on FTO or TiO_2 CL, cannot prevent the recombination between porous TiO_2 and perovskite or HTM, that is, recombination of carriers at perovskite and HTM interface remains unaffected by any change in the CL. Hence it can be inferred that significant increment in V_{oc} by MgO TL is unlikely due to the prevented back transfer from FTO to perovskite or HTM, which is already prevented by remnant PbI_2 and mesoporous TiO_2 layer (as evident from same V_{oc} for cells with and without CL) (Fig. 2.6 b).[17] Here important role of MgO is that electron once collected by FTO can never move back to TiO_2, where it ultimately undergoes a constant recombination due to trap states in the TiO_2 (Fig. 2.7 b). Prior report suggests that there exist lot of trap states in TiO_2 (or TiO_x) CL[18] which are basically of two types. The under-coordinated Ti^{4+} and oxygen vacancies acts as electron trap centers while the hydroxyl groups act as hole trap centers.[19, 20, 21, 22] These trap states can cause trap-assisted recombination within TiO_2 layer[20, 23, 22] as well as at the interface with perovskite resulting in loss in V_{oc} which was also evident from open-circuit coltage decay (OCVD) measurement. For performing OCVD measurement, the cells were kept under illumination for one minute and the light is then switched off. The voltage decay was monitored with time and the OCVD graph for cells with different cases is shown in Fig. 2.8. The device incorporating TiO_2-MgO bilayer and TiO_2 CL based cells showed similar decay confirming that there is a reasonable loss in V_{oc} within TiO_2 CL itself. In case of TiO_2-MgO bilayer devices, the recombination at FTO/TiO_2 interface are not prevented (Fig. 2.7 c) which is the reason for not showing much increment in V_{oc}. However, the light increment (from 0.86 V to 0.9 V) can be due to the coverage of TiO_2 CL and passivation of surface traps of TiO_2 CL by MgO TL. Also, research reports suggests that dehydrogenative condensation reaction of $Mg(OH)_2$, which is formed from the intermediate product from the precursor ($Mg(CH_3COO)_2$), is considered to improve the interface contact between CL and

mesoporous TiO_2.[15] As a result, J_{sc} showed increment in bilayer devices and exhibited highest PCE of 12% among all devices studied.

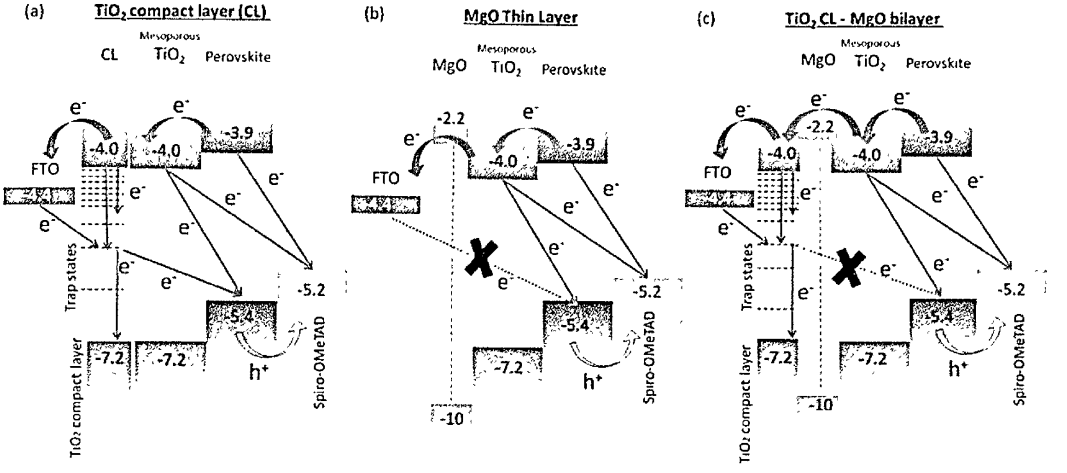

Figure 2.7: Schematic diagram showing possible recombination mechanisms in TiO_2 mesostructure perovskite solar cells with (a) TiO_2 CL, (b) MgO TL and (c) TiO_2-MgO bilayer.

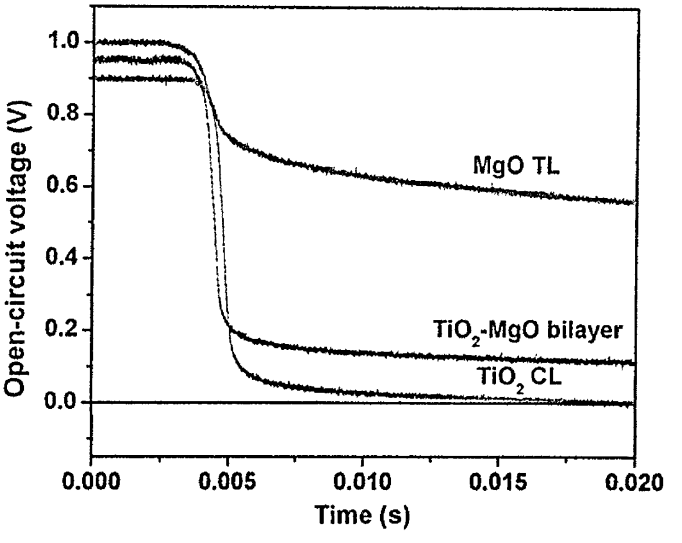

Figure 2.8: Open-circuit voltage decay (OCVD) measurement of TiO_2 CL (blue trace), MgO TL (red trace) and TiO_2-MgO bilayer (black trace).

Incorporation of MgO TL also tends to stabilize the cell performance as a result of reduced recombination. This was evident from wider distribution of device performance observed in case of cells with (thick and thin) and without TiO_2 CL (Fig. 2.6 d) in comparison to narrow distribution after incorporating MgO TL (both as independent and on top of TiO_2 CL) (Fig. 2.4 c) suggesting more uniform electrical property of MgO treated substrates.

In perovskite solar cells hysteresis in J-V plot obtained from forward and reverse scan directions is commonly observed phenomenon [24] and several reasons such as ferroelectric polarization,[25] charge carrier dynamics at the interface[26, 27, 28, 29] and ion migration[30] has been proposed in the literature. Herein, although the perovskite in bulk of mesostructured TiO_2 was the same, the cells with MgO TL showed reasonable hysteresis while the cells with TiO_2-MgO bilayer and TiO_2 CL exhibited negligible hysteresis (Fig. 2.4 d) indicating that hysteresis is much influenced by the carrier dynamics at the interfaces.[26, 27, 28, 29] Incorporation of MgO TL on FTO is believed to change the charge transfer rate at the interface of mesoporous TiO_2 and FTO resulting in enhanced hysteresis.

2.4 Conclusion

MgO incorporated in TiO_2 mesostructure perovskite solar cell as a thin tunneling barrier layer on FTO enhanced the V_{oc} of the cells significantly (from 0.86 to 0.98 V) while the MgO layer on 50-60 nm TiO_2 CL (TiO_2-MgO bilayer) did not show much change in V_{oc} (from 0.86 to 0.9 V) The above results revealed that there is a reasonable recombination loss by trap assisted recombination within TiO_2 itself and by back transfer of electron from FTO to TiO_2 (as a minor effect). Therefore, the enhancement in V_{oc} by the MgO TL is most likely due to blocking the recombination pass way at FTO/TiO_2 interface, not at TiO_2/perovskite or TiO_2/Spiro-OMeTAD interface. Moreover, the cells with and without TiO_2 CL showed same V_{oc}, which confirmed that the TiO_2 CL does not necessarily help in preventing back transfer of electron from FTO to perovskite or HTM. Further investigation is needed to understand thoroughly the mechanism of recombination and its suppression by MgO at FTO/TiO_2 interface. However, our results suggest that interfacial modification on conductive FTO with thin tunneling barrier layer can further enhance the performance of perovskite solar cells.

2.5 References

1 Kojima, A., Teshima, K., Shirai, Y., Miyasaka, T., *J. Am. Chem. Soc*, **2009**, *131*, 6050-6051.

2 Miyasaka, T., *Chem. Lett.*, **2015**, *44*, 720-729.

3 Best solar cell efficiency chart. Available at http://www.nrel.gov/ncpv/images/efficiency_chart.jpg accessed on (3rd Dec, 2017).

4 Stranks, S. D., Eperon, G. E., Grancini, G., Menelaou, C., Alcocer, M. J. P., Leijtens, T., Herz, L. M., Petrozza, A., Snaith, H. J., *Science*, **2013**, *342*, 341-344.

5 Sun, S. Y., Salim, T., Mathews, N., Duchamp, M., Boothroyd, C., Xing, G. C., Sum, T. C., Lam, Y. M., *Energy & Environmental Science*, **2014**, *7*, 399-407.

6 Xing, G. C., Mathews, N., Sun, S. Y., Lim, S. S., Lam, Y. M., Grätzel, M., Mhaisalkar, S., Sum, T. C., *Science*, **2013**, *342*, 344-347.

7 Zuo, L., Gu, Z., Ye, T., Fu, W., Wu, G., Li, H., Chen, H., *J. Am. Chem. Soc.*, **2015**, *137 (7)*, 2674-2679.

8 Liu, L., Mei, A., Liu, T., Jiang, P., Sheng, Y., Zhang, L., Han, H., *J. Am. Chem. Soc.*, **2015**, *137 (5)*, 1790-1793.

9 Wang, J., Qin, M., Tao, H., Ke, W., Chen, Z., Wan, J., Qin, P., Xiong, L., Lei, H., Yu, H., Fang, G., *Appl. Phys. Lett.*, **2015**, *106*, 121104.

10 Han, G. S., Chung, H. S., Kim, B. J., Kim, D. H., Lee, J. W., Swain, B. S., Mahmood, K., Yoo, J. S., Park, N.-G., Lee, J. H., Jung, H. S., *J. Mater. Chem. A.*, **2015**, *3*, 9160-9164.

11 Yue, Y., Yang, X., Wu, Y., Salim, N. T., Islam, A., Noda, T., Han, L., *ChemSusChem.*, **2015**, *8 (16)*, 2625-2629.

12 Ke, W., Fang, G., Wan, J., Tao, H., Lin, Q., Xiong, L., Qin, P., Wang, J., Lei, H., Yang, G., Qin, M., Zhao, X., Yan, Y., *Nature Communications*, 2016, 6, DOI:10.1038/ncomms7700.

13 Liu, D., Yang, J. Kelly, T. M., *J. Am. Chem. Soc.*, **2014**, *136*, 17116-17122.

14 Song, J., Zheng, E., Bian, J., Wang, X.-F., Tian, W., Sanehira, Y., Miyasaka, T., *J. Mater. Chem. A.*, **2015**, *3*, 10837-10844.

15 Sakai, N., Ikegami, M., Miyasaka, T., *Appl. Phys. Lett.*, **2014**, *104 (6)*, 063303.

16 Chandiran, A. K., Nazeeruddin, M. K., Grätzel, M., *Adv. Funct. Mater.*, **2014**, *24 (11)*, 1615-1623.

17 Cao, D. H., Stoumpos, C.C., Malliakas, C. D., Katz, M. J., Farha, O. K., Hupp, J. T., Kanatzidis, M. G., *APL Mater.*, **2014**, *2*, 091101.

18 Yuan, Z., Wu, Z., Bai, S., Xia, S., Xu, W., Song, T., Wu, H., Xu, L., Si, J., Jin, Y., Sun, B., *Adv. Energy Mater.*, **2015**, *5 (10)*, DOI: 10.1002/aenm.201500038

19 Mercado, C. C., Knorr, F. J., McHale, J. L., Usmani, S. M., Ichimura, A. S., Saraf, L. V., *J. Phys. Chem. C.*, **2012**, *116*, 10796-10804.

20 Wang, X., Feng, Z., Shi, J., Jia, G., Shen, S., Zhou, J., Li, C., *Phys. Chem. Chem. Phys.*, **2010**, *12*, 7083-7090.

21 Peter, L. M., *Phys. Chem. Chem. Phys.*, **2010**, 9, 2630-2642.

22 Bertoluzzi, L., Herraiz-Cardona, I., Gottesman, R., Zaban, A., Bisquert, J., *J. Phys. Chem. Lett.*, **2014**, *5*, 689-694.

23 Wehrenfennig, C., Palumbiny, C. M., Snaith, H. J., Johnston, M. B., Schmidt-Mende, L., Herz, L. M., *J. Phys. Chem. C.*, **2015**, *119*, 9159-9168.

24 Snaith, H. J., Abate, A., Ball, J. M., Eperon, G. E., Leijtens, T., Noel, N. K., Stranks, S. D., Wang, J. T.-W., Wojciechowski, K., Zhang, W., *J. Phys. Chem. Lett.*, **2014**, *5 (9)*, 1511-1515.

25 Chen, H.-W., Sakai, N., Ikegami, M., Miyasaka, T., *J. Phys. Chem. Lett.*, **2015**, *6 (1)*, 164-169.

26 Zhang, H., Liang, C., Zhao, Y., Sun, M., Liu, H., Liang, J., Li, D., Zhang, F., He, Z., *Phys. Chem. Chem. Phys.*, **2015**, *17*, 9613-9618.

27 Wojciechowski, K., Stranks, S. D., Abate, A., Sadoughi, G., Sadhanala, A., Kopidakis, N., Rumbles, G., Li, C.-Z., Friend, R.-H., Jen, A. K.-Y., Snaith, H. J., *ACS Nano.*, **2014**, *8 (12)*, 12701-12709.

28 Shao, Y., Xiao, Z., Bi, C., Yuan, Y., Huang, J., *Nature Communications*, **2014**, *5*, DOI:10.1038/ncomms6784.

29 Jena, A. K., Chen, H.-W., Kogo, A., Sanehira, Y., Ikegami, M., Miyasaka, T., *ACS Appl. Mater. Interfaces*, **2015**, *7 (18)*, 9817-9823.

30 Eames, C., Frost, J. M., Barnes, P. R. F., O'Regan, B. C., Walsh, A., Islam, M. S., *Nature Communications,* **2015**, *6*, DOI:10.1038/ncomms8497.

Chapter 3

Study The Effect of Various TiO_2 Electron Transporting Materials on $(CH_3NH_3)_3Bi_2I_9$ – A Zero Dimensional Perovskite Material for Photovoltaic Applications.

Abstract

In this work, non-toxic, high stable methylammonium iodobismuthate ($(CH_3NH_3)_3Bi_2I_9$) (MIB) perovskite is introduced as an alternative to rapidly progressing hybrid organic-inorganic lead perovskite material. Morphology of polycyrstalline films of hybrid perovskite $(CH_3NH_3)_3Bi_2I_9$, produced by simple solution spin coating process and subsequent heating, is influenced drastically by the nature of substrates. The optical measurements exhibited a strong absorption band at around ~500 nm. Photovoltaic devices made with anatase mesoporous TiO_2 layer demonstrated better performance with current density over 0.8 mA/cm^2 in comparison to devices with brookite mesoporous TiO_2 and planar (free of porous layer) which showed inefficient performance. Additionally, devices with anatase mesoporous TiO_2 were stable to ambient conditions for more than 10 weeks.

3.1 Introduction

The development of renewable energy is one of the vital issues of the present century and solar energy can be an important contributor to future energy production whereas the production of solar cells is rapidly increasing with comprehensive decrease in solar cells price. However, in order to grow a large-scale energy source and to compete with other energy generation sources, the production cost of solar cells must be reduced further. Recently, the next generation solar cells employing hybrid organic-inorganic halide perovskites (AMX_3 where A = $CH_3NH_3^+$, Cs^+, M = Pb^{2+}, Sn^{2+} and X = I^-, Br^-, Cl^-) as an active absorption layer have gained huge attention and established as a major field of research since the pioneering work by Miyasaka et al.[1,2] In a short period of time, certified power conversion efficiency (PCE) of 22.7% has been achieved, nearly approaching the performance of mature technologies.[3,4,5] The hybrid lead halide perovskites possess excellent properties such as high absorption coefficient, bandgap tune-ability,[6,7] long carrier diffusion length, photon recyclability[8,9,10] and they can be produced by low cost solution processes.[11,12,13,14,15] Despite of demonstrating almost vertical growth in device performance, perovskite solar cells faces several issues which needed to be addressed. In addition to consistent fabrication processes and stability, the toxicity of lead (Pb) is presently a major disadvantage with the lead based perovskite solar cells. The primary challenge is to replace or reduce the content of lead in the perovskite with a non-toxic element. Efforts have been made to replace toxic lead with tin (Sn)[16,17,18,19] and due to its small bandgap, Sn perovskites can produce high short-circuit current densities (J_{sc}) compared to its lead counterparts. However, the device performance and open-circuit voltage (V_{oc}) of Sn-based perovskite has been limited by bulk recombination (due to self-doping effect) and in addition the stability of Sn-perovskite in ambient condition is very poor. Hence, all the processes need to be carried out in nitrogen gas atmosphere to avoid the degradation. The other perovskite materials without Pb also been reported which showed low power conversion efficiency (PCE) compared to lead-halide perovskites, however, their stability is superior and also exhibit other functionalities.[20,21,22,23,24,25] Among various materials studied, methylammonium iodobismuthate (MIB) ($(CH_3NH_3)_3Bi_2I_9$) exhibits promising optoelectronic properties.[26,27,28,29,30,31,32] However, their photovoltaic properties was first reported by Park et

al. in which they studied the photovoltaic characteristics of $Cs_3Bi_2I_9$, $MA_3Bi_2I_9$ and $MA_3Bi_2I_{9-x}Cl_x$ materials using a single step coating which were found to be very low.[33] Lyu et al. demonstrated promising stability of $MA_3Bi_2I_9$ perovskite in thick mesoporous configuration.[34] Further, Oez et al. incorporated $MA_3Bi_2I_9$ perovskite in inverted architecture and observed low power conversion efficiency of 0.1% with high stability in ambient condition.[35]

Herein, bismuth (Bi) based halide perovskite ($(CH_3NH_3)_3Bi_2I_9$) was prepared by combining bismuth iodide and methylammonium iodide in 2:3 molar ratio and incorporated in planar and mesoporous device architecture via a simple, low temperature solution process. A detailed morphological, structural and optoelectronic properties are studied for suitable device fabrication. A comparative study of perovskite formation on mesoporous (anatase and brookite TiO_2) and planar structure and its strong dependence on the kind of TiO_2 and device architecture is performed. Although, the device with anatase mesoporous TiO_2 layer demonstrated PCE of 0.2% which is still low, they exhibits long term stability up to 10 weeks in ambient air. Nevertheless, the results adequately evidence that morphology can play a significant role in improving the cell efficiency of MIB perovskites. The development in low temperature processing of MIB can address both the toxicity and stability issues of lead-based perovskites.

3.2 Experimental

3.2.1 Methylammonium iodide synthesis

Methylammonium iodide was synthesized by mixing equimolar amount of hydroiodic acid (HI) and methylamine in a flask. HI (57 wt.% in water, Wako) was added to methylamine solution (40% in ethanol, Wako) drop by drop with gently stirring and nitrogen purging in ice bath. The reaction was stirred for two hours and the white CH_3NH_3I precipitation was recovered by carefully evaporating solvent using rotor-vapour. Recrystallization was conducted to purify the product via ethanol and diethyl ether for 10 hours. The final product was washed by diethyl ether several times and then drying at 45 ^{O}C vacuum oven overnight.

3.2.2 Device fabrication

Fluorine doped SnO_2 (FTO) (10 Ω/□, NSG Group, Japan) conductive and transparent glass substrates were patterned using zinc powder and 3 M HCl aqueous solution and ultrasonically cleaned with 2% Hellmanex in water, deionized water, acetone and ethanol sequentially for 15 minutes each and thoroughly dried with nitrogen. All the chemicals in this study were used as received, without further purification.

3.2.2.1 TiO_2 compact layer coating

TiO_2 compact layer (CL) was spin coated onto cleaned FTO glass substrates by using 0.15 M titanium diisopropoxide bis-(acetylacetonate) $(Ti\text{-}acac)_2$ (75 wt.% in isopropanol, Sigma-Aldrich) in a 2-propanol (99.9% Wako) solution at 3000 rpm for 30 seconds, followed by drying at 125 ^{O}C for 5 minutes and cooled down to room temperature. Further two successive coating (3000 rpm, 30 sec) from 0.3 M $(Ti\text{-}acac)_2$ solution were deposited and dried at 125 ^{O}C for 5 minutes followed by sintering at 500 ^{O}C for 30 minutes in a muffle furnace. The TiO_2 coated FTO substrates were further treated with 40 mM $TiCl_4$ aqueous solution at 70 ^{O}C for 60 minutes. The $TiCl_4$ treated samples were thoroughly washed with distilled water and dried in nitrogen followed by sintering again at 500 ^{O}C for 30 minutes in muffle furnace.

3.2.2.2 TiO_2 mesoporous coating

The anatase mesoporous layer was spin coated using a commercial TiO_2 paste (18-NRT, Dyesol, particle size ~20 nm) diluted in 25 wt.% ethanol at 4000 rpm for 30 sec and the coated substrates were then sintered at 500 ^{O}C for 1 hour in a muffle furnace. An aqueous brookite TiO_2 paste (PECC-B01, Peccell Technologies, Inc., particle size ~10-20 nm) was diluted to 33 vol.% with ethanol and spin coated on TiO_2 CL coated substrates at 3000 rpm for 30 sec. The substrates were annealed at 300 ^{O}C for 1 hour in a muffle furnace. Prior to bismuth perovskite coating, the substrates without any mesoporous layer (planar substrate) and substrates coated with brookite and anatase mesoporous layers were treated with UV-ozone for 10 minutes.

3.2.2.3 Bismuth perovskite ($(CH_3NH_3)_3Bi_2I_9$) and HTM deposition

2:3 Molar ratio of bismuth triiodide (BiI_3) and CH_3NH_3I (MAI) (20 wt.%) were dissolved in DMF with constant stirring at 50 ^{O}C for 30 minutes prior to the coating. The precursor solution was spin coated on UV-ozone treated ETL coated FTO substrates at 2000 rpm for 30 sec. After spin coating, the samples were transferred to the hot plate which was set at 100 ^{O}C for 90 min. to form an orange coloured layer of perovskite. The hole transporting material (HTM) was spin0coated at 2000 rpm for 30 sec from 8 wt.% solution of spiro-OMeTAD in chlorobenzene solution containing additives of lithium bis(trifluoromethanesulfonyl) imide and 4-tert-butylpyridine followed by overnight oxidation of spiro-OMeTAD. Finally, Au metal electrode (ca. ~90 nm in thickness) was thermally evaporated on top of the HTM to complete the device fabrication.

3.2.3 Characterization

The photovoltaic characteristics of all devices with an active area of 0.09 cm^2 (defined by black mask) were measured with Keithley 2400 source meter under 1 sun illumination (AM 1.5 G, 100 mW/cm^2) using a Peccell Technologies PEC-L01 solar simulator. The external quantum efficiency (EQE) spectra of the devices were measured in air at room temperature using Peccell Technologies, PEC-S20 action spectrum measurement setup. The structural, optical and morphological analysis were carried out using X-ray diffractometer (D8 Discover, Brucker) with CuKα radiation source, UV-vis spectrophotometer (UV-Vis 1800, Shimazdu) and scanning electron microscope (SU8000, HITACHI) respectively.

3.3 Results and discussion

3.3.1 Characterization of MBI perovskite on various TiO_2 ETL

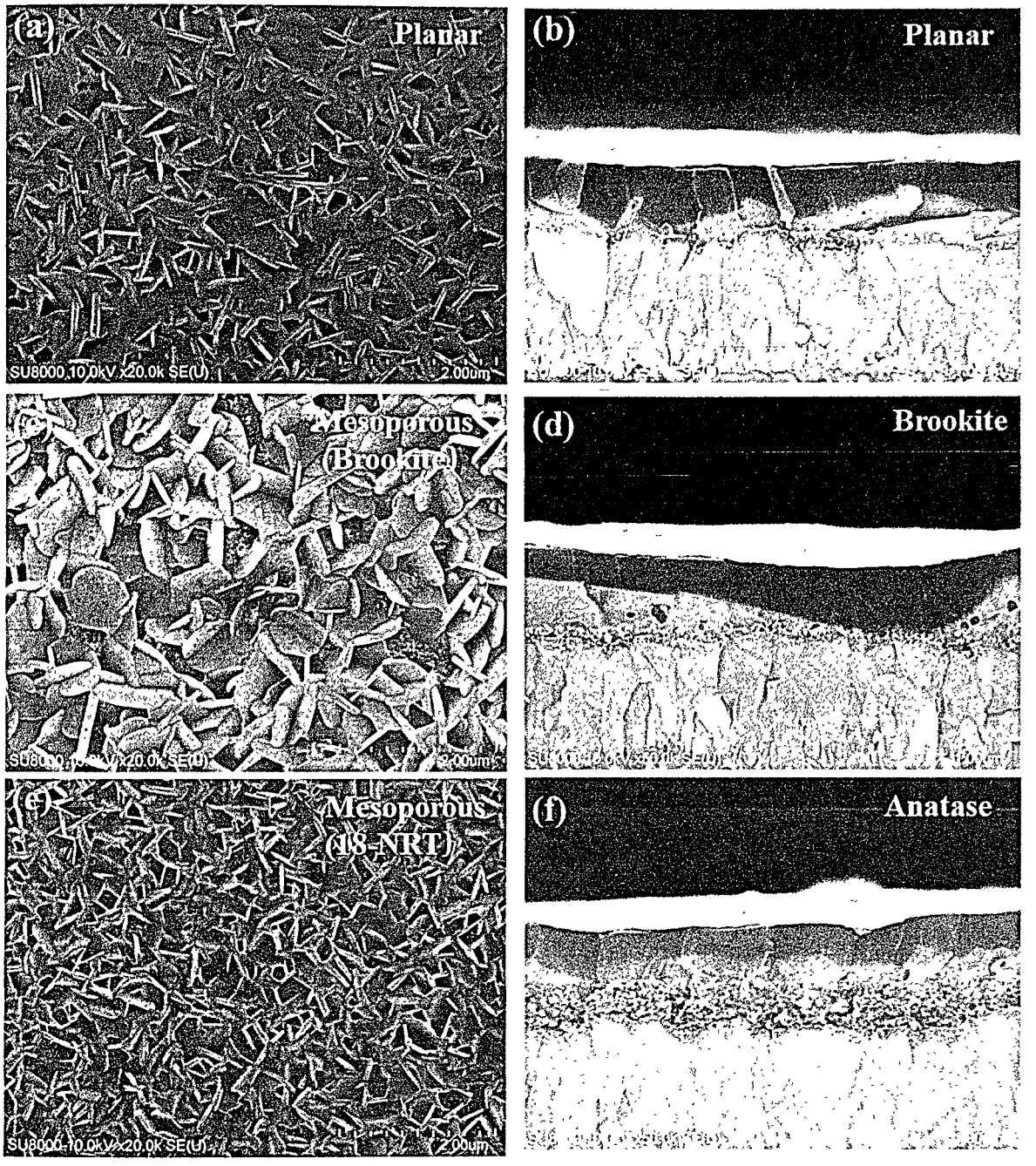

Figure 3.1: Top and cross section SEM image of MBI perovskite layer deposited on (a-b) TiO_2 compact layer, (c-d) Brookite mesoporous and (e-f) Anatase mesoporous.

Figure 3.1 displays the top view SEM image of MBI films and cross-sectional view SEM images of different stacking layers of perovskite devices of different architectures. Morphology of MBI perovskite on TiO_2 CL (planar structured cell) differed slightly from that on mesoporous (brookite and anatase TiO_2) substrates (Fig. 3.1 a, c, e). Surface coverage of anatase and planar substrate with MBI was found to be similar and better than for brookite. From the cross-sectional view it can be seen that the HTM layer touches the mesoporous layer in case of brookite mesoporous film (Fig. 3.1d). For planar and anatase case, the capping layer of MBI devices resembles smooth interfaces (Fig. 3.1 b, f). These results reflect the surface properties of substrates affect the morphological properties of MBI perovskite layers dramatically.

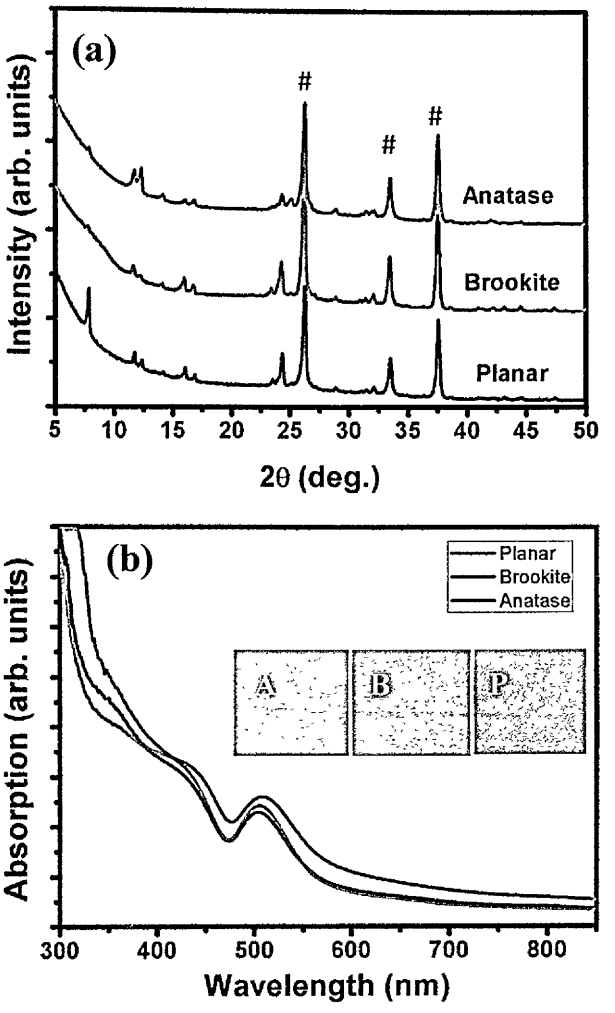

Figure 3.2: XRD of MBI perovskite grown on planar and mesoporous (anatase and brookite layer) (# corresponds to FTO peaks) and (b) UV-vis spectra of MBI perovskite (Inset of Fig. 3.2.b, shows the visual image of A = Anatase, B = Brookite and P = Planar).

The crystal structure of MBI perovskite was further determined from X-ray diffraction measurement as shown in Fig. 3.2a. The diffraction peaks were resolved in the $P6_3/mmc$ space group[36] and well matches with previous literatures. The diffraction peaks of MBI on all the three substrates showed close matching with each other except the intensity of the peak at lower angle ($2\theta = 7.5^{O}$) on planar TiO_2 CL was slightly higher compared to the other two. The enhancement in the intensity at lower angle can be attributed to the effect of scaffolds. Also, the absorption measurement showed the absorption band around ~500 nm

in all the samples and brookite samples has higher absorption due to greater thickness of perovskite film. However, there was no change in the visual colour of all the three samples (inset in Fig. 3.2b).

3.3.2 Device performance and long term stability

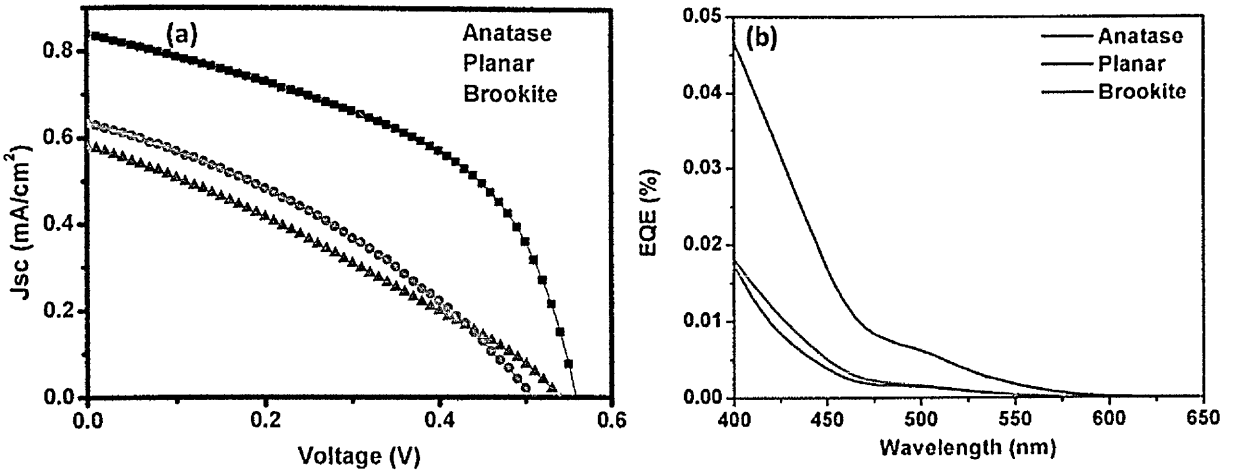

Figure 3.3: (a) J-V characteristic curves and (b) EQE spectra of best performing MBI devices in both device architectures (planar and mesoporous).

MBI perovskite solar cells with the all the three configurations (planar, mesoporous brookite and anatase TiO_2) were prepared following the same experimental procedure, as described above to study the influence of different substrates/morphology on the final photovoltaic performance. Fig. 3.3a compares the current density (J)-voltage (V) characteristics of all the three photovoltaic devices measured under standard conditions. The EQE spectra of all devices (Figure 3.3b) showed an edge at around ~620 nm indicating similar spectral response of MBI perovskite and integrated photocurrent density from EQE is well matched with the values obtained from standard illumination at 1 Sun. As can be seen from J-V characteristic curves (Fig. 3.3a), MBI perovskite solar cells prepared on anatase TiO_2 mesoporous layer showed better photovoltaic performance in comparison to planar and brookite mesoporous case. In case of brookite mesoporous and planar structured cells resulted poor characteristics in all the device parameters of J_{sc}, V_{oc} and FF indicating that these cells undergo large recombination and/or high internal resistance. Because carrier transfer resistance is directly influenced by junction structure between scaffold and MBI, it

is rationalized that physical junction was poorly formed in case of brookite and planar scaffolds. The higher photocurrent of anatase TiO_2 MBI cells can also be attributed to better surface coverage (Table 1). Also, from EQE spectra the integrated Jsc for planar, anatase mesoporous and brookite mesoporous are 0.4 mA/cm^2, 0.65 mA/cm^2 and 0.35 mA/cm^2 respectively. This result shows that MBI perovskites for photovoltaic applications depends strongly on the compact layer and kind of scaffold employed. As can be seen, perovskite solar cells prepared on anatase TiO_2 mesoporous layer showed better results in terms of conversion efficiency, open-circuit voltage and short-circuit current in comparison to planar and brookite mesoporous perovskite devices. An important correlation between various device parameters of all the studied device architecture has been observed as shown in Fig. 3.4

Table 3.1: Device parameters of best performing MBI perovskite in planar and mesoporous architecture

Device architecture	J_{sc} (mA/cm^2)	V_{oc} (V)	FF	PCE (%)
Anatase	0.83	0.56	0.48	0.259
Planar	0.61	0.51	0.33	0.108
Brookite	0.57	0.53	0.3	0.0942

As evident from cross-sectional SEM image (Fig. 3.1), brookite and planar MBI samples formed non-uniform perovskite capping layer which lead to the increased shunting pathway because of contact between spiro-OMeTAD and TiO_2 compact layer (in case of brookite mesoporous). Additionally, perovskite loading is very poor in case of thicker brookite mesoporous layer which is in contrary to the lead based perovskite which can be due to strong inter particle necking of brookite leading to smaller pores and fast crystallization of MBI.[37,38,39] In contrast, in case of anatase TiO_2 mesoporous, being rich of pores, the film shows better coverage and interfaces of various layer are smooth compared to

planar and brookite. The continuous interface in anatase TiO_2 based MBI devices reduces junction resistance as well as charge recombination and produces higher V_{oc} as well as J_{sc}.

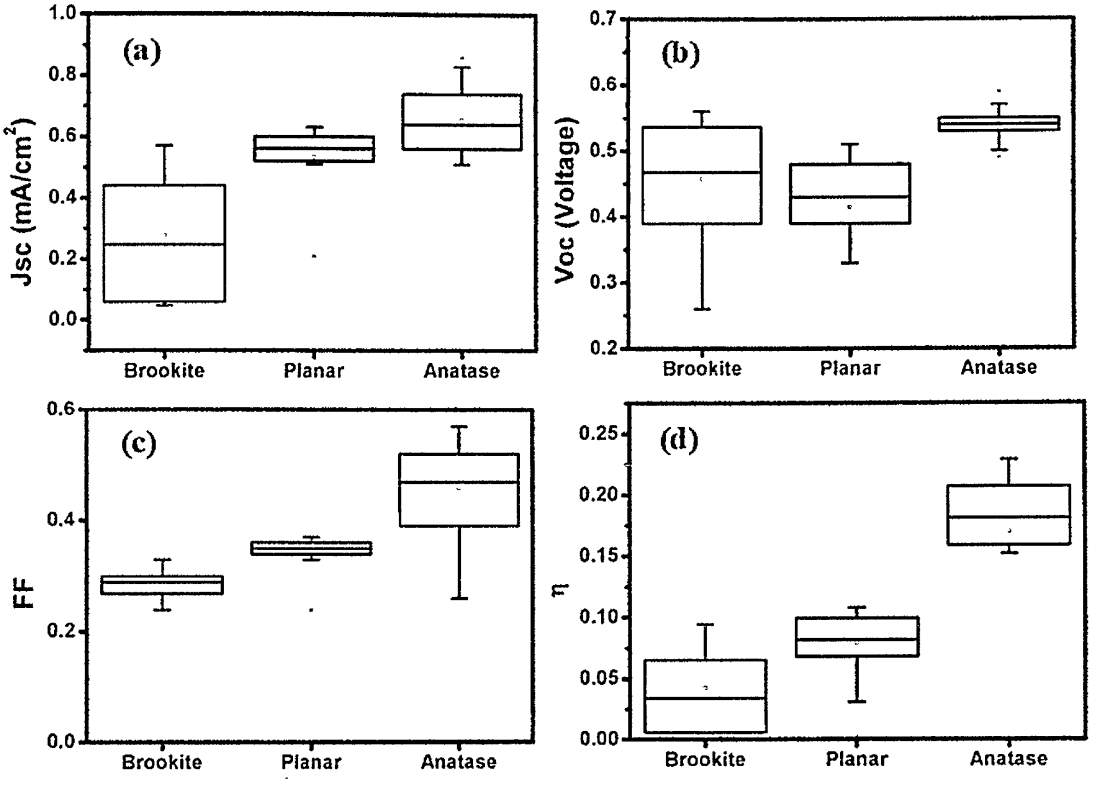

Figure 3.4: Device performance at optimized conditions using different device architectures measured under simulated AM 1.5 sunlight of 100 mW/cm^2 irradiance. The data are represented as standard box plot with (a) short-current photocurrent density (J_{sc}), (b) open-circuit voltage (V_{oc}), (c) Fill Factor (FF) and (d) power conversion efficiency (η) of measured devices. Number of devices is not mentioned here (24 devices in each case).

According to prior reports, carrier density of MBI is ~10^{16} cm^{-3}, which is 7 orders of magnitude higher than lead perovskite ($MAPbI_3$) (10^9 cm^{-3}).[40] Such high background carrier densities in the light absorber can contribute to the bulk recombination which further influence and reduce FF. Other factors that can drastically change the device performance are the presence of defects and impurities in MBI, however, no additional absorption band in UV-vis spectra (Fig. 3.2b) and also no impurity phase in XRD pattern is observed. In the present study, MBI perovskite devices showed almost negligible hysteresis in all the device

configurations (Fig. 3.5a). The long term stability of best performing devices showed stable performance after 10 weeks after exposing the devices to ambient atmosphere without any sealing (Fig. 3.5b).

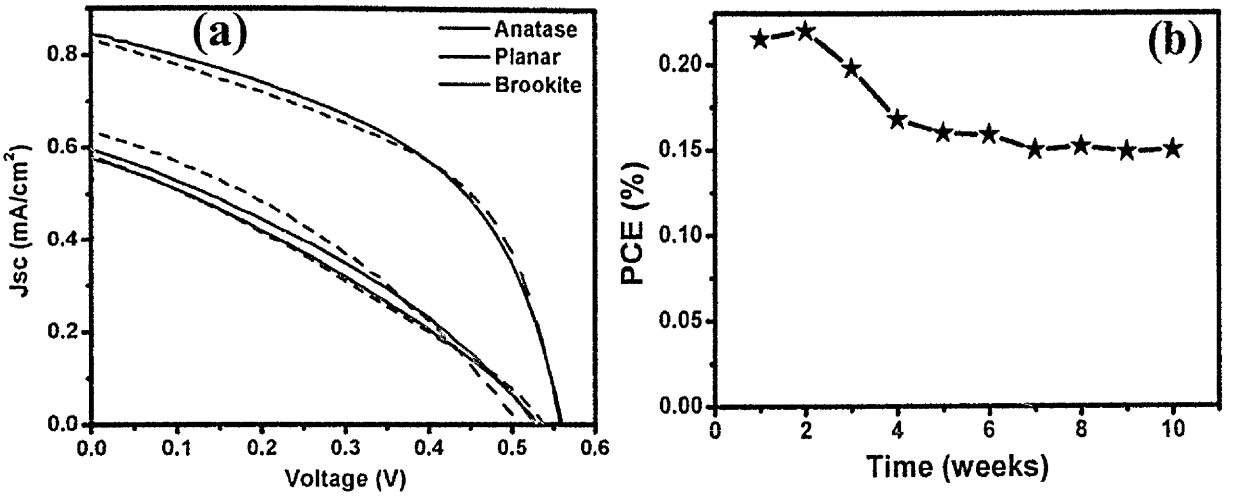

Figure 3.5: (a) J-V curve of best performing MBI devices grown on planar TiO_2 and mesoporous TiO_2 with forward and reverse scan direction at scanning speed of 50 mV/sec, (b) Lone term stability of MBI perovskite cells without encapsulation stored and measured in ambient condition.

Based on the obtained results, the critical issue to enhance the performance of bismuth perovskite must be structuring of continuous interfaces at collector-perovskite heterojunction and suppression of recombination at the interfaces including grain-grain inter-structure of perovskite crystals. With spectral sensitivity of photon collection (<620 nm), it can be estimated that MBI perovskite has potential to yield J_{sc} as high as 10 mA/cm^2. The corresponding efficiency level with V_{oc} of 1V is around ~8%. The thickness of the MBI perovskite absorber is also limited by the carrier diffusion length. Assuming 100 nm thick MBI perovskite film, efficiency is limited to <4%. Present study shows that there are large room for improvements in the quality of MBI perovskite absorber via controlling the growth and nucleation of MBI crystals and appropriate choice of substrates as the degree of lattice mismatching also plays a pivotal role in preferential growth and nucleation. Also, controlling the I/Bi stoichiometry is essential in the crystallization process. Optoelectronic properties such as light absorption coefficient are also sensitive to the stoichiometry of

organic halide and choice of salts as the final film is not only sensitive to experimental conditions (stoichiometry, solvent, heating etc.), but can be predetermined via desired/undesired colloids in the precursor solutions. These improvements will lead to minimize the recombination and enhance the photovoltaic parameters of the bismuth based organic-inorganic perovskite materials. Further optimization of the growth conditions and preparations is required to exploit maximum potential of MBI.

3.4 Conclusion

Facile synthesis of MBI perovskite at low temperature via single step spin coating of stoichiometric solution of bismuth triiodide and methylammonium iodide in DMF is demonstrated. The suitable device configuration of MBI perovskite using planar, brookite and anatase mesoporous layer for efficient perovskite photovoltaics have been investigated. MBI perovskite morphology depends strongly on the compact and mesoporous layer on the FTO substrates. MBI layer on TiO_2 CL is not continuous which further facilitates the non-uniform growth, however, in case of mesoporous layers the nucleation and growth is uniform. In case of brookite mesoporous layer, the inter particle necking impedes the MBI percolation in the pores and hampers the nucleation and uniform growth of MBI. The photovoltaic analysis showed improved performance with 0.2% PCE with good stability of devices for 10 weeks in ambient condition. Furthermore, the present study demonstrated that the MBI perovskite has emerged as a very promising material for use in optoelectronic devices particularly in hybrid solar cells.

3.5 References

1 Kojima, A.; Teshima, K.; Shirai, Y.; Miyasaka, T., *J. Am. Chem. Soc.* **2009**, *131*, 6050-6051.

2 Miyasaka, T, *Chem. Lett.*, **2015**, *44*, 720-729

3 NREL Best research-cell efficiencies, http://www.nrel.gov/ncpv/images/efficiency_chart.jpg.

4 Wang, D. L.; Cui, H. J.; Hou, G. J.; Zhu, Z. G.; Yan, Q., B.; Su, G, *Scientific Reports*, **2016**, *6*, 18922.

5 Bi, D.; Tress, W.; Dar, M. I.; Gao, P.; Luo, J.; Renevier, C.; Schenk, K.; Abate, A.; Giordano, F.; Baena, J.-P., C; Decoppet, J. D.; Zakeeruddin, S. M.; Nazeeruddin, M. K.; Grätzel, M.; Hagfeldt, A, *Sci. Adv.* **2016**, 2:e1501170.

6 Noh, J., H.; Im, S., H.; Heo, J., H.; Mandal, T., N.; Seok, S. I, *Nano Lett.*, **2013**, *13*, 1764-1769.

7 Yin, W.-J.; Yang, J. H.; Kang, J.; Yan, Y.; Wei, S.-H, *J. Mater. Chem. A*, **2015**, *3*, 8926-8942.

8 Stranks, S. D.; Eperon, G. E.; Grancini, G.; Menelaou, C.; Alcocer, M. J. P.; Leijtens, T.; Herz, L. M.; Petrozza, A.; Snaith, H. J, *Science*, **2013**, *342*, 341-344.

9 Fang, Y.; Shao, Y.; Mulligan, P.; Qiu, J.; Cao, L.; Huang, J, *Science*, **2015**, *347*, 967.

10 Shi, D.; Adinol, V.; Comin, R.; Yuan, M.; Alarousu, E.; Buin, A.; Chen, Y.; Hoogland, S.; Rothenberger, A.; Katsiev, K.; Losovyj, Y.; Zhang, X.; Dowben, P. A.; Mohammed, O., F.; Sargent, E., H.; Bakr, O., M, *Science*, **2015**, *347*, 519.

11 Liu, M.; Johnston, M., B.; Snaith, H., J, *Nature*, **2013**, *501*, 395.

12 Malinkiewicz, O.; Yella, A.; Lee, Y., H.; Espallargas, G., M.; Graetzel, M.; Nazeeruddin, M., K.; Bolink, H., J, *Nat. Photonics*, **2014**, *8*, 128-132.

13 Chen, C.-W.; Kang, H.-W.; Hsiao, S.-Y.; Yang, P.-F.; Chiang, K.-M.; Lin, H.-W, *Adv. Mater.*, **2014**, 26, 6647-6652.

14 Wang, F.; Yu, H.; Xu, H.; Zhao, N, *Adv. Funct. Mater.*, **2015**, 25, 1120-1126.

15 Singh, T.; Miyasaka, T., *Chem. Commun.*, **2016**, 52, 4784-4787.

16 Hao, F.; Stoumpos, C., C.; Cao, D., H.; Chang, R., P., H.; Kanatzidis, M., G, *Nature Photonics,* **2014**, *8*, 489–494.

17 Kumar, M., H.; Dharani, S.; Leong, W., L.; Boix, P., P.; Prabhakar, R., R.; Baikie, T.; Shi, C.; Ding, H.; Ramesh, R.; Asta, M.; Graetzel, M.; Mhaisalkar, S., G.; Mathews, N, *Adv. Mater.* **2014**, 26 (41), 7122-7127.

18 Noel, N., K.; Stranks, S., D.; Abate, A.; Wehrenfennig, C.; Guarnera, S.; Haghighirad, A.-A.; Sadhanala, A.; Eperon, G., E.; Pathak, S., K.; Johnston, M., B.; Petrozza, A.; Herz, L., M.; Snaith, H., J, *Energy Environ. Sci.* **2014,** 7, 3061–3068.

19 Sabba, D.; Mulmudi, H., K.; Prabhakar, R., R.; Krishnamoorthy, T.; Baikie, T.; Boix, P., P.; Mhaisalkar, S.; Mathews, N, *J. Phys. Chem. C.,* **2015**, 119, 1763-1767.

20 Yang, S., Y.; Martin, L., W.; Byrnes, S., J.; Conry, T., E.; Basu, S., R.; Paran, D.; Reichertz, L.; Ihlefeld, J.; Adamo, C.; Melville, A.; Chu, Y.-H.; Yang, C.-H.; Musfeldt, J., L.; Schlom, D., G.; Ager III, J., W.; Ramesh, R, *Appl. Phys. Lett.* **2009**, *95*, 062909.

21 Choi, T.; Lee, S.; Choi, Y., J.; Kiryukhin, V.; Cheong, S.-W, *Science,* **2009**, 324, 63-66,

22 Chakrabartty, J., P.; Nechache, R.; Harnagea, C.; Rosei, F, *Opt. Express,* **2014**, 22, A80.

23 Grinberg, I.; West, D., V.; Torres, M.; Gou, G.; Stein, D., M.; Wu, L.; Chen, G.; Gallo, E., M.; Akbashev, A., R.; Davies, P., K.; Spanier, J., E.; Rappe, A., M, *Nature,* **2013,** 503, 509-512.

24 Nechache, R.; Harnagea, C.; Li, S.; Cardenas, S.; Huang, W.; Chakrabartty, J.; Rosei, F, *Nat. Photon.*, **2015**, 9, 61-67.

25 Brandt, R., E.; Kurchin, R., C.; Hoye, R., L., Z.; Poindexter, J., R.; Wilson, M., W., B.; Sulekar, S.; Lenahan, F.; Yen, P., X., T.; Stevanović, V.; Nino, J., C.; Bawendi, M., G.; Buonassisi, T, *J. Phys. Chem. Lett.,* **2015**, *6*, 4297-4302.

26 Kawai, T.; Ishii, A.; Kitamura, T.; Shimanuki, S.; Iwata, M.; Ishibashi, Y, *J. Phys. Soc. Jpn.*, **1996**, *65*, 1464-1468.

27 Kawai, T.; Shimanuki, S, *phys. stat. sol. (b)* **1993**, 177, K43.

28 Lindqvist, O, *Acta Chem. Scand.*, **1968**, 22, 2943-2952,

29 Arakcheeva, A., V.; Bonin, M.; Chapuis, G.; Zaitsev, A., I, *Z. Kristallogr.***1999**, 214, 279.

30 Arakcheeva, A., V.; Chapuis, G.; Meyer, M, *Z. Kristallogr.* **2001**, 216, 199,

31 Szklarz, P.; Pietraszko, A.; Jakubas, R.; Bator, G.; Zielinski, P.; Galazka, M, *J. Phys.,* **2008**, 20, 255221,

32 Hoye, R.; Brandt, R., E.; Osherov, A.; Stevanovic, V.; Stranks, S., D.; Wilson, M., W., B.; Kim, H.; Akey, A., J.; Kurchin, R., C.; Poindexter, J., R.; Wang, E., N.; Bawendi, M., G.; Bulovic, V.; Buonassisi, T, *Chem. Eur. J.,* **2016**, 22, 2605-2610.

33 Park, B. W.; Philippe, B.; Zhang, X.; Rensmo, H;, Boschloo, G., Johansson, E., M., *Adv. Mater.* **2015,** 27(43) 6806-6813.

34 Lyu, M.; Yun, J.-H.; Cai, M.; Jiao, Y.; Bernhardt, P., V.; Zhang, M.; Wang, Q.; Du, A.; Wang, H.; Liu, G.; Wang, L, *Nano Research*, DOI: 10.1007/s12274-015-0948-y.

35 Öz, S.; Hebig, J., C.; Jung, E.; Singh, T.; Lepcha, A.; Olthof, S.; Flohre, J.; Gao, Y.; German, R.; van Loosdrecht, P., H., M.; Meerholz, K.; Kirchartz, T.; Mathur, S., *Sol. Energ. Mater. Sci.* DOI: 10.1016/j.solmat.2016.01.035.

36 Eckhardt, K.; Bon, V.; Getzschmann, J.; Grothe, J.; Wisser, F.; Kaske, S., *Chem. Commun.* **2016**, 52, 3058-3060.

37 Miyasaka, T.; Ikegami, M.; Kijitori, Y., *J. of Electrochem. Soc.*, **2007**, *154,* A455.

38 Kogo, A.; Sanehira, Y.; Ikegami, M.; Miyasaka, T., *J. Mater. Chem. A*, **2015**, *3*, 20952-20957.

39 Kogo, A.; Sanehira, Y.; Ikegami, M.; Miyasaka, T., *Chem. Lett*, **2016,** 45, 143-145.

40 Stoumpos, C., C.; Malliakas, C., D.; Kanatzidis, M., G., *Inorg. Chem.*, **2013**, *52*, 9019-9038.

Chapter 4

Studying the Effect of Tuned Morphology of Methylammonium Iodobismuthate ($(CH_3NH_3)_3Bi_2I_9$) on the Photovoltaic Device Performance.

Abstract

Non-toxic and high stable methylammonium iodobismuthate (MBI) ($(CH_3NH_3)_3Bi_2I_9$) as a solution processable photovoltaic absorber produces hexagonal non-uniform morphology leading to poor interfacial contacts with the electron and hole transporting layers. Herein, MBI morphology is tuned by bringing in a small amount of *N*-methyl-2-pyrrolidone (NMP) as a morphology controller into the MBI-DMF solution. The incorporation of different concentration of NMP into the precursor solution was found to control the rate of crystallization. An optimal low concentration of 2.5% NMP added to the MBI-DMF precursor solution showed 50% enhancement in short-circuit current (J_{sc}). The device showed power conversion efficiency (PCE) up to 0.31% with high reproducibility. Moreover the devices were quite stable when exposed to an ambient atmosphere (relative humidity of ~50-60%) for 30 days.

4.1 Introduction

Ever since our pioneering work on perovskite solar cell in liquid junction that achieved 3.8% power conversion efficiency (PCE)[1] the perovskite photovoltaic research has gained enormous attention worldwide[2,3] with a certified efficiency scaled up to 22.1% in just 8 years.[4] Such high efficiency in these devices is attributed to long diffusion length[5] and high mobility of charge carriers.[6] Simple solution processes adopted for perovskite preparation offer wider choice to control various parameters to engineer the devices.[7] However, the toxicity of lead (Pb) and device instability stand as major obstacles for industrialization of this rising material. To improve the stability various attempts such as replacing methylammonium iodide (MAI) with formamidinium iodide (FAI),[8] using insulating $Al2O_3$ instead of UV-sensitive TiO_2, [9] developing new hole transporting material (HTM), [10] interfacial engineering[11] and developing 2D based perovskites[12] have been made. While some work on Pb based perovskite has shown promising results, replacement of toxic Pb with other non-toxic metals still remains a big challenge. Although tin (Sn) based perovskite cells have been reported to show PCE up to 10% the problem associated with it is the instability of Sn (II), which gets readily oxidized to Sn (IV) when exposed to air. [13, 14] Moreover, commercialization of Sn(II) based perovskite can be acutely more toxic than lead (II) because the oxidation of Sn(II) to Sn(IV) can cause reaction with the organism, releasing HI as byproduct, leading to serious damage.[15] Recently copper (Cu) has also been used to replace lead in perovskite structure ($(CH_3NH_3)_2CuCl_xBr_{4-x}$). But, its low absorption coefficient and heavy mass of holes limit the device efficiency to low value (0.02%).[16]

Bismuth (Bi) is the only non-toxic 6p-block element having outer lone pair of $6s^2$ electron same as lead (Pb).[17] Recently researchers have reported promising optoelectronic and photovoltaic properties of methylammonium iodobismuthate (MBI) ($(CH_3NH_3)_3Bi_2I_9$) achieving 0.1% efficiency, both in normal and inverted structure, with long term stability. [17, 18, 19] Previous chapter demonstrated the effect of under layer on the growth of bismuth perovskite and the results suggested that bismuth perovskite growth on anatase TiO_2 mesoporous under layer, compared to brookite mesoporous and compact TiO_2 (planar architecture) under layer, facilitates better interfacial contacts of MBI with their adjacent

connecting layers. As a result, an efficiency of ~0.2% was achieved with TiO_2 anatase porous layer. [20] In various literatures, MBI perovskite processed by solution methods formed hexagonal flakes of MBI, leading to non-uniform dendrite morphology on porous TiO_2.[17-20] The key challenge encountered in one-step MBI perovskite spin-coating process is to control rapid crystallization of MBI perovskite which lead to non-homogeneous MBI flakes. This is readily evidenced for MBI by the spontaneous formation of an orange perovskite layer, after spin coating process; where as in case of lead perovskite complete crystallization of $CH_3NH_3PbI_3$ is much slower and is achieved on thermal treatment. The difference indicates faster reaction of BiI_3, in comparison to PbI_2 or $PbCl_2$, with MAI (CH_3NH_3I) to form perovskite. As a result, rough surface of MBI perovskite with many pinholes leads to poor device performance. Therefore, tuning the morphology is essential to improve the device performance of MBI perovskite.[18-20] Recently, Hoye et al. showed uniform morphology and superior carrier transport property in vapour-processed MBI film although its photovoltaic performance was not clarified.[21] However, it is of critical importance to develop low cost and rapid solution process in order to obtain smooth and uniform layer of MBI perovskite.

4.2 Experimental

4.2.1 Synthesis of CH_3NH_3I

50 g of hydroiodic acid (57 wt.% in water, Wako) was added dropwise to 50 mL methylamine (40% in ethanol, Wako) with gentle stirring in an ice bath. After stirring for 2 hours, a white precipitate was recovered through evaporation using rotor-vapour at 50 ^{O}C for 1 hour. Subsequently, the product was recrystallized using ethanol and diethyl ether sequentially in a -7 ^{O}C condition. The precipitate was recovered again through evaporation at 50 ^{O}C for 1 hour. The final product, CH_3NH_3I, was acquired by washing with diethyl ether and then drying at 45 ^{O}C in a vacuum oven overnight.

4.2.2 MBI perovskite device fabrication

Transparent conductive FTO glass was cleaned by solvent washing and UV-ozone treatment. TiO_2 compact layer (CL) was deposited by repeated spin coating of titanium diisopropoxide bis (acetylacetonate) solution in 2-propanol followed by sintering at 550 ^{O}C for 30 min. After cooling down the substrates were given 80 mM $TiCl_4$ treatment at 70 ^{O}C

for 40 min and were annealed again at 550 ^{O}C for 30 min. Mesoporous layer was deposited by dissolving the commercial available TiO_2 paste (18-NRT) in ethanol (1:4 wt. ratio) and spin coating the solution at 3000 rpm for 30 sec. After depositing the mesoporous layer, the substrates were annealed at 500 ^{O}C for 1 hr. MBI layer was achieved by spin coating the DMF solution, containing 20 wt.% bismuth iodide (BiI_3) and methylammonium iodide (MAI) (169 mg BiI_3 and 69 mg MAI in 1 ml DMF), at 1500 rpm for 30 sec followed by annealing at 110 ^{O}C for 90 min. The HTM solution was prepared by dissolving 84 mg of 2 2' 7 7'-tetrakis-(n n-di-4-methoxyphenyl amino)-9 9'-spirobifluorene (spiro-OMeTAD) (Merck), 14 µL of 4-tertbutylpyridine (TBP, Aldrich), 27 µL of a stock solution of 170 mg/mL of lithium bis(trifluoromethylsulfonyl) imide in acetonitrile in 1 mL of chlorobenzene. The prepared solution was spin coated on MBI deposited substrates at 3000 rpm for 30 sec. and the cells were left overnight in dark for air oxidation. Finally, thermal evaporation of gold was performed at 5×10^{-4} pa pressure to complete the cell. To introduce NMP treatment in the device fabrication, different concentration of NMP (12.5 µL, 25 µL, 50 µL) was added to 1 ml MBI-DMF solution and after stirring for 1 hour the solution was skinned by procedure mentioned above.

4.2.3 Characterization

The structural, morphological and optical analysis were carried out using X-ray diffractometer (D8 Discover, Brucker) with CuKα radiation source, scanning electron microscope (SU8000, HITACHI) and UV-Vis spectrophotometer (UV-Vis 1800, Shimadzu) respectively. The current density-voltage (J-V) curves were characterized using a Peccell Technologies PEC-L01 solar simulator featuring a computer-controlled digital source meter Keithley 2400 source meter under 1 sun illumination (AM 1.5 G, 100 mW/cm^2), calibrated using a monocrystalline silicon photodiode (KG3, Oriel, USA) During the measurement, a mask featuring a 0.088 cm^2 aperture area was attached to the incident side of all devices. All the devices were measured using both a forward scan (short-circuit to open-circuit) and a backward scan (open-circuit to short-circuit) with a fixed 10 mV step voltage and 50-ms delay time. The active cell area was of 0.088 cm^2.

4.3 Results and discussion

4.3.1 MBI perovskite film characterization

In this study, morphological evolution of MBI perovskite via NMP incorporation into MBI-DMF solution and its effect on device performance is investigated. NMP which forms complex with lead perovskite has been employed earlier to tune the morphology and obtain highly reproducible device performance in lead based perovskites.[22,23] According to previous reports, NMP forms complex with bismuth iodide[24] and from the UV-vis absorption spectra of MBI dissolved in pure NMP, the absorption band at ~360 nm can be seen (Fig. 4.1a) and is different from the absorption spectra of MBI film (Fig. 4.1b) which evidently signifies the formation of some complex similar to that of $MAPbI_3$-NMP and/or $Bi(dppn)I_3$-NMP.[24] Addition of NMP slowed down the evaporation of solvent mixture during the spin-coating process because of high boiling point and low vapour pressure and facilitated slow crystallization with uniform film formation of MBI perovskite.

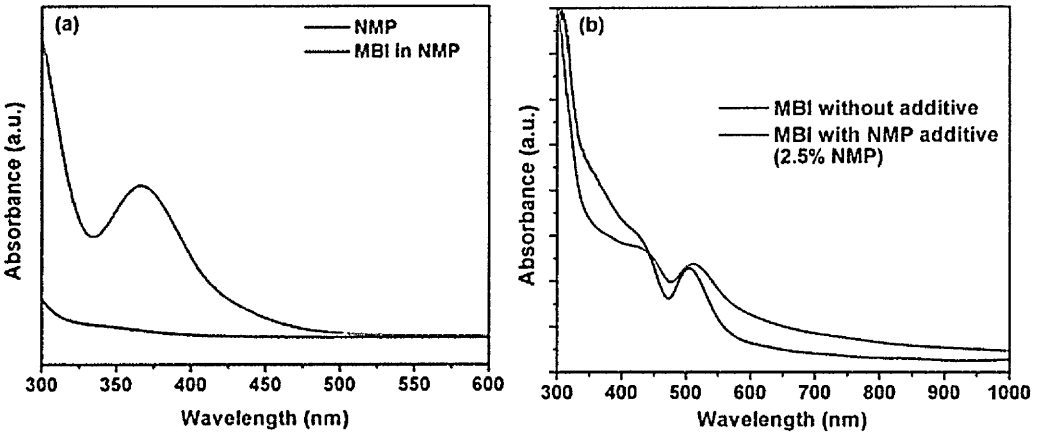

Figure 4.1: UV-vis spectra of (a) MBI dissolved in NMP and (b) MBI perovskite film without and with NMP (2.5%) additive.

In the samples made from solution without NMP, no change in colour of the perovskite layer before and after heating at 110 ^{O}C for 90 min is observed due to fast crystallization. In contrast, colour of NMP treated (all concentrations) MBI layer changed from transparent to orange during the heating process at the same temperature. The transparent colour of the coated film (before heating) of NMP-DMF MBI might be an

intermediate solvated phase formed during perovskite deposition process, similar to lead based perovskite forming complexes with DMSO and NMP.[23] This intermediate assisted crystallization is expected to change the morphology of final film which has been evidently observed in scanning electron micrographs (SEM) images. From Fig. 4.2, it is evident that the MBI perovskite without additive has grown into hexagonal flake structure (non-uniform morphology) exposing large area of porous TiO_2 through large number of micro-pores (Fig. 4.2a), which is in good agreement with previous reports.[17, 18, 20] In case of NMP guided MBI perovskite (Fig. 4.2 b, c, d) the change in the morphology has been observed with increasing the concentration of NMP additives. In lower concentration of NMP (1.25%), MBI perovskite grows into large crystals (Fig. 4.2b) however this morphology has not observed uniformly over the substrate as shown in Fig. 4.3a. This indicates that the amount of NMP additive is not sufficiently enough to tune the morphology effectively. Further increasing the concentration of NMP (2.5%), the morphology changed drastically (Fig. 4.2c) as the grain growth is different in comparison to previous two cases (non-NMP and lower concentration of NMP); the perovskite covered the mesoporous TiO_2 layer uniformly. The grain size increased with further increase in the concentration of NMP additive (5%) as shown in Fig. 4.2d. The change in the grain growth with NMP concentration is attributed to the change in solubility/interaction of the precursor material with the solvent molecules as evident from UV-vis spectra (Fig. 4.1a). It has been observed that the colour of the precursor solution (without additive) changes from transparent red to intense red colour with the addition of NMP. Further the rate of evaporation of NMP is slower than the DMF which causes the change in the morphology of MBI films.

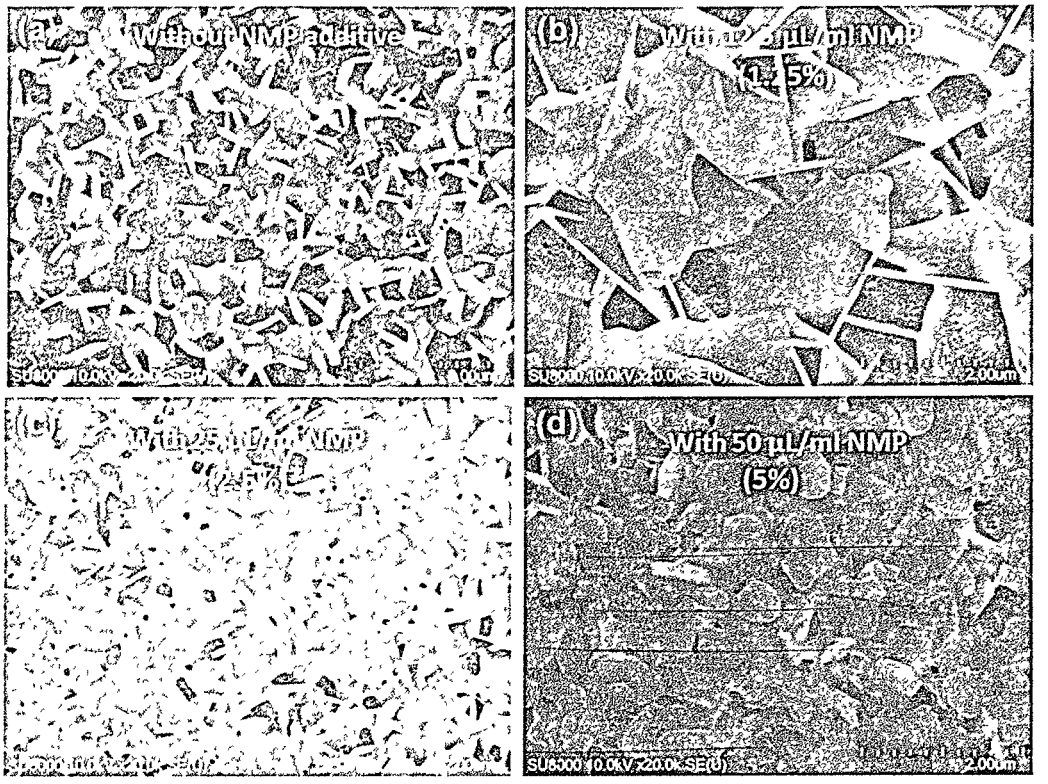

Figure 4.2: Top surface SEM image of MBI perovskite (a) without and (b, c, d) with different concentrations of NMP additive.

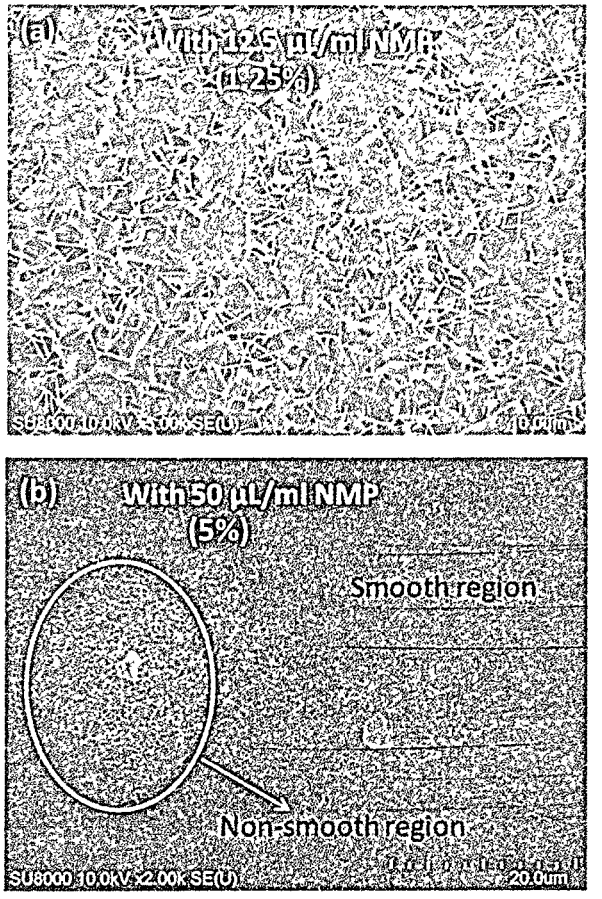

Figure 4.3: Low mag top surface SEM image of (a) 1.25% and (b) 5% NMP additive based MBI films.

The XRD pattern of MBI films, deposited on mesoporous TiO_2 under layer, under different processing conditions are shown in Fig. 4.4. From the diffraction pattern of non-additive based MBI films a doublet peak at 2 theta = ~12^O is seen which is assigned to MBI perovskite[19, 20, 25] and its intensity increases with the addition of higher concentration of NMP as shown in zoomed inset figure. Additionally, intensity of small peak at 2 theta = ~24^O also increases with the addition of NMP indicating slight change in the orientation of MBI crystals. This result is in consistent with observed changes in the morphology as evident from SEM images (Fig. 4.2). From this it is significantly evident that NMP-free MBI films showed poor crystallinity on mesoporous TiO_2 layer and with the addition of NMP its crystallinity improved which is suspected due to proper interaction/dissolution of precursor material with the addition of NMP, into the main solvent DMF. The optical absorption spectra showed absorption band around ~500 nm for both NMP treated and non-treated

films, however, a slight increase in absorption is observed for NMP treated (2.5%) MBI films probably due to the uniform and dense film formation (Fig. 4.1b)

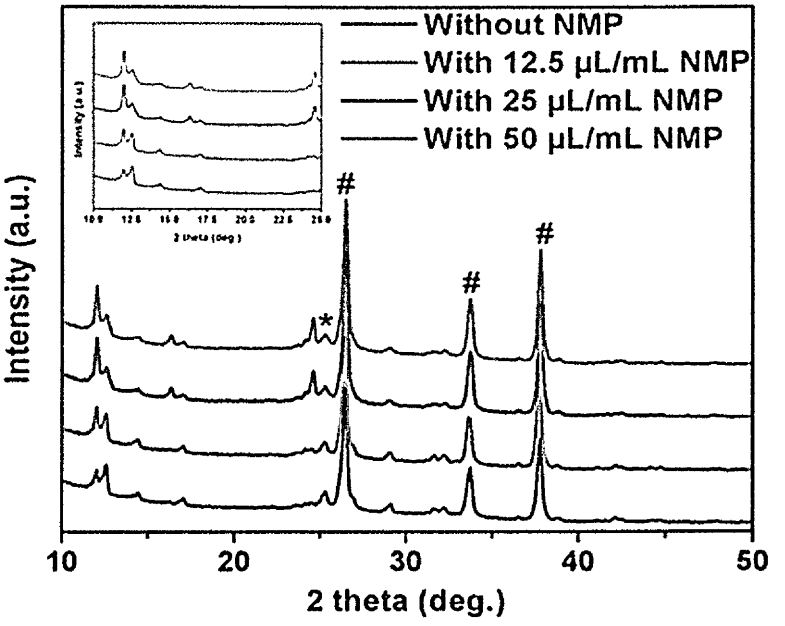

Figure 4.4: XRD diffraction pattern of MBI layer without and with different concentration of NMP additive on mesoporous TiO_2 coated FTO substrates (# corresponds to FTO peaks and * corresponds to TiO_2 peaks).

4.3.2 MBI perovskite device performance and long term stability test

To verify the influence of tuned morphology and improved crystallization, devices were fabricated by spin coating with MBI solution (without and with additives) on mesoporous TiO_2 coated substrates and were compared. Fig. 4.5a compares the average current density-voltage (J-V) characteristics (Table 1) and external quantum efficiency (EQE) spectra (Fig. 4.5b) of best performing devices, measured under simulated sunlight intensity of AM1.5 (100 mW/cm2). In all cases studied device showed small hysteresis in J-V characteristic curve which can be due to unbalanced electron and hole flux at the interface of electron- and hole transporting layers[26] originating from the energy level mismatch between MBI and its neighboring charge transporting layers.[17, 20] As can be seen from the histogram plot (Fig. 4.5c) short circuit photocurrent density (J_{sc}) of the NMP-free device varied from 0.58 mA/cm^2 to 0.68 mA/cm^2 with majority of samples showing J_{sc} of 0.62

mA/cm^2. With the addition of 1.25% NMP there has been a slight increment in J_{sc} ranging from 0.6 mA/cm^2 to 0.74 mA/cm^2. In contrast, addition of 2.5% of NMP drastically improved J_{sc} to a range from 0.88 mA/cm^2 to 1 mA/cm^2. Based on the fact of crystallinity and morphology improvement, this increment in J_{sc} is attributed to better coverage and crystallinity of MBI layer formed on TiO_2 scaffold. With further increasing the NMP concentration to 5.0% the J_{sc} decreased probably due to the non-smooth region of MBI perovskite layer over the substrate as evidenced in SEM image (Fig. 4.3b). The EQE spectra (Fig. 4.5b) of pristine and additive based MBI perovskite have same EQE edge up to 650 nm which indicated similar spectral response, however, the EQE increased in visible region for 2.5% NMP-based MBI perovskite. From PCE histogram plot (Fig. 4.5d), non-additive based MBI perovskite device showed PCE ranging from 0.13% to 0.2% and the PCE of device with 12.5 mL and 50 mL of NMP in 1 mL precursor solution also showed PCE in the same range. Interestingly, device containing MBI perovskite treated with 25 mL of NMP showed PCE ranging from 0.28% to 0.31% with majority of samples showing 0.3% PCE.

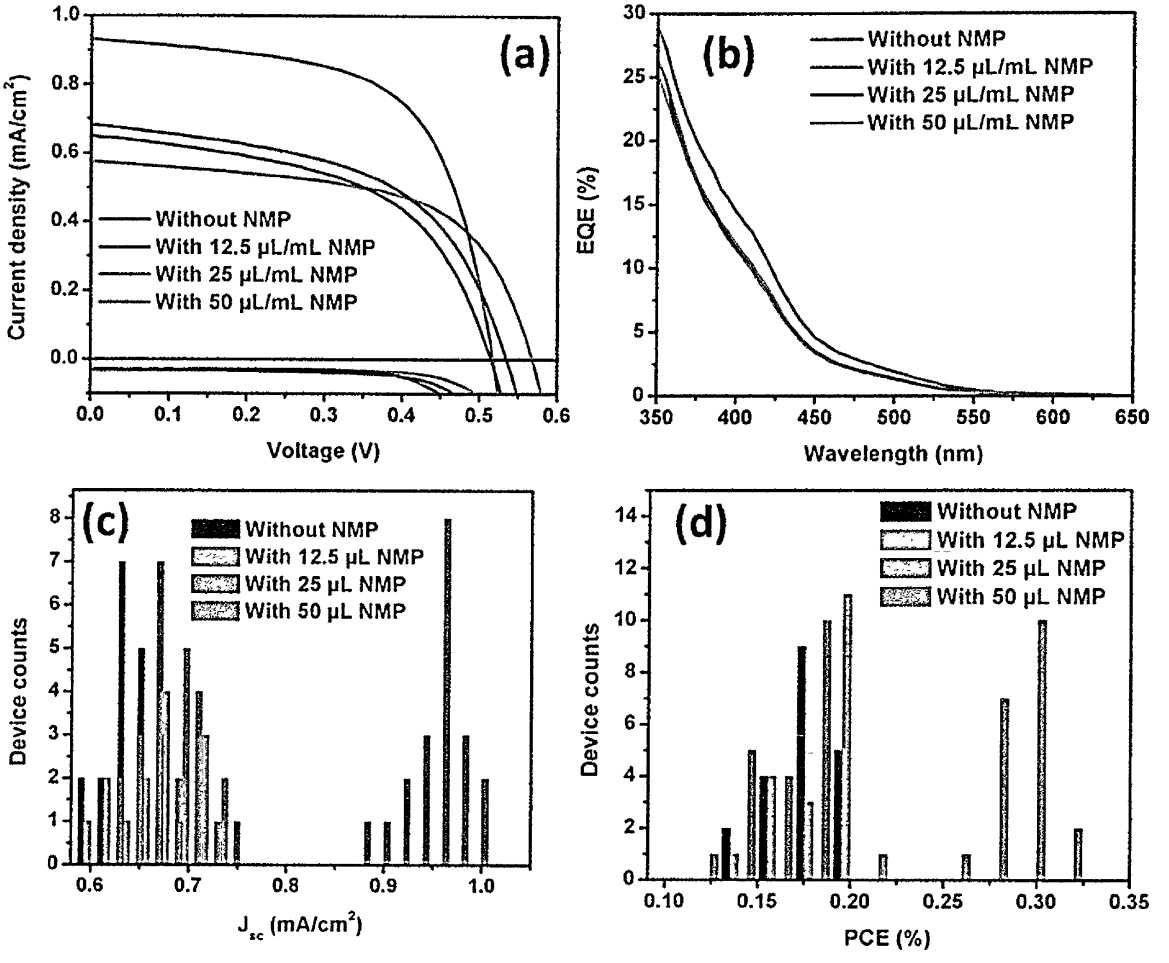

Figure 4.5: (a) Average J-V curves, (b) IPCE Spectra, (c) J_{sc} and (d) PCE histogram plot of devices containing MBI perovskite without and with different concentration of NMP additives.

Table 4.1: Device parameters of best performing cells with and without additives.

Case studied	J_{sc} (mA/cm^2)	V_{oc} (V)	FF	PCE (%)
Without additive	0.68	0.53	0.53	0.19
With 12.5 µL NMP	0.7	0.51	0.51	0.18
With 25 µL NMP	0.94	0.51	0.61	0.31
With 50 µL NMP	0.65	0.51	0.52	0.18

Long term stability of MBI based devices are investigated by exposing (without encapsulation) to relative 50–60% humidity for 30 days. Device PCE are quite stable (Fig. 4.6) and NMP treated samples showed improved stability (88% sustained) compared to pristine (66% sustained) which is attributed to high crystallinity of MBI crystals as evidenced from XRD measurement as well as high stable oxidation state of bismuth.[17-21]

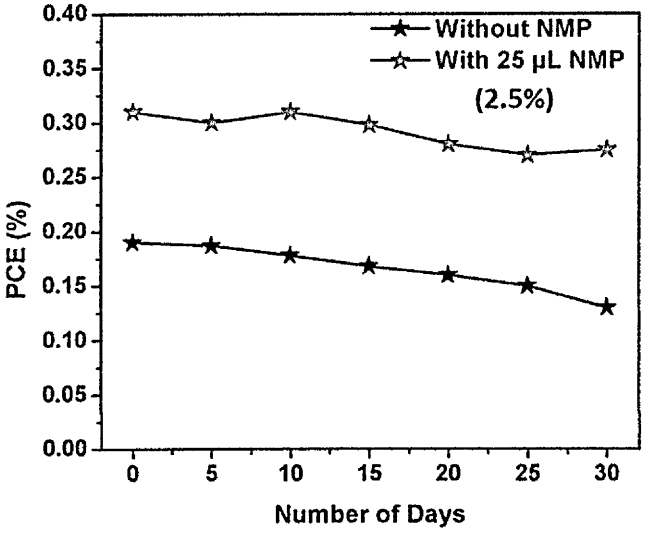

Figure 4.6: Long term stability of non-encapsulated MBI devices (without and with NMP additives) exposed to ~50-60% humidity atmosphere.

A solvent engineering process was developed to prepare uniform MBI absorber for fabrication of non-toxic, high stable perovskite solar cells. However, device performance is highly behind those of lead perovskite solar cells. Even though MBI perovskite absorbs up to ~650 nm it encompasses high carrier density of around ~10^{16} cm^{-3}, which are 7 orders of magnitude higher than lead perovskite.[17] Presence of such high density of background charge carriers are mainly responsible for such low J_{sc} and performance, resulting from bulk recombination within the MBI perovskite, also leading to lower V_{oc}. Hao et al. demonstrated that by tuning and controlling the morphology of tin based perovskite, its background carrier densities can be reduced.[27] Although in case of MBI perovskite, prior reports suggests that tuning the morphology can help to reduce the background carrier density,[18] the present study reveals that these background charge carriers are slightly reduced to some extent with the addition of NMP, further indicating that the background charge carrier densities are not highly affected by tuning the morphology unlike tin perovskite. The slight reduction in background charge carriers, with the addition of NMP, can be due to the tuned morphology and orientation of MBI perovskite film. This further directs towards addition of additives and dopants which can reduce the background charge carrier densities similar to the addition of SnF_2 in tin based perovskite.[14] In addition to intrinsic property of MBI, the device performance also depends on the charge collecting materials surrounding the MBI in aspects of interfacial contacts and energy level matching. Non-additive MBI samples showed poor crystallinity on TiO_2 mesoporous layer suggesting choice of suitable electron transporting layer and hole transporting layer due to the energy level mismatch between MBI and Spiro-OMeTAD leading to lower V_{oc}.

4.4 Conclusion

Addition of different concentration of NMP into the precursor solution of MBI perovskite facilitated slow and uniform crystallization resulting in improved morphology and crystallinity. The improved morphology of MBI perovskite at particular concentration of 2.5% NMP resulted in enhancement in J_{sc} and its concomitant enhancement in PCE to 0.31%. Additionally, the devices with NMP treated MBI perovskite are highly stable up to 30 days with exposure to relative ~50-60% humidity atmosphere. The present study opened up the possibilities of tuning the morphology and stability of MBI perovskite. It also directs

research towards minimization of the background carrier density by tuning the intrinsic optoelectronic properties and selection of suitable charge collecting materials for further enhancement of efficiency of MBI perovskite solar cells.

4.5 References

1. A. Kojima, K. Teshima, Y. Shirai and T. Miyasaka, *J. Am. Chem. Soc.*, **2009**, *131*, 6050.

2. T. Miyasaka, *Chem. Lett.*, **2015**, *44*, 720.

3. T. Singh, J. Singh and T. Miyasaka, *ChemSusChem*, **2016**, *9*, 2559.

4 Best solar cell efficiency chart. Available at http://www.nrel.gov/ncpv/images/efficiency_chart.jpg accessed on (2nd Dec. 2017).

5. S. D. Stranks, G. E. Eperon, G. Grancini, C. Menelaou, M. J. P Alcocer, T. Leijtens, L. M. Herz, A. Petrozza and H. J. Snaith, *Science*, **2013**, *342*, 341.

6. G. C. Xing, N. Mathews, S. Y. Sun, S.S. Lim, Y. M. Lam, M. Grätzel, S. Mhaisalkar and T.C. Sum, *Science*, **2013**, *342*, 344.

7. S. Y Sun, T.Salim, N. Mathews, M. Duchamp, C. Boothroyd, G. C. Xing, T. C. Sum and Y. M. Lam, *Energ. Environ. Sci*, **2014**, *7*, 399.

8. N. J. Jeon, J. H. Noh,; W. S. Yang, Y. C. Kim, S. Ryu, J. Seo and S. I. Seok, *Nature*, **2015**, *517*, 476.

9. M. L. Lee, J. Teuscher, T. Miyasaka, T. N. Murakami and H. J. Snaith, *Science*, **2012**, *338*, 643.

10. P. Ganesan, K. Fu, P. Gao, I. Raabe, K. Schenk, R. Scopelliti, J. Luo, L. H. Hong, M. Grätzel and M. K. Nazeeruddin, *Energy Environ. Sci.*, **2015**, *8*, 1986.

11. A. Kulkarni, A. Jena, H-W. Chen, Y. Sanehira, M. Ikegami and T. Miyasaka, *Solar Energy*, **2016**, *136*, 379.

12. D. H Cao, C. C. Stoumpos, O.K. Farha, J. T. Hupp and M. G. Kanatzidis, *J. Am. Chem. Soc.*, **2015**, *137 (24)*, 7843.

13. F. Hao, C. C. Stoumpos, D. H. Cao, R. P. H. Chang and M. G. Kanatzidis, *Nature Photonics,* **2014**, *8*, 489.

14. M. H. Kumar, S. Dharani, W. L. Leong, P.P. Boix, R. R. Prabhakar, T. Baikie, C. Shi, H. Ding, R. Ramesh, M. Asta, M. Graetzel, S. G. Mhaisalkar and N. Mathews, *Adv. Mater.*, **2014**, *26 (41)*, 7122.

15. A. Babayigit, A. Ethirajan, M. Muller and B. T. Conings, *Nature Materials*, **2016**, *15*, 247.

16. D.Cortecchia, H. Dewi, J. Yin, A. Bruno, S. Chen, T. Baikie, P. Boix, M. Graetzel, S. Mhaisalkar, C. Soci and N. Mathews, *Inorg. Chem.*, **2016**, *55*, 1044.

17. M. Lyu, J-H. Yun, M. Cai, Y. Jiao, P. V. Bernhardt, M. Zhang, Q. Wang, A. Du, H. Wang, G. Liu and L. Wang, *Nano Res.*, DOI: 10.1007/s12274-015-0948-y.

18. B.-W. Park, B. Philippe, X. Zhang, H. Ransmo, G. Boschloo and E. M. J. Johansson, *Adv. Mater.*, **2015**, *27*, 6806.

19. S. Öz, J. C. Hebig, F. E. Jung, T. Singh, A. Lepcha, S. Olthof, J. Flohre, Y. Gao, R. German, P. H. M. van Loosdrecht, K. Meerholz, T. Kirchartz and S. Mathur, *Sol. Energ. Mater. Sci.*, **2016**, *158*, 195.

20. T. Singh, A. Kulkarni, M. Ikegami and T. Miyasaka, *ACS Appl. Inter. Mater.*, **2016**, *8 (23)*, 14542.

21. R. L. Z. Hoye, R. E. Barndt, A. Osherov, V. Stevanović, S. D. Stranks, M. W. B. Wilson, H. Kim, A.J. Akey, J. D. Perkins, R. C. Kurchin, J. R. Poindexter, E. N. Wang, M. G. Bawendi, V. Bulović and T. Buonassisi, *Chemistry-A Eur. Journal*, **2016**, *22*, 2605.

22. Y.-J. Jeon, S. Lee, R. Kang, J-E. Kim, J-S. Yeo, S-H. Lee, S-S. Kim, J-M. Yun, and D-Y. Kim, *Scientific Reports*, **2014**, *4*, 6945.

23. Y. Jo, K. S. Oh, M. Kim, K-H. Kim, H. Lee, C-W. Lee and D. S. Kim, *Adv. Mater. Inter.*, **2016**, *3*, 1500768.

24. W. Travis, C. E. Knapp, C. N. Savory, A. L. Ganose, P. Kafourou, X. Song, Z. Sharif, J. M. Cockcroft, D. O. Scanlon, H. Bronstein, and R. G. Palgrave, *Inorg. Chem.*, **2016**, *55*, 3393.

25. K. Eckhardt, V. Bon, J. Getzschmann, J. Grothe, F. M. Wisser and S. Kaskel, *Chem. Commun.*, **2016**, *52*, 3058.

26. J. H. Heo, H. J. Han, D. Kim, T. K. Ahn and S. H. Im, *Energy Environ. Sci.*, **2015**, *8*, 1602.

27. F. Hao, C. S. Stoumpos, P. Guo, N. Zhou, T. J. Marks, R. H. P. Chang and M. G. Kanatzidis, *J. Am. Chem. Soc.*, **2015**, *137*, 11445.

Chapter 5

Vapour Annealing Controlled Crystal Growth and Photovoltaic Performance of Bismuth Triiodide Embedded in Mesostructured Configurations

Abstract

Low stability of organic-inorganic lead halide perovskite and toxicity of lead (Pb) quest for alternative non-toxic and stable light absorbing materials with promising optoelectronic properties. Herein, we report about non-toxic bismuth triiodide (BiI_3) photovoltaic device prepared using TiO_2 mesoporous film and spiro-OMeTAD as electron and hole transporting materials, respectively. Effect of annealing methods (e.g. thermal annealing-TA, solvent vapour annealing-SVA, pot-roast vapour annealing-PR-VA) and different annealing temperatures (90, 120, 150 and 180 ^{O}C for PR-VA) on BiI_3 film morphology have been investigated. As found in the study, grain size increased and film uniformity improved with temperature raised from 90 to 150 ^{O}C. The photovoltaic devices based on BiI_3 films processed at 150 ^{O}C with PR-VA treatment showed power conversion efficiency (PCE) of 0.5% with high reproducibility, which is to date the best PCE of a BiI_3 photovoltaic device employing organic HTM, owing to increase in grain size and uniform morphology of BiI_3 film. These devices showed stable performance even after 30 days of exposing to 50% relative humidity. More importantly, the study reveals many challenges and rooms (discussed in the details) for further development of the BiI_3 photovoltaic devices.

5.1 Introduction

Perovskite solar cells (PSCs) have witnessed an unprecedented rise in power conversion efficiency (PCE) from 3.8% to certified 22.1% in just 8 years as compared to already existing technologies, owing to its exceptional optoelectronic properties and ease of solution processing protocols.[1] While ongoing worldwide research work on the lead perovskite photovoltaic device and its PCE is rapidly approaching the theoretical efficiency limit of the single junction solar cell, it faces poor long-term stability issue.[2] Exposure to moisture, oxygen, heat stress, UV-light and its intrinsic chemical instability, causes degradation of perovskite device leading to exposure of PbI_2.[2] Thermal and chemical instability issues have been addressed and resolved by developing perovskite materials via compositional and solvent engineering and triple- and multi-cation system.[3] Additionally, an electron transporting material (ETM)/perovskite, perovskite/ hole transporting material (HTM), HTM/counter electrode interfacial modifications has also improved stability against moisture and UV-light[4] up to few months, however long-term stability to several tens of years still remains a big challenge. On the other hand, it has been reported that exposure of PbI_2 after degradation of perovskite is highly toxic to human reproductive and nervous systems.[5] Hence to address the Pb toxicity issue, tin (Sn),[6] germanium (Ge),[7] bismuth (Bi),[8, 9] antimony (Sb)[10] based perovskite materials have been explored as alternate non-toxic materials. However, Sn and Ge perovskites suffer from structural instabilities due to spontaneous oxidation when exposed to ambient atmosphere[11] and very recently toxicity concern of Sn-perovskite has been raised.[5] Considering Bi based perovskites, the efficiency of $(CH_3NH_3)_3Bi_2I_9$, $Cs_3Bi_2I_9$ photovoltaic devices have not shown impressive rise due to relatively high band gap (~2eV), poor surface morphology, high intrinsic carrier densities and high exciton binding energies and even after several attempts by various groups the device performance still remains below 2%.[8, 9,12,13,14,15] Previous chapter studies reveal that tuning the morphology of $(CH_3NH_3)_3Bi_2I_9$ does not essentially improve the performance much.[9] Also, Sb-based perovskites have shown comparable progress as of Bi perovskites and the conversion efficiency still lags behind of lead perovskites.[10] Moreover, combining trivalent metal halide (Bi^{3+}, Sb^{3+}) with a monovalent metal halide (Ag^{+}, Cu^{+}) to form double

perovskites (having a 3D structure) have also been demonstrated showing promising carrier lifetime.[16] However, very recently Savory et al. reported its limitations including high effective masses, large indirect band gap, to name few and suggested to expand the search beyond Ag-Bi double perovskites.[17] Hence, finding an alternate eco-friendly material with lower band gap and promising optical properties suitable for the efficient photovoltaic system is critically important.

Noteworthy, to synthesize bismuth perovskite material BiI_3 is used as one of the precursor component[8, 9] which interestingly belongs to a layered heavy metal semiconductors group and possesses interesting optical properties[18] such as high optical absorption ($>10^5$ cm^{-1}) than Si and GaAs,[19] electron diffusion length of 4.9 μm, large static dielectric constant etc.[18] Also, BiI_3 has an outer shell electronic configuration of $6s^2$ which leads to disperse valance band, high dielectric constant, shallow intrinsic point defects, all of which are serviceable properties of defect tolerant material.[18] Having a rhombohedral crystal structure, BiI_3 forms layered 2D structure with hexagonal closely packed iodine atoms and 2/3 of octahedral sites are occupied by bismuth atoms.[20] BiI_3 has been previously investigated intensively in gamma-ray detectors[21] and X-Ray imaging.[22] Moreover, theoretically and experimentally efforts have been made and predicted to use BiI_3 as a potential photovoltaic absorber through "inverse design search".[18,23] Brandt et al. observed room temperature photoluminescence (PL) of BiI_3 both in vapor and solution-processed thin film indicating its promising application in optoelectronic devices.[18] However, only a few attempts have been made to integrate BiI_3 into photovoltaic devices. The initial report demonstrated BiI_3 as a hole transporting material (HTM) in organic solar cells with fullerene-based light absorber as an active layer.[24] Recently, TiO_2 compact layer (CL) based planar structured BiI_3 solar cell has been reported by Lehner et al. and Hamdeh et al. with 0.3% and 1% efficiency respectively using poly-triarylamine (PTAA) as organic HTM[25] in former case and MoO_3 and V_2O_5 as inorganic HTM[26] in later one and in both the reports tetrahydrofuran (THF) was used as a main solvent to dissolve BiI_3 with hydroiodic acid as an additive.[25, 26] With few attempts it is clear that the potential of BiI_3 as light absorbing material in photovoltaic system and non-toxic alternative to lead perovskites has not been thoroughly investigated. Herein, BiI_3 is incorporated in TiO_2 meso-structured architecture by dissolving it in DMF followed by spin coating and annealing for 1 hour with various

annealing treatment such as solvent vapour annealing (SVA),[27] pot-roast vapour annealing (PR-VA)[28] and only thermal annealing (TA) (without SVA and PR-VA) treatment. For processing under ambient atmosphere, we choose DMF as the main solvent to dissolve BiI_3 as THF promptly absorbs water[29] and is not suitable for its use in ambient atmosphere. Spiro-OMeTAD and Au acting as HTL and counter electrode respectively were deposited to complete the cell.

5.2 Experimental

5.2.1 Device fabrication

F-doped SnO_2 (FTO) (10 Ω/□, NSG Group, Japan) conductive glass substrates were washed by ultrasonic treatment with commercial detergent (2% Hellmanex in water), deionized water (DI), acetone and 2-propanol for 15 minutes each. All the chemicals were used as received without any further purification. The substrates were given UV-ozone treatment for 10 min before coating TiO_2 compact layer.

TiO_2 compact layer coating: Solution of titanium diisopropoxide bis(acetylacetonate) (Ti acac) (75 wt% in isopropanol, Sigma-Aldrich) in ethanol (99.99%, Wako) was spray-coated on to cleaned FTO coated glass substrates at 500 ^{O}C to obtain 50 nm thick TiO_2 compact layer (CL) and allowed the substrates to remain at the same temperature for 30 min followed by cooling down naturally to room temperature.

TiO_2 Mesoporous layer coating: Anatase TiO_2 mesoporous layer was spin coated using a commercially available TiO_2 paste (18NR-T, Dyesol, particle size ~20 nm) diluted in 25 wt% ethanol at 3000 rpm/30 sec followed by sintering at 500 ^{O}C for 1 hour in a muffle furnace. After cooling down the meso-structured substrates were given 40 mM $TiCl_4$ treatment at 70 ^{O}C for 30 min. The substrates were rinsed and cleaned with distilled water and ethanol and were again sintered at 500 ^{O}C for 30 min. The coated substrates were given UV-ozone treatment for 10 min prior to the BiI_3 layer deposition.

Active layer and HTM deposition: 1 M bismuth triiodide (BiI_3) in DMF were stirred on a hot plate at 50 ^{O}C for 1 hour prior to the coating. The BiI_3 solution was spin coated on TiO_2 mesoporous coated substrates at 1500/30 sec. After spin coating, the substrates were

transferred on to the hot plates which were already set at 90 ^{O}C, 120 ^{O}C, 150 ^{O}C and 180 ^{O}C for 1 hour with 10 μL DMF solvent at the inner boundary wall of Petri dish for SVA treatment and without any solvent for PR-VA treatment. For thermal annealing treatment, the substrates were heated without any Petri dish cover for 1 hour. 8 wt % spiro-OMeTAD solution in chlorobenzene containing additives of lithium bis(trifluoromethanesulfonyl) imide and 4-*tert*-butylpyridine were spin coated on BiI_3 coated substrates at 3000 rpm/30 sec. The HTM coated substrates were kept overnight in the air for oxidation of spiro-OMeTAD followed by thermal deposition of Au metal electrode to complete the cell.

5.2.2 Characterization

Solar cell characteristics of all devices were measured using a Peccell Technologies PEC-L01 solar simulator with a Keithley 2400 source meter under 1 sun illumination (AM 1.5G, 100 mW/cm^2). The EQE spectra of the device were measured with Peccell Technologies, PEC-S20 action spectrum measurement setup. The optical, structural and morphological analysis was carried out using UV-vis spectrophotometer (UV-vis 1800, Shimadzu), X-ray diffractometer (D8 Discover, Bruker) with Cu Kα radiation source and scanning electron microscope (SU8000, HITACHI), respectively. The active areas of the cells were 0.09 cm^2.

5.3 Results and discussion

5.3.1 BiI_3 thin film characterization

In order to estimate the band gap we measured UV-vis absorption spectra (Figure 5.1 a) of the optimized BiI_3 film and from the Tauc plot (Figure 5.1 b) assuming an indirect band gap we obtained the E_g of ~1.81 eV which is in agreement with prior reports.[25, 26] Encouragingly the band gap value is quite suitable for top cell in two terminal tandem devices. Influenced with a recent report by Hamdeh et al. who demonstrated SVA treatment to improve the morphology of BiI_3 (dissolved in THF) in which DMF drops were poured within the boundary wall of Petri dish[26] initial attempts were made to perform and compare the effect of TA and SVA treatment on BiI_3 films. Top surface scanning electron micrograph (SEM) image of TA treatment processed BiI_3 films reveals that the average size of the grains

is apparently small and show largely sized pinholes (Fig. 5.2 b). Although the BiI_3 grain size increases with DMF SVA, it also resulted in a large number of pinholes (Fig. 5.2 c) and the increase in grain size indicates that DMF vapour facilitates migration and promotes BiI_3 grain growth. Moreover, lower magnification SEM image of TA and SVA processed film (Figure 5.2 e, f) reveals large variation in grain size with a high degree of non-uniformity (BiI_3 crystals accumulate forming a non-homogeneous layer) and large gaps throughout the film. It is well known that rapid evaporation of polymeric thin film solvent can make the growth kinetically constrained leading to small grain growth which can be the reason for the non-homogeneous layer in case of TA treatment.[30] Even though previously many reports have shown that SVA treatment improves the morphology and performance of lead halide perovskite[27] as well as bismuth halide based solar cells[26] recently Numata et al. reported poor reproducible perovskite formation and performance with SVA treatment[28] owing to non-uniform solvent vapour atmosphere and excess vapor concentration (during SVA treatment) which can be the reason for non-uniform grain distribution and enormous BiI_3 grain growth observed in our study as can be seen in Fig. 5.2 c, f. Also, change in the morphology in comparison to previous report[26] can be due to the use of a different solvent to dissolve BiI_3. On the contrary, improvement in morphology, crystal growth with better uniformity (Fig. 5.2 d, g) by PR-VA treatment is observed, that is, confining BiI_3 coated substrates in a Petri dish without additional solvent drops during the heating process and the pinholes obtained from PR-VA treatment are relatively less and is in contrast to BiI_3 layer with TA and SVA treatment (Figure 5.2 b, c, e, f). The merit of PR-VA treatment is that the solvent evaporated from BiI_3 film gets uniformly distributed (due to Petri dish cover) and in the presence of recycled solvent atmosphere the grain grows uniformly resulting in non-coalescence of BiI_3 grains (Figure 5.2 d, g) and is in line with observation made by Numata et al. in lead perovskite system.[28] Fig. 5.2 a depicts the schematic representation of BiI_3 film processed with TA, SVA and PR-VA treatment. In all the cases the colour of BiI_3 films transitioned from orange to grayish black, during the heating process, indicating the decomposition of BiI_3-DMF complex into BiI_3.[26] In case of SVA and PR-VA process slow decomposition is observed due to slow evaporation of solvent DMF. From the above studies, therefore, it can be inferred better uniformity, large grains of the BiI_3 layer with PR-VA treatment in sharp contrast to SVA and TA treatment and thus further studies were mainly

focused on BiI_3 film processed with PR-VA treatment and finally compared the photovoltaic performance with TA processed BiI_3 film.

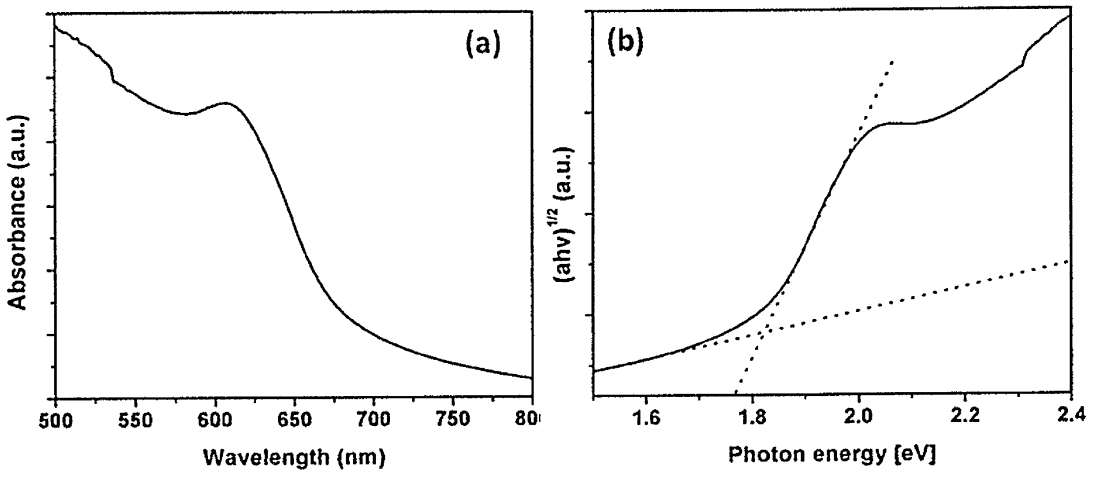

Figure 5.1: (a) UV-vis absorption spectra and (b) corresponding Tauc plot of the optimized BiI_3 thin film.

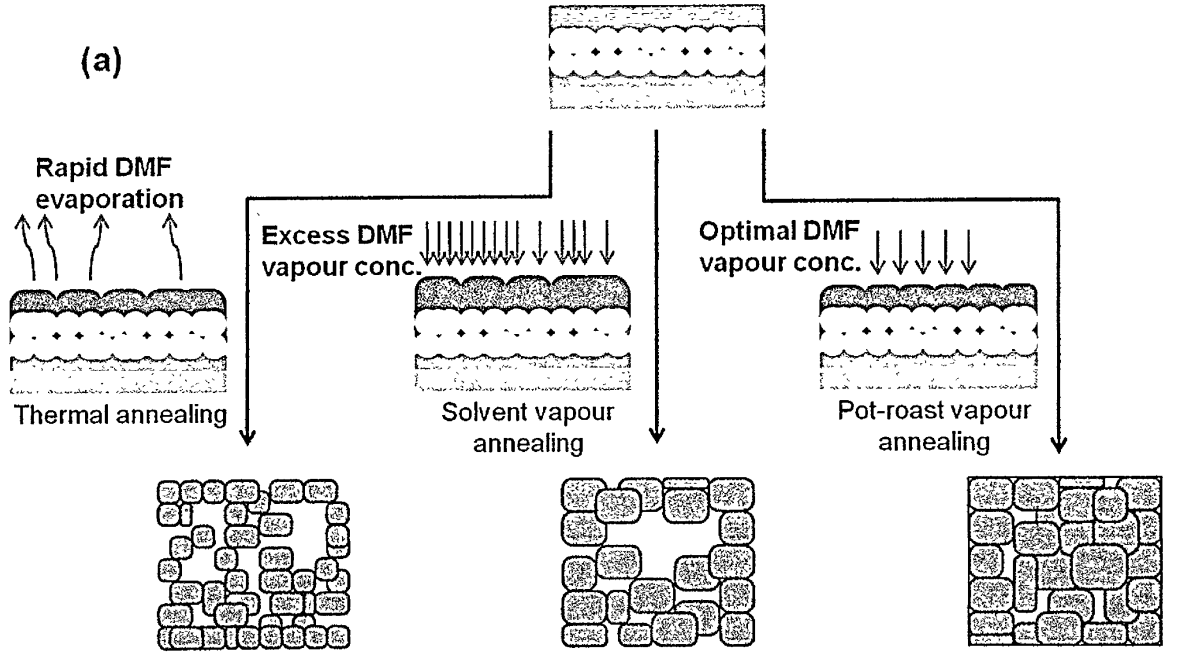

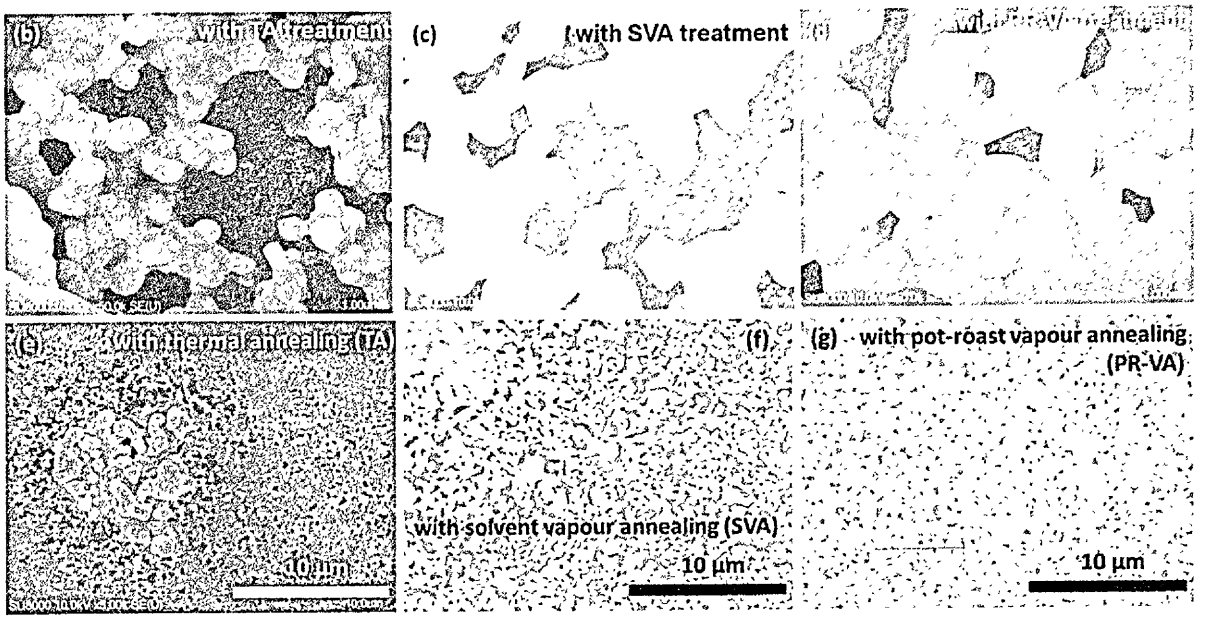

Figure 5.2: Schematic representation and top surface SEM image of BiI_3 films with (b, e) thermal annealing (TA), (c, f) solvent vapour annealing (SVA) and (d, g) pot-roast vapour annealing (PR-VA) treatment.

It is well known that pinholes containing layer causes a loss in photo-voltage and charge transport, most probably due to increased charge recombination. Hence, further optimization of the BiI_3 layer is needed in order to obtain pinhole-free layer. In above studies for TA, SVA and PR-VA treatment analysis the BiI_3 film was annealed at 150 ^{O}C which is very close to the boiling point of DMF (153 ^{O}C). This processing temperature can cause rapid evaporation of solvent resulting in pinholes, as observed lately. To address this issue, the films were annealed at various temperatures by transferring BiI_3 coated substrates (after spin coating) onto hot plates which were already set at 90 ^{O}C, 120 ^{O}C, 150 ^{O}C and 180 ^{O}C and Petri dish was covered for PR-VA treatment due to its observed beneficial effect, as mentioned above. Figure 5.3 shows the top surface and cross-section SEM image of BiI_3 films investigated. Interestingly, with the change in temperature, we observe variation in the morphology of BiI_3. When annealed at 90 ^{O}C the grain growth is random that is consisting of small and enormous grains (Fig. 5.3 a, b). This enormous grain growth suggests Ostwald ripening, i.e. large grain grows at the cost of small grains in the presence of recycled DMF vapour (due to slow evaporation of DMF and slow decomposition of DMF-BiI_3 complex).[26] In addition to it, BiI_3 films processed at 90 ^{O}C also shows some rod-like morphology at

some other region of the film with several cracks in between the layers as shown in Figure 5.5. The origin of different morphology within the same film is still for an unknown reason but it is speculated to the polydispersity grain growth. With the increase in temperature up to 150 ^{O}C the morphology changes with large grain growth (Fig. 5.3 c-f) and improvement in uniformity (Fig. 5.4 b, c). The change in homogeneity, with processing temperature, can be attributed to imbalance between solvent evaporation rate and BiI_3 thin film formation rate i.e. at lower temperature (90 and 120 ^{O}C) the solvent evaporation rate is much slowed down (due to Petri dish cover) causing accumulation of BiI_3 crystals, in the presence of DMF recycled vapour, resulting in enormous grain growth and large number of pinholes (Figure 5.4 a). However, with an increase in temperature the solvent evaporation rate is enhanced stemming to uniformity of BiI_3 films as can be seen for film processed at 120 ^{O}C (Figure 5.4 b) in which it improved slightly in comparison to films processed at 90 ^{O}C (Figure 5.4 a). At 150 ^{O}C processing condition, the evaporation rate of solvent and BiI_3 film formation rate is balanced resulting in large grains and non-accumulation of BiI_3 crystals as shown in Figure 5.3 e and 5.4 c respectively. Also, at 150 ^{O}C processing temperature, BiI_3 layer shows both pinhole and pinhole free layer within the film as shown in Fig. 5.5 and the observed number of the pinhole (in pinhole containing region) are relatively less in comparison to film processed at 90 and 120 ^{O}C. Moreover, with further increase in temperature, from 150 ^{O}C to 180 ^{O}C, the films show small grains, a large number of pinholes (Fig. 5.3 g, h) with non-uniform growth (Fig. 5.4 d) most likely due to rapid evaporation of the solvent (above the boiling point of DMF). The schematic representation of solvent evaporation rate vs grain growth at various processing condition is illustrated in Figure 5.6. Also, with 180 ^{O}C annealing temperature, we observe visible degradation of BiI_3 layer (brown layer forms on the inner upper wall of Petri dish) as shown in Figure 5.7 which can be the reason for the formation of large number of pinholes. However, in all cases, after several attempts, pinholes were still present but less number of pinholes (and no pinholes at some other region) were observed for BiI_3 films processed at 150 ^{O}C in comparison to other cases studied. It is reported that BiI_3 is a very soft material with a Vickers Hardness of 12-15 [ref. 31] and when the material is heated or cooled down in adhesion to its neighboring layers, cracks and pinholes are easy to form[18] which can be the reason for the cracks (Figure 5.5) and pinholes (Figure 5.3 and 5.4) observed in present study.

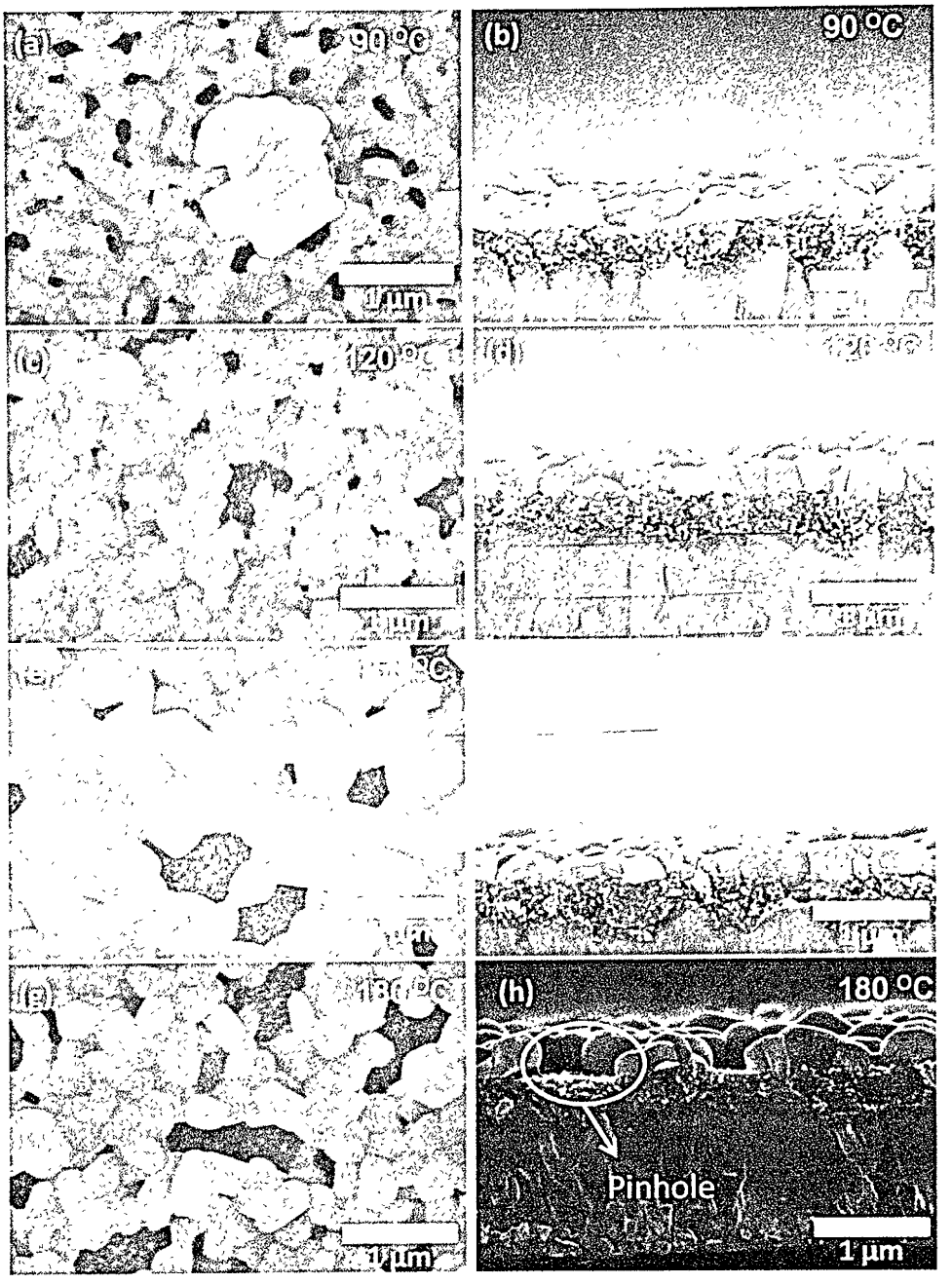

Figure 5.3: Top surface and cross-sectional SEM images of BiI_3 films processed at (a, b) 90 ^{O}C, (c, d) 120 ^{O}C, (e, f) 150 ^{O}C and (g, h) 180 ^{O}C.

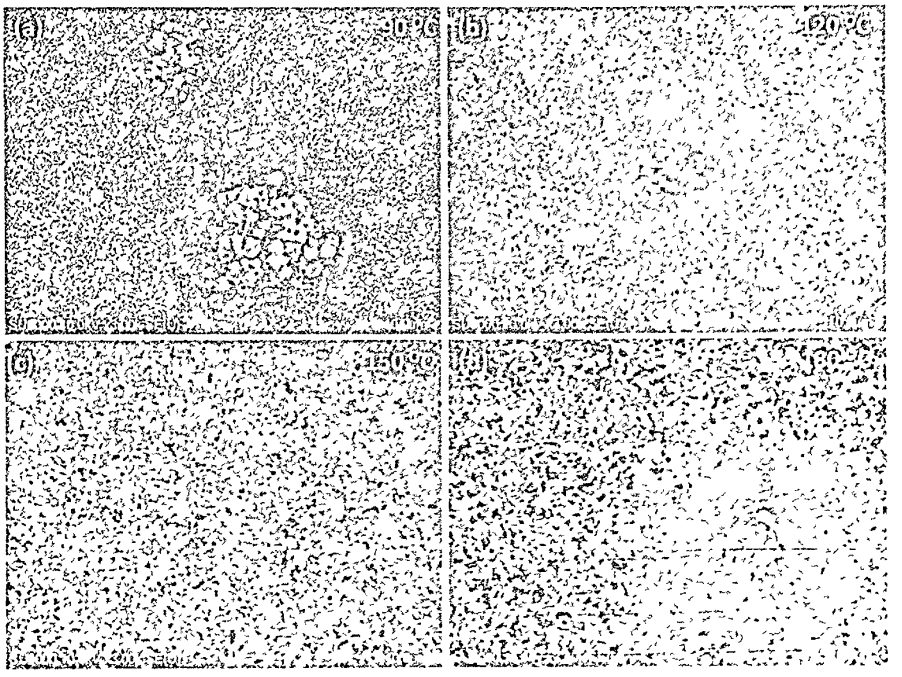

Figure 5.4: Top surface SEM image of BiI_3 film processed at (a) 90 ^{o}C, (b) 120 ^{o}C, (c) 150 ^{o}C, (d) 180 ^{o}C.

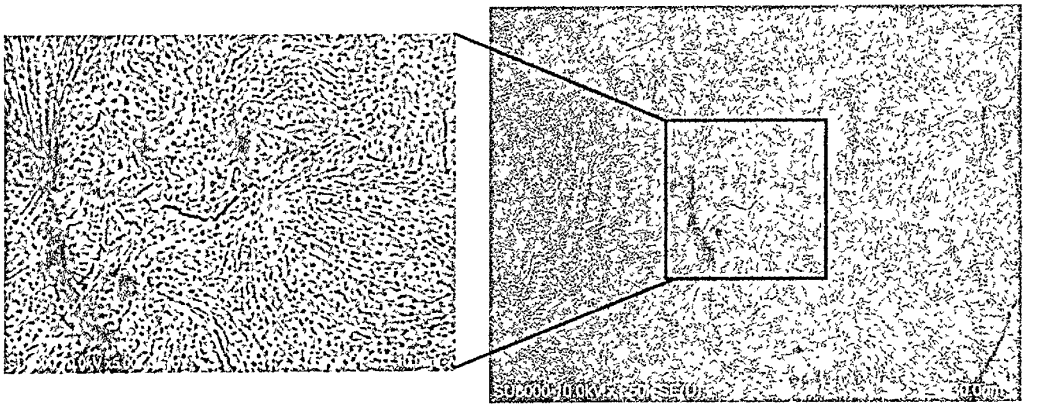

Figure 5.5: Top surface SEM image of BiI_3 films processed at 90 ^{o}C showing rod-like morphology with cracks.

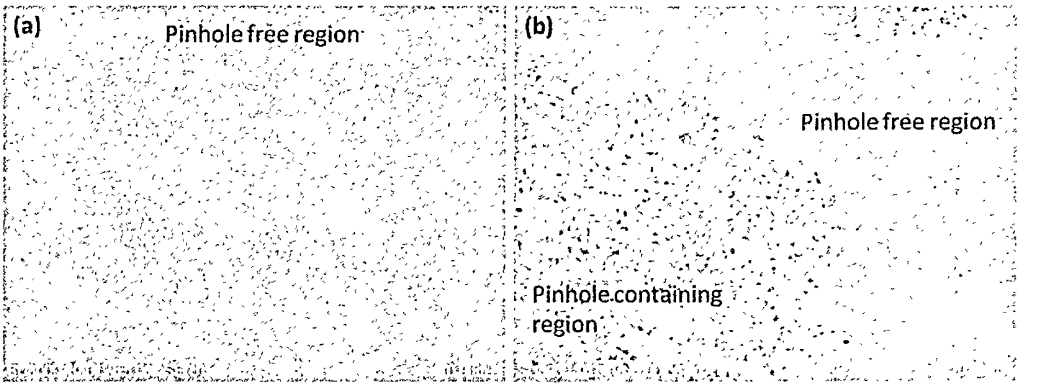

Figure 5.6: BiI_3 film processed at 150 °C with PR-VA treatment showing (a) pinhole free region and (b) both pinhole containing and pinhole free region.

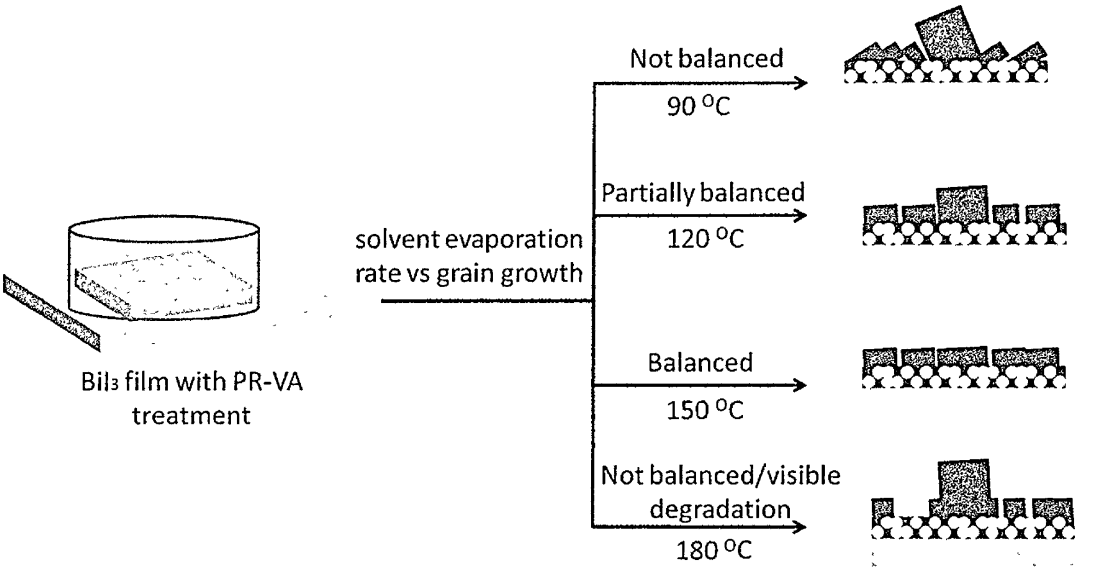

Figure 5.7: Schematic illustration of BiI_3 films with PR-VA treatment at various processing temperature showing DMF solvent evaporation rate vs BiI_3 grain growth.

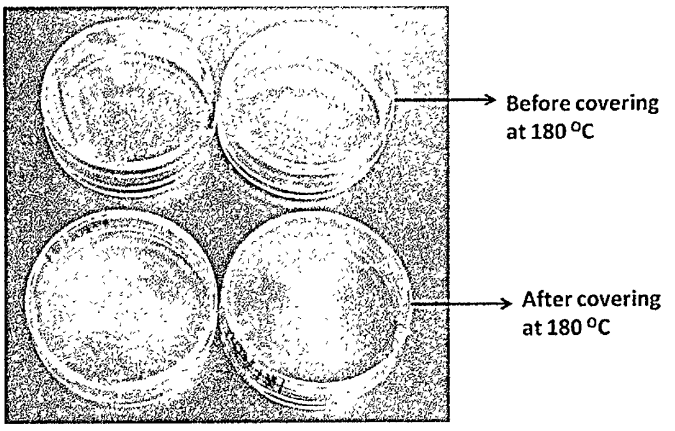

Figure 5.7: Images of Petri dish (above) before covering and (below) after covering the BiI_3 films at 180 °C showing visible degradation.

X-ray diffraction (XRD) measurement was performed to study the crystal structure and orientation of BiI_3 layer deposited on the mesoporous layer. Herein, the relative intensity of BiI_3 XRD peak is improved with PR-VA treatment in contrast to TA treatment as shown in Figure 5.8a indicating higher crystallinity in the former case. Hence, PR-VA treatment was employed to further study the effect of temperature on XRD pattern of the BiI_3 thin film. Figure 5.8b depicts BiI_3 films annealed at 90 °C show two major characteristic peaks at ~12° and ~12.7° which are assigned to (003) and (101) phase of BiI_3. Previously in the planar structured BiI_3 device, Hamdeh et al. observed preferred crystallographic orientation along (113) and (300) direction and (003) and (101) orientation of BiI_3 was not observed.[26] Figure 5.8 c and d further show the zoomed (101) and (113) diffraction peak at ~12° and ~27° whose intensity gradually increases with the annealing temperature. Additionally, from Figure 5.8 b it can also be seen that (300) oriented peak at ~42° shows slight enhancement in peak intensity with the annealing temperature from 90 °C to 120 °C and thereafter remains constant. This evidences that with an increase in processing temperature the BiI_3 grain growth is more in (101), (113), and (300) preferred orientation further supporting the variation of grain growth observed in SEM images (Figure 5.3). The weaker intensity at low processing temperature can be due to the random morphology (polydispersity of grains) and even though solvent-mediated peak was not observed it can be said, on a minor note, that solvent DMF may appear to be embedded within the matrix making it an amorphous material[26] due to which the diffraction intensity is

weak and with increase in temperature the DMF gets evaporated from the matrix leading to tuned morphology, high intense peaks, and better crystallinity. Additionally, XRD diffraction pattern was resolved into $R\bar{3}$ space group and are in well agreement with previous reports.[18, 26]

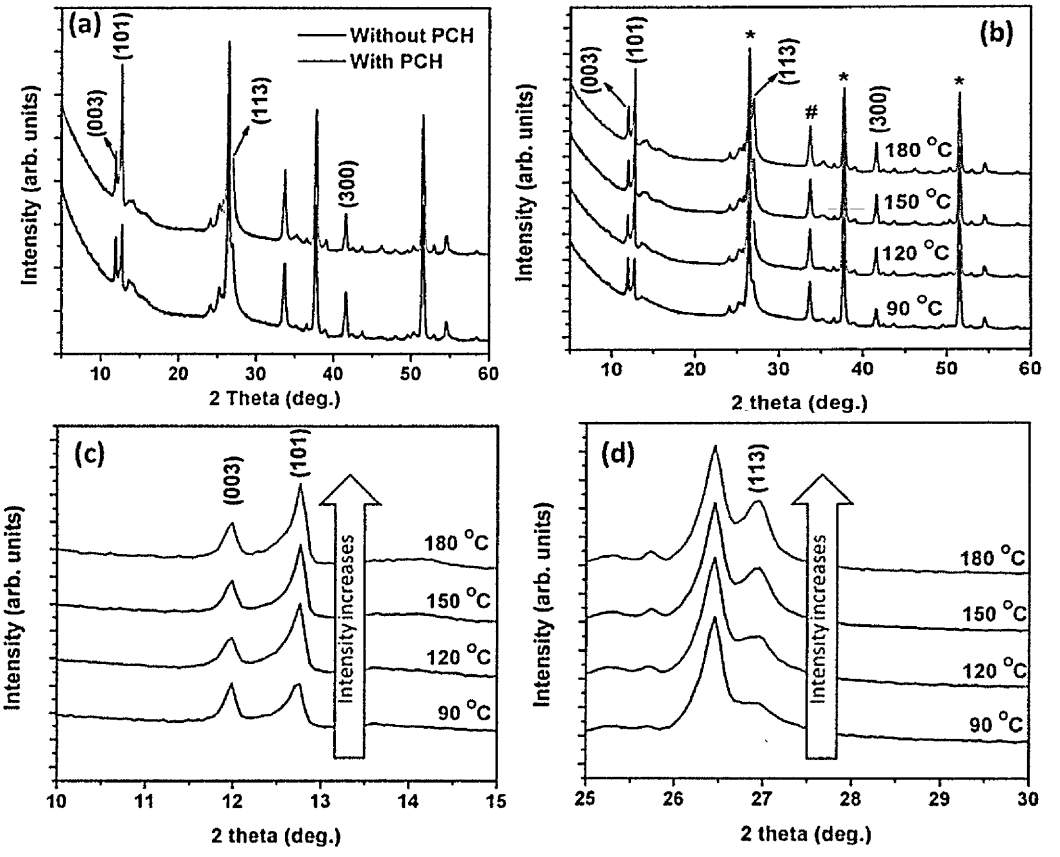

Figure 5.8: XRD pattern of the BiI_3 films processed (a) without and with PR-VA treatment, (b) at various temperatures, its corresponding zoomed (c) (101) oriented peak and (d) (113) oriented peak. * and # corresponds to FTO and TiO_2 respectively.

5.3.2 Photovoltaic device performance and long-term stability

Solar cells using BiI_3 as an active layer were fabricated with widely used spiro-OMeTAD with dopants as HTM. Figure 6a depicts the energy level diagram[25] and the cross-section SEM image of a BiI_3 solar cell showing stacks of layers in the structured configuration of FTO/TiO_2 (BL + meso.)/BiI_3/Spiro-OMeTAD/Au. The effect PR-VA

treatment at various annealing temperatures on the device performance was investigated as shown in Figure 5.9 b and the photovoltaic parameters are tabulated in Table 5.1. The statistics of the photovoltaic parameters obtained from 5 batches (50 devices of each kind) are shown in Figure 5.9 c. From the statistics plot it can be seen that the short-circuit current density (J_{sc}) increases with the increase in temperature (90 ^{O}C to 150 ^{O}C) which can be credited to the tuned morphology, large grains, (Figure 5.3) and preferred crystallographic orientation of BiI_3 crystals as evident from XRD pattern (Figure 5.8). It is suspected that grain growth in (101), (113) and (300) preferred orientation favors improvement in J_{sc} and device performance, however, detail investigation is required to validate this. Although, BiI_3 films processed at 180 ^{O}C shows enhanced intensity of (101) and (113) peaks, observed BiI_3 visible degradation (Figure 5.7) (as mentioned above) resulting in small grain sizes, many pinholes (Figure 5.3 h, g, 5.4) and non-uniform growth (Figure 5.4 d), attributes to decrease in overall performance (Figure 5.9 c). Further from Figure 5.9 c it is evident that among all the cases studied, BiI_3 films processed at 150 ^{O}C shows best device performance with minimum, average and maximum PCE of 0.44%, 0.48% and 0.5% respectively (Figure 5.10) and from the histogram plot (Figure 5.10) it is also evident that the results are statistically significant and reproducible. It is to be noted that the obtained PCE is among the highest value reported in TiO_2 mesoporous structured BiI_3 solar cells employing organic HTM. Figure 5.9 d shows the forward and reverse scan of best-performing device J-V curve (processed at 150 ^{O}C), measured under simulated AM 1.5 G solar illumination, showing negligible hysteresis. Also, devices with TA and SVA processed film were fabricated and as expected the device shows poor performance in comparison to PR-VA processed BiI_3 device as shown in Fig. 5.11 and Table 5.2. Figure 5.9 e shows the incident photon to conversion efficiency (IPCE) or external quantum efficiency of the best performing device which covers the visible spectra with sharp absorption onset around ~720 nm and is in good agreement with BiI_3 optical band gap (~1.8 eV). Integration of IPCE spectra yielded short-circuit photo-current density of 3.43 mA/cm^2 which is well matching with the J_{sc} value (3.6 mA/cm^2) obtained from J-V measurement.

Table 1: Photovoltaic parameters of best performing BiI_3 device J-V curves obtained with different processing conditions

Processing Temperature (^{O}C)	J_{sc} (mA/cm^2)	V_{oc} (V)	FF	PCE (%)
90	1.35	0.30	0.33	0.14
120	1.98	0.31	0.37	0.24
150	3.6	0.32	0.41	0.5
180	2.71	0.23	0.35	0.23

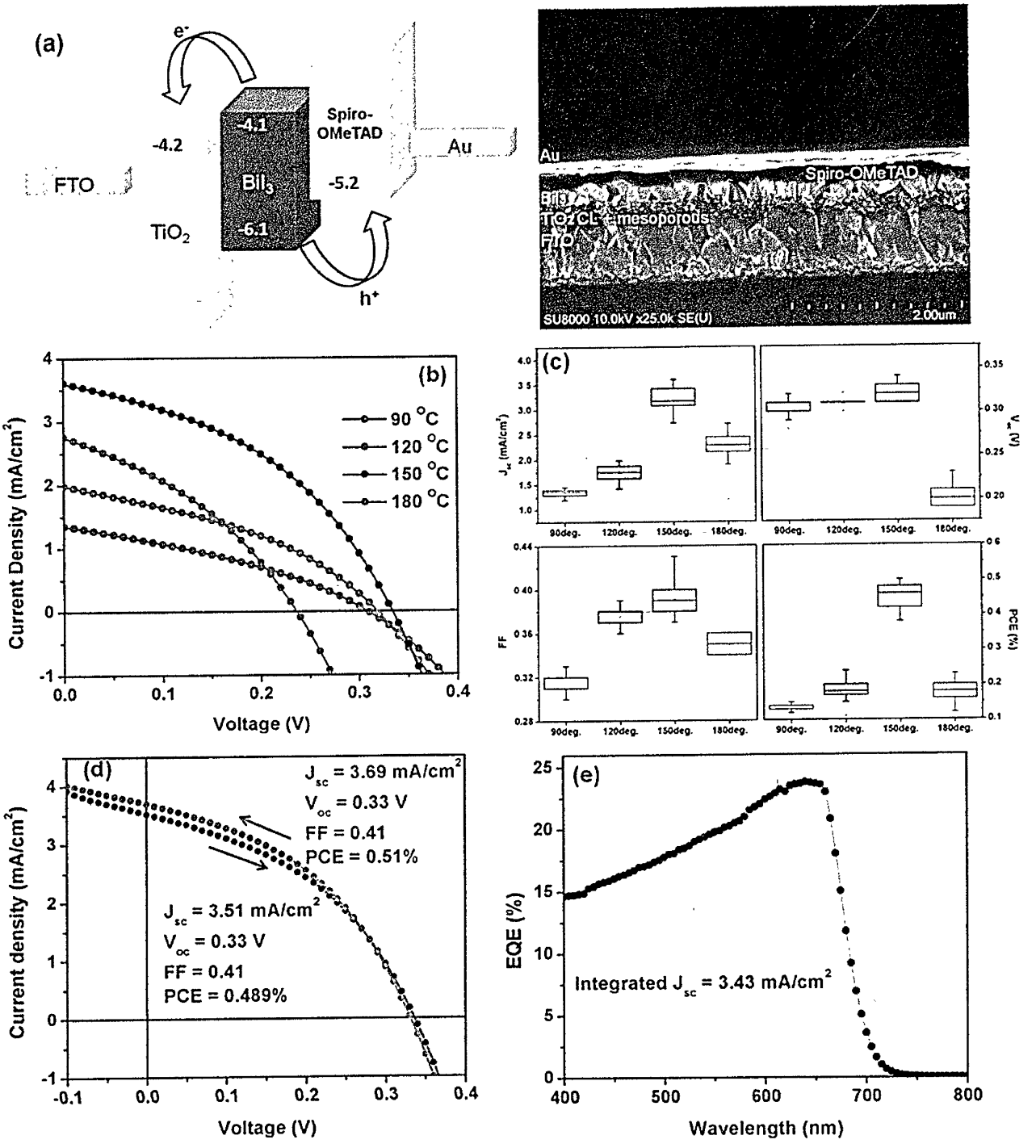

Figure 5.9: (a) Energy level diagram and device cross-section image of BiI_3 photovoltaic device, (b) best performing BiI_3 device J-V curves processed with different heating temperature, (c) its corresponding device statistics, (d) J-V curve with forward and reverse scan and its corresponding (e) IPCE spectra.

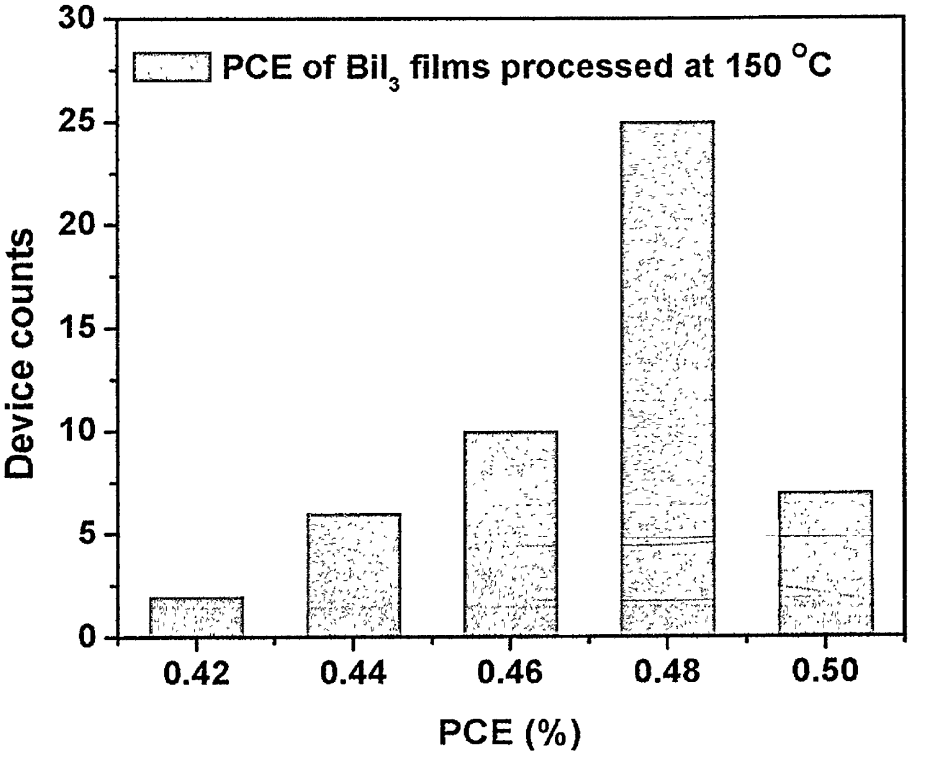

Figure 5.10: Conversion efficiency histogram plot of BiI_3 photovoltaic devices.

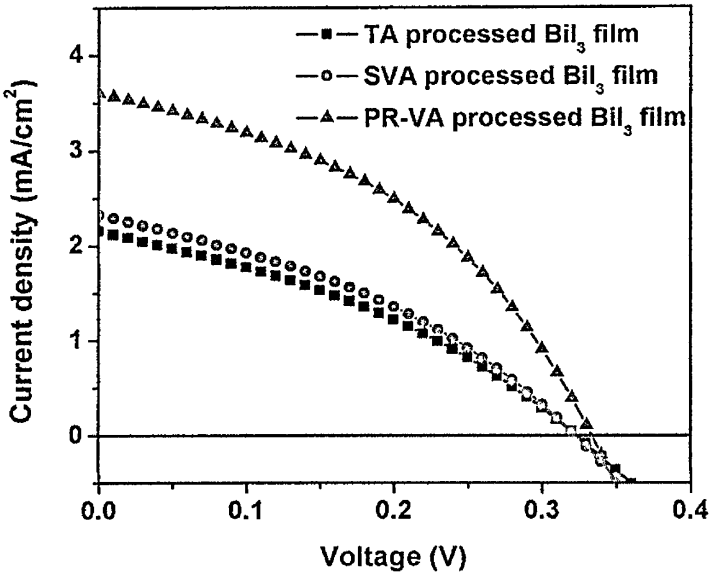

Figure 5.11: J-V characteristics of best performing device with TA, SVA, and PR-VA processed BiI_3 film.

Table 5.2: Device parameters of BiI_3 film processed under various conditions.

Condition	J_{sc} (mA/cm^2)	V_{oc} (V)	FF	PCE (%)
TA	2.15	0.32	0.35	0.24
SVA	2.32	0.32	0.36	0.27
PR-VA	3.6	0.32	0.41	0.5

High variation in the grain size for the film processed at 90 ^{O}C results in poor interfacial contacts leading to low FF and with increase in temperature to 120 ^{O}C and to 150 ^{O}C the FF slightly improved due to improvement in the uniformity of grain growth and due to better interfacial contact with neighboring charge collecting layer (Fig. 5.9 c). However, it can be noted that even though the J_{sc} improved effectively with an increase in processing temperature, FF almost remains in a narrow range (for BiI_3 films processed at 120 and 150 ^{O}C). Additionally, in all cases, we observe low V_{oc} (0.3 V) which does not differ with improvement in morphology except for the case of 180 ^{O}C annealing case in which V_{oc} degraded due to a loss in BiI_3 layer (Fig. 5.9 c). There can be several reasons for low V_{oc} and FF which includes: BiI_3 has lot of iodine vacancies[32] and surface defects resulting in shallow traps[32] which makes it much easier for charge carriers to recombine, electron diffusion length of BiI_3 is much less than lead perovskites and also the electron mobility is reported to be 30 times higher than the hole mobility.[18] This unbalanced charge mobilities and low diffusion length can cause inefficient charge transport. Additionally, BiI_3 itself possess high resistivity up to 10^8 to 10^9 Ω-cm resulting in high series resistance.[33] Such high resistivity results in short carrier lifetime (below 200 ps).[18] Large atomic mass of Bi^{3+} leads to deeper 6s orbitals and less contribution to valance band resulting in high hole effective masses.[18] All the above-mentioned reason can severe affect V_{oc} and FF of the device. Additionally, EQE spectra (Fig. 5.9 e) evidences relatively poor extraction of higher energy photons which implies that there is a loss in photo-generated charge carriers extraction near TiO_2/BiI_3 interface.[26] This also indicates the presence of defect states at this interface which causes recombination of photo-generated charge carriers.[26] Also, in accordance with prior reports[25] and from schematic illustration (Figure 5.9 a) the poor alignment of valence band maximum (VBM) between spiro-OMeTAD and BiI_3 limits efficient charge transport. Further stability test of the best performing BiI_3 devices was performed. The PCE remains

above 0.45% for over 30 days after exposing them to ambient atmosphere of relative humidity of 50% as shown in Figure 5.12 a. We also perform a light soaking test of the freshly prepared device by exposing them to continuous illumination for 1 hours using 100 $mWcm^{-2}$ AM 1.5 G as shown in Figure 5.12 b. No much degradation of BiI_3 devices is seen after 1-hour illumination, PCE degraded from 0.5% to 0.47%. This result highlights promising stability of the BiI_3 material.

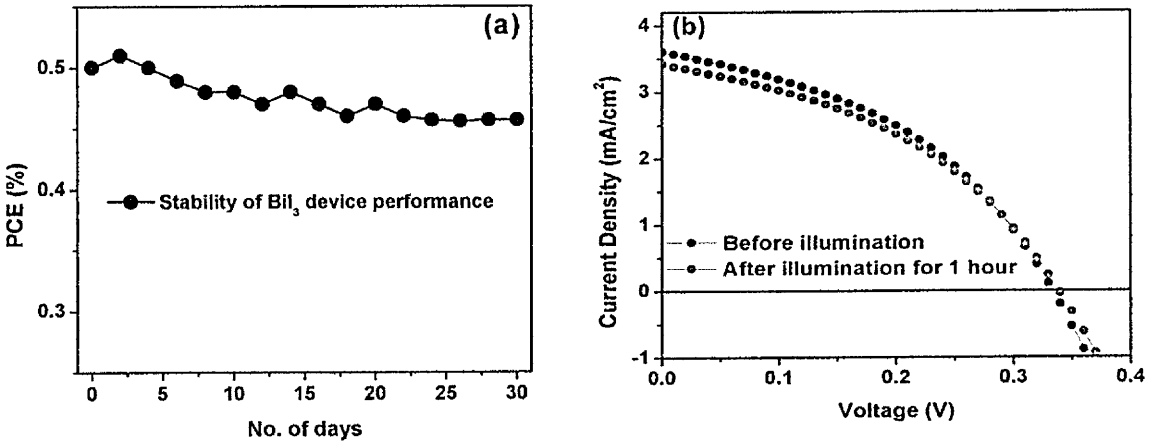

Figure 5.12: PCE of BiI_3 device after exposing to (a) ambient atmosphere (relative humidity 50%) and (b) 1 hour light soaking test.

Based on the results, BiI_3 photovoltaic device conversion efficiency can be further enhanced by mitigating intrinsic high resistive property of BiI_3[33] by external doping which leads to low series resistance and low recombination rate. Thin film devices based on CdTe with comparable carrier lifetime with that of BiI_3 have demonstrated PCE of 8 to 9%[34] further suggesting improvement in BiI_3 material development (eliminating impurities such as bismuth interstitial sites and vacancies) and device engineering protocols. Also, the difference between carrier lifetime of single crystal and polycrystalline thin film of BiI_3 prospects the route to enhance carrier lifetime of the polycrystalline film by phase purity and/or intragranular structural defects.[18] Additionally, as mentioned earlier, BiI_3 is very soft material which presents challenges to device fabrication.[31]

In addition to tuning the intrinsic properties of BiI_3, device architecture needs much modification for efficient charge carrier extraction. As mentioned earlier, the loss of higher energy photons evinces amendment of TiO_2/BiI_3 interface and/or choice of the suitable

electron collecting layer. The choice of suitable HTM is also important as the VBM of BiI_3 and widely used spiro-OMeTAD is highly mismatching. Resolving the above-mentioned issues can pave a path to enhance the conversion efficiency of non-toxic bismuth halide solar cells.

5.4 Conclusion

In summary, meso-structured BiI_3 films were prepared by simple solution process and PR-VA treatment (during the heating step) showed better morphology with less number of pinholes compared to SVA and TA treatment. A further effect of different annealing temperature on the BiI_3 layer morphology and orientation was investigated. Among all the processing temperature, BiI_3 films processed at 150 ^{O}C showed better performance in comparison to other cases due to effective enhancement in J_{sc}. However, V_{oc} and FF were not highly affected with the annealing temperature (90 to 150 ^{O}C) and a further increase in temperature to 180 ^{O}C resulted in visible degradation of BiI_3 layer resulting in lowering of device performance. Moreover, BiI_3 devices (stored in dark) were quite stable for up to 30 days after exposing to 50% relative humidity and devices stored under light showed slight degradation under the same condition. Light soaking for 1 hour further confirmed the stability of BiI_3 devices. Lastly, this study demonstrates the initial efficiency of 0.5% of BiI_3 devices in TiO_2 mesostructured architecture employing widely used spiro-OMeTAD as HTM and we expect more enhancements in highly air-stable BiI_3 device efficiency by tuning intrinsic properties of the BiI_3 material, choice of suitable charge collecting layers and device engineering processes.

5.5 References

1 (a) Kojima, A.; Teshima, K.; Shirai, Y.; Miyasaka, T., *J. Am. Chem. Soc.* **2009**, *131*, 6050-6051, (b) Miyasaka, T., *Chem. Lett.*, **2015**, *44*, 720-729, (c) Yang, W. S.; Park, W. B.; Jung, E. H.; Jeon, N. J.; Kim, Y. C.; Lee, D. U.; Shin, S. S.; Seo, J.; Kim, E. K.; Noh, J. H.; Seok, S. I., *Science*, **2017**, *356*, 1376-1379, (d) Lee, M. M.; Teuscher, J.; Miyasaka, T.; Murakami, T. N.; Snaith, H. J., *Science*, **2012**, 338 (6107), 643-647, (e) Stranks, S. D.; Eperon, G. E.; Grancini, G.; Menelaou, C.; Alcocer, M. J. P.; Leijtens, T.; Herz, L. M.; Petrozza, A.; Snaith,

H. J., *Science*, **2013**, *342*, 341-344, (f) Pazos-Outon, A. M.; Szumilo, M.; Lamboll, R.; Richter, J. M.; Crespo-Quesada, M.; Abdi-Jalebi, M.; Beeson, H. J.; Vrucinic, M.; Alsari, M.; Snaith, H. J.; Ehrler, B.; Friend, R. H.; Deschler, F., *Science*, **2016**, *351 (6280)*, 1430-1433.

2 Legitens, T.; Bush, K.; Cheacharoen, R.; Beal, R.; Bowring, A.; McGehee, M. D., *J. Mater. Chem. A*, **2017**, *5*, 11483-11500.

3 (a) Jeon, N. J.; Noh, J. H.; Yang, W. S.; Kim, Y. C.; Ryu, S.; Seo, J.; Seok, S. I., *Nature*, **2015**, *517*, 476-480, (b) Jeon, N. J.; Noh, J. H.; Kim, Y. C.; Yang, W. S.; Ryu, S.; Seok, S. I., *Nature Materials*, **2014**, *13*, 897-903, (c) Saliba, M.; Matsui, T.; Seo, J-Y.; Domanski, K.; Correa-Baena, J-P.; Nazeeruddin, M. K.; Zakeeruddin, S. M.; Tress, W.; Abate, A.; Hagfeldt, A.; Gratzel, M., ***Energy Environ. Sci.***, **2016**, ***9***, 1989-1997, (d) Saliba, M.; Matsui, T.; Domanski, K.; Seo, J-Y.; Ummadisingu, A.; Zakeeruddin, S. M.; Correa-Baena, J-P.; Tress, W. R.; Abate, A.; Hagfeldt, A.; Gratzel, M., *Science*, **2016**, DOI: 10.1126/science.aah5557.

4 (a) Kulkarni, A.; Jena, A. J.; Chen, H.-W.; Sanehira, Y.; Ikegami, M.; Miyasaka, T., *Solar Energy*, **2016**, *136*, 379-384, (b) Chaudhary, B.; Kulkarni, A.; Jena, A. J.; Ikegami, M.; Udagawa, Y.; Kunugita, H.; Ema, K.; Miyasaka, T., *ChemSusChem*, **2017**, DOI: 10.1002/cssc.201700271, (c) Pinpithak, P.; Chen, H.-W.; Kulkarni, A.; Sanehira, Y.; Ikegami, M.; Miyasaka, T., *Chem. Lett.*, **2017**, *46 (3)*, 382-384, (d) Domanski, K.; Correa-Baena, J.-P.; Mine, N.; Nazeeruddin, M. K.; Abate, A.; Saliba, M.; Tress, W.; Hagfeldt, A.; Gratzel, M., *ACS Nano*, **2016**, *10* (6), 6306–6314.

5 Babayigit, A.; Ethirajan, A.; Muller, M.; Conings, B., *Nature Materials*, **2016**, *15*, 247-251.

6 Konstantakou, M.; Stergiopoulous, T., *J. Mater. Chem. A*, **2017**, *5*, 11518-11549.

7 Krishnamoorthy, T.; Ding, H.; Yan, C.; Leong, W. L.; Baikie, T.; Zhang, Z.; Sherburne, M.; Li, S.; Asta, M.; Mathews, N.; Mhaisalkar, S. G., *J. Mater. Chem. A*, **2015**, *3*, 23839-23832.

8 Singh, T.; Kulkarni, A.; Ikegami, M.; Miyasaka, T., *ACS Appl. Mater. Interfaces*, **2016**, *8* (23), 14542–14547

9 Kulkarni, A.; Singh, T.; Ikegami, M.; Miyasaka, T., ***RSC Adv.***, **2017**, *7*, 9456-9460.

10 Hebig, J.-C.; Kuhn, I.; Flohre, J.; Kirchartz, T., *ACS Energy Lett.*, 2016, *1 (1)*, 309-314.

11 Shi, Z.; Guo, J.; Chen, Y.; Li, Q.; Pan, Y.; Zhang, H.; Xia, Y.; Huang, W., *Adv. Mater.*, **2017**, *29 (16)*, 1605055

12 Park, B.-W.; Philippe, B.; Zhang, X.; Ransmo, H.; Boschloo, G.; Johansson, E. M. J., *Adv. Mater.*, **2015**, *27*, 6806-6813.

13 Ran, C.; Wu, Z.; Xi, J.; Yuan, F.; Dong, H.; Lei, T.; He, X.; Hou, X., *J. Phys. Chem. Lett.*, **2017**, *8* (2), 394–400.

14 Mali, S. S.; Kim, H.; Kim, D.-H.; Hong, C. K., *Chemistry Select*, **2017**, *2(4)*, 1578-1585.

15 Zhang, Z.; Li, X.; Xia, X.; Wang, Z.; Huang, Z.; Lei, B.; Gao, Y., *J. Phys. Chem. Lett.*, **2017**, *8 (17)*, 4300-4307.

16 Slavney, A. H.; Hu, T.; Lindenberg, A. M.; Karunadasa, H. I., *J. Am. Chem. Soc.*, **2016**, *138 (7)*, 2138-2141.

17 Savory, C. N.; Walsh, A.; Scanlon, D. O., *ACS Energy Lett.*, **2016**, *1 (5)*, 949-955.

18 Brandt, R. E.; Kurchin, R. C.; Hoye, R. L. Z.; Poindexter, J. R.; Wilson, M. W. B.; Sulekar S.; Lenahan, F.; Yen, P. X. T.; Stevanovic, V.; Nino, J. C.; Bawendi, M. G.; Buonassisi, T., *J. Phys. Chem. Lett.*, **2015**, *6*, 4297-4302.

19 (a) Green, M. A.; Keevers, M. J., *Prog. Photovoltaics*, **1995**, *3*, 189−192, (b) Blakemore, J. S., *J. Appl. Phys.*, **1982**, *53*, R123−R181.

20 Mackay, R. A.; Henderson, W., 6th ed.; CRC Press: 2002

21 Nason, D.; Keller, L., *J. Cryst. Growth*, **1995**, *156*, 221-226.

22 Cuna, A.; Aguiar, I.; Gancharov, A.; Perez, M.; Fornaro, L., *Cryst. Res. Technol.*, **2004**, *39*, 899-905.

23 Cuna, A.; Noguera, A.; Saucedo, E.; Fornaro, L., *Crys. Res. Technol.*, **2004**, *39*, 912-919.

24 Boopathi, K. M.; Raman, S.; Mohanraman, R.; Chou, F.-C.; Chen, Y.-Y.; Lee, C.-H.; Chang, F.-C.; Chu, C.-W., *Sol. Energy Mater Sol. Cells*, **2014**, *121*, 35-41.

25 Lehner, A. J.; Wang, H.; Fabini, D. H.; Liman, C. D.; Hebert, C.-A.; Perry, E. E.; Wang, M.; Bazan, G. C.; Chabinyc, M. L.; Seshadri, R., *Appl. Phys. Lett.*, **2015**, *107*, 131109.

26 Hamdeh, U. M.; Nelson, R. D.; Ryan, B. J.; Bhattacharjee, U.; Petrich, J. W.; Panthani, M. G., *Chem. Mater.*, **2016**, *28 (18)*, 6567-6574.

27 Xiao, Z.; Dong, Q.; Bi, C.; Shao, Y.; Yuan, Y.; Huang, J., *Adv. Mater.*, **2014**, *26*, 6503-6509.

28 Numata, Y.; Kogo, A.; Udagawa, Y.; Kunugita, H.; Ema, K.; Sanehira, Y.; Miyasaka, T., *ACS Appl. Mater. Interfaces*, **2017**, *9*, 18739-18747.

29 Katayama, M.; Ozutsumi, K., *J. Solution Chem*, **2008**, *37*, 841.

30 Sinturel, C.; Vayer, M.; Morris, M.; Hillmyer, M. A., *Macromolecules,* **2013**, *46*, 5399–5415.

31 Baciak, J. E.; Nino, J. C.; Qiu, W.; Lintereur, A., DTRA-TR-12-70; DTIC Document, 2013.

32 Curtis, B. J.; Brunner, H. R., *Materials Research Bulletin*, **1974**, *9*, 715-720.

33 Lintereur, A. T.; Qiu, W.; Nino, J. C.; Baciak, J., *Nucl. Instrum. Methods Phys. Res., Sect. A* **2011**, *652*, 166–169.

34 Moutinho, H. R.; Dhere, R. G.; Al-Jassim, M. M.; Ballif, C.; Levi, D. H.; Swartzlander, A. B.; Young, M. R.; Kazmerski, L. L., *Photovoltaic Specialist Conference (PVSC)*, **2000 IEEE 28th 2000**, 646–649.

Chapter 6

Study of Various Silver Bismuth Halide Perovskite-like Materials for Photovoltaic Applications

Abstract

Organic-inorganic lead halide perovskite undergoes degradation when exposed to moisture, oxygen, heat and continuous light illumination, further exposing the toxic lead iodide (degraded product) to the environment. For better optical properties three-dimensional materials are superior to lower dimensional one due to lower exciton binding energy and suitable band gap. Herein, studies on various perovskite-like silver-bismuth halide materials are presented which possess edge sharing octahedral cubic crystal structure. In the first part of this chapter studies on corrosion of Ag_3BiI_6 in the presence of dopants that are used in spiro-OMeTAD and choice for suitable hole transporting material (HTM) is presented. Second part of this thesis present study on the role of precursor solvent (butylamine and DMSO) on the morphology, grain growth, crystal orientation, conversion efficiency and degradation of $AgBi_2I_7$ and Ag_2BiI_5 materials. Further direction for efficiency enhancement of non-toxic silver-bismuth halide materials based photovoltaic devices is presented.

6.1 Introduction

Following the seed technologies of organic-inorganic lead halide perovskite solar cells by Miyasaka et al. in 2006 and 2009 reporting 2.2% and 3.8% respectively,[1,2] power conversion efficiency (PCE) of perovskite solar cells sky rocketed to certified 22.7% in just 10 years.[3] Such steep rise in PCE is credited to its exceptional optoelectronic properties such as ambipolar charge mobility, sharp urbach tail, narrow band gap, photon recycling capability, long carrier diffusion length etc.[4, 5, 6] and simple solution facile fabrication process,[7] offering substantial cost reduction compared to already established technologies. Despite of several advantages, lead perovskite suffers from long term stability as it gets degrades upon exposure to moisture, heat, UV-light and oxygen and faces criticism due to use of toxic materials (PbI_2).[8] The solubility constant (K_{sp}) of PbI_2 is reported to be 4.4×10^{-9} which is much less than K_{sp} of CdTe (10^{-34}) indicating that Pb can easily get dissolve from the broken photovoltaic (PV) module leading to environment toxication.[9] World Health Organization (WHO) demands maximum blood Pb level of 5 µg/L for children which are quite less than the amount of Pb that is used in the photovoltaic device and hence it can be difficult/quite challenging for Pb-based perovskite to pass the environmental standards for building integrated photovoltaic system.[10] Recently, Babayigit et al. studied the effect of lead perovskite toxicity and reported that exposure of PbI_2 can cause severe damage to nervous and reproductive systems.[11] In order to enhance the stability of the cell and avoid exposure of Pb many efforts have been made by developing and synthesizing stable perovskite materials based on various compositions.[12] In addition to that, interfacial modifications have also shown promising long term stability to several hours to weeks.[13] Also, work on recycling of perovskite solar cells (after degradation) has been carried out at research laboratory level to avoid the exposure of toxic lead into the environment.[14] Apart from moisture and oxygen; heat and continuous light illumination causes degradation of the cell.[15] Robust encapsulation strategies can prevent exposure of cell to moisture and oxygen; however, stability against heat and sunlight illumination is quite questionable and has been less addressed. On the other hand, researchers have also explored other perovskite material based on tin (Sn), germanium (Ge).[16, 17] However, Sn and Ge based perovskite materials are

highly prone to disproportionation or oxidation when exposed to moisture or ambient atmosphere and recently Sn perovskite toxicity concern has been reported.[11, 16]

Due to similar isoelectronic $6s^2$ cation bismuth (Bi), another non-toxic metal, has been used as an alternative to replace Pb.[18] As discussed in chapter 3 and 4, $A_3Bi_2I_9$ class of low dimensional material, with crystal lattice consisting of isolated face $[B_2X_9]$ shared double octahedral unit, has been explored as a photovoltaic candidate due to its exceptional high stability against moisture.[19] To date best PCE of 1.09% and 1.64% has been demonstrated for solar cells based on $Cs_3Bi_2I_9$ and $(CH_3NH_3)_3Bi_2I_9$ respectively which is rather low in comparison to lead perovskites.[20, 21] Even non-perovskite two dimensional (2D) bismuth halide (BiI_3) has also been explored, however, presence of large number of bismuth interstitial defect and indirect bandgap limits its PCE to 1%.[22] It is well known that for better optical properties, three dimensional (3D) materials are better applicant than 2D materials due to low exciton binding energy and high charge carrier lifetime. Towards this end, 3D Bi based double perovskite, in combination with monovalent cation such as silver (Ag^+), copper (Cu^+), have been investigated demonstrating promising optical properties.[23] However, they possess indirect wide band gap (>2.1 eV) and theoretical calculations suggest that these double perovskite may rather have low charge carrier mobilities. Also, few other reports suggest that some other combinations of double perovskites are thermodynamically unstable.[24] Hence alternative higher dimensional non-toxic materials need to be explored with optical properties and narrow band gap which are suitable for photovoltaic applications. Recently family of photovoltaic halides based on edge-sharing $[AX_6]$ and $[BX_6]$ octahedral materials such as Ag_3BiI_6, Ag_2BiI_5, $AgBi_2I_7$, $AgBiI_4$ etc., having a general formula of $A_aM_mX_x$, where A = Ag, Cu; M = Bi, Sb; X = I, Br and m = a+3b have emerged.[10] Edge sharing ABX prototype materials were discovered by Rudorff in 1954 and hence named as "rudorffites" which forms three-dimensional lattice in which the cation sublattice can be descried as joint populations of monovalent, trivalent and neutral vacant sites with different occupancies.[10] Even though Ag-Bi-I and Cu-Bi-I materials exhibit quite poor ionic conductivity even at elevated temperatures, these materials were widely investigated as potential ionic conductors. Although Ivan et al.[10] suggested ABX prototype material structure to be edge sharing octahedra, Zhu et al. reported the hexagonal trigonal structure of Ag_2BiI_5 with R3m space group and cell parameters of a = 4.350 Å, c = 20.82 Å.[25] Regarding

$AgBi_2I_7$, initially Kim et al. reported that the structure of $AgBi_2I_7$ corresponds to cubic $ThZr_2H_7$ prototype structure.[26] Later, Xiao et al. suggested that $AgBi_2I_7$ cannot form $ThZr_2H_7$-type structure due to short Bi-I bond length in the $[BiI_8]$ hexahedra resulting in unreasonably large mass density and further suggested that Ag-deficient cubic $AgBiI_4$ is formed with lattice constant a= 12.2223 Å.[27] As the crystal structure of $AgBi_2I_7$ is unclear, from hereafter $AgBi_2I_7$ (based on stoichiometry) refers to either $AgBi_2I_7$ or $AgBiI_4$. Recently, photovoltaic properties of series of Ag-Bi halide material with molar ratio of BiI_3/AgI = 2:1, 1:3, 1:2 forming Ag_3BiI_6, Ag_2BiI_5, and $AgBi_2I_7$ respectively have been reported due to their favorable bandgap of ~1.8 eV which is suitable for single junction and tandem architecture devices.[10, 25, 26] The present study aims to study the effect of dopants used in spiro-OMeTAD (HTM), choice of suitable HTM for Ag_3BiI_6 and the role of precursor solvent in further enhancing the efficiency of Ag_2BiI_5 and $AgBi_2I_7$ based photovoltaic devices.

6.2 Experimental

6.2.1 Device fabrication

Fluorine doped tin oxide (FTO) (10 Ω/□, NSG Group, Japan) conductive glass substrates were washed by ultrasonic treatment with commercial detergent (2% Hellmanex in water), deionized water (DI), acetone and 2-propanol for 15 minutes each. All the chemicals were used as received without any further purification. The substrates were given UV-ozone treatment for 10 min before coating TiO_2 compact layer.

TiO_2 compact layer coating: Solution of titanium diisopropoxide bis(acetylacetonate) (Ti acac) (75 wt% in isopropanol, Sigma-Aldrich) in ethanol (99.99%, Wako) was spray coated on to cleaned FTO coated glass substrates at 500 ^{O}C to obtain 50 nm thick TiO_2 compact layer (CL) and allowed the substrates to remain at the same temperature for 30 min followed by cooling down naturally to room temperature.

TiO_2 Mesoporous layer coating: Anatase TiO_2 mesoporous layer were spin coated using a commercially available TiO_2 paste (18NR-T, Dyesol, particle size ~20 nm) diluted in 25 wt% ethanol at 3000 rpm/30 sec followed by sintering at 500 ^{O}C for 1 hour in muffle furnace. After cooling down the meso-structured substrates were given 40 mM $TiCl_4$ treatment at 70 ^{O}C for 30 min. The substrates were rinsed and cleaned with distilled water

and ethanol and were again sintered at 500 ^{O}C for 30 min. The coated substrates were given UV-ozone treatment for 10 min prior to the BiI_3 layer deposition.

Active layer deposition: Different molar ratio of bismuth triiodide (BiI_3) and silver iodide (AgI) in either butylamine or DMSO were stirred on a hot plate at 50 ^{O}C for 1 hour prior to the coating. For Ag_3BiI_6, Ag_2BiI_5 and $AgBi_2I_7$ ($AgBiI_4$), BiI_3 and AgI were added in 1:3, 1:2, 2:1 molar ratio respectively. The rudorffite perovskite solution was spin coated on TiO_2 mesoporous coated substrates at 1500/30 sec when dissolved in DMSO and at 6000 rpm/30 sec when dissolved in butylamine. After spin coating, the substrates were transferred on to the hot plates and annealed at 100 ^{O}C and 150 ^{O}C for DMSO and butylamine case respectively for 1 hour to form a perovskite-like rudorffite cubic 3D materials.

HTM deposition

8 wt % spiro-OMeTAD solution in chlorobenzene containing additives of lithium bis(trifluoromethanesulfonyl) imide and 4-*tert*-butylpyridine were spin coated on BiI_3 coated substrates at 3000 rpm/30 sec. The HTM coated substrates were kept overnight in air for oxidation of spiro-OMeTAD followed by thermal deposition of Au metal electrode to complete the cell. In case of devices with poly-3-hexyl thiophene (P3HT) as HTM (without dopants), 15mg/mL P3HT was dissolved in chlorobenzene followed by spin coating and annealing at 4000 rpm/30 sec and 70 ^{O}C/20 min respectively prior to deposition of Au counter electrode.

6.2.2 Characterization

Solar cell characteristics of all devices were measured using a Peccell Technologies PEC-L01 solar simulator with a Keithley 2400 source meter under 1 sun illumination (AM 1.5G, 100 mW/cm^2). The EQE spectra of the device were measured with Peccell Technologies, PEC-S20 action spectrum measurement setup. Optical, structural and morphological analysis were carried out using UV-vis spectrophotometer (UV-vis 1800, Shimazdu), X-ray diffractometer (D8 Discover, Bruker) with Cu Kα radiation source and scanning electron microscope (SU8000, HITACHI), respectively. The active areas of the cells were 0.09 cm^2.

6.3 Results and discussion

The present chapter is subdivided into two parts;

1. In the first part Studies on adverse effect of dopants used in spiro-OMeTAD and choice of suitable HTM for efficient Ag_3BiI_6 – rudorffite perovskite material based devices is presented.
2. Second part cover studies on choice of suitable precursor solvent for the dissolution of $AgBi_2I_7$ and Ag_2BiI_5 and its effect on photovoltaic performance.

6.3.1 First part: Studies on adverse effect of dopants used in spiro-OMeTAD and choice of suitable HTM for efficient Ag_3BiI_6 – rudorffite perovskite material based devices.

6.3.1.1 Ag_3BiI_6 thin film characterization

Ivan et al.[10] first reported Ag_3BiI_6 material based photovoltaic devices with device configuration of FTO/sputtered TiO_2/mesoporous TiO_2/Ag_3BiI_6/PTAA/Au which demonstrated the conversion efficiency of 4.3%. However, Banerwal et al. demonstrated poor reproducibility of Ag_3BiI_6 device performance both in normal (1.08%) and inverted architecture (0.32%) with spiro-OMeTAD and NiO as HTM respectively.[28] The exact reason for such non-reproducible and poor performance was attributed to non-homogeneous elemental distribution; as the amount of Bi^{3+} was smaller than the monovalent Ag^{+} cation.[28] However, further deep insights are necessary to understand the reason for degradation of PCE. Aim of the present study is to understand the morphology evolution of Ag_3BiI_6, role of dopants used in HTMs, developing dopant free HTMs and to enhance the performance.

Ag_3BiI_6 thin film was deposited by dissolving AgI and BiI_3 in DMSO followed by spin coating and annealing process (as mentioned in experimental section). Fig. 6.1.1 a shows optical microscopic image of Ag_3BiI_6 before spiro-OMeTAD deposition showing uniform and dense layer. Further, investigation to nanometer scale reveals non-uniform morphology of Ag_3BiI_6 with large number of pinholes are formed as shown in top surface SEM image (Fig. 6.1.2). Initially spiro-OMeTAD (with dopants) was employed as HTM and

during the spin coating process, slight change in the visible colour of Ag_3BiI_6 was observed. In order to understand the aforementioned issue, further optical microscopy was used to study the top surface morphology after spiro-OMeTAD deposition as the morphology cannot be seen clearly with SEM images due to low conductivity of spiro-OMeTAD. Surprisingly, deposition of spiro-OMeTAD (with dopants) shows adverse effect as the dense layer of Ag_3BiI_6 (Fig. 6.1.1 b) transforms into transparent one; that is Ag_3BiI_6 layer is being corroded. Also, further increasing the spiro-OMeTAD loading time, before spin coating step, results in complete corrosion of Ag_3BiI_6 layer (visible with naked eye). This indicates that the dopants used in spiro-OMeTAD may corrode the Ag_3BiI_6 layer. Hence, spiro-OMeTAD without dopants was deposited to verify the reason for degradation and as expected optical images shows (Fig. 6.1.1 c) no pinholes after depositing spiro-OMeTAD layer without dopants. This evidently signifies that dopants (Li-TFSI and/or TBP) are corroding the Ag_3BiI_6 layer leading to the transformation of dense layer to transparent one.

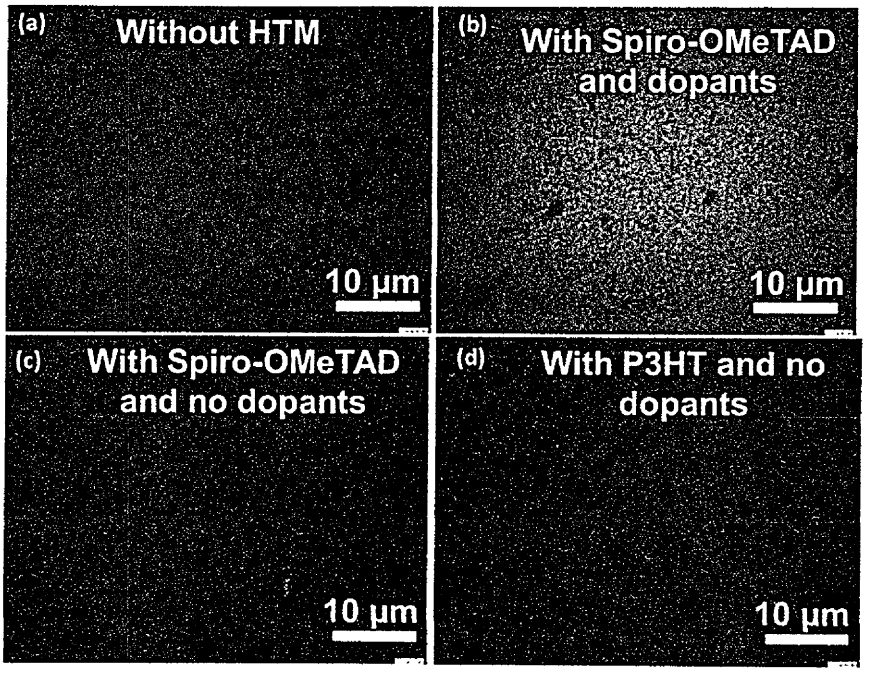

Figure 6.1.1: optical images of Ag_3BiI_6 thin film (a) without HTM, with spiro-OMeTAD as HTM (b) with dopants, (c) without dopants and (d) with P3HT HTM (without dopants).

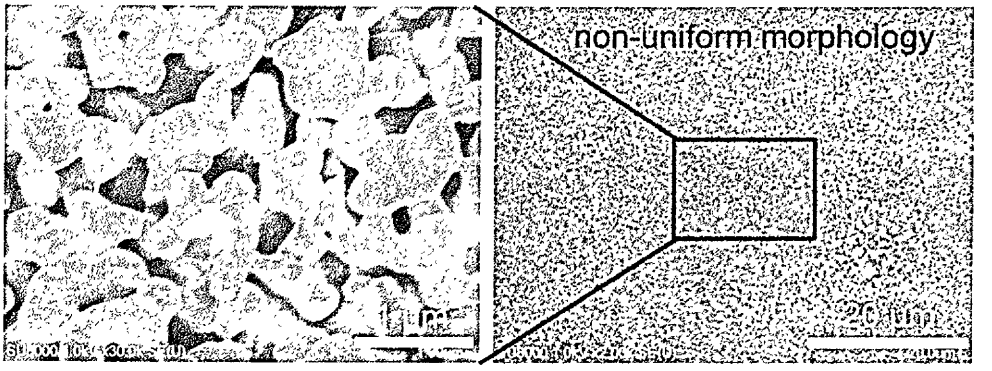

Figure 6.1.2: Top surface SEM image of Ag_3BiI_6 showing non-uniform morphology.

6.3.1.2 Photovoltaic characterization of Ag_3BiI_6

Devices were fabricated with spiro-OMeTAD with and without dopants. The performance of device with spiro-OMeTAD (with dopants) showed 1% efficiency (Fig. 6.1.3 a) in backward scan and shows hysteresis, additionally, its poor reproducibility, wider distribution of device performance (Fig. 6.1.3 b) can be attributed to the corrosion of Ag_3BiI_6 layer. Nevertheless, devices with spiro-OMeTAD (without dopants) showed very poor performance of ~0.3% (Fig. 6.1.3 c) and huge hysteresis along with unusual behavior in J-V characteristic curve (6.1.3 d) which can be attributed to poor conductivity of pristine spiro-OMeTAD layer (without dopants) and inefficient charge extraction.[29] In order to enhance the device performance, incorporation of HTMs having high conductivity is critically important. P3HT having high hole mobility previously has been employed in bulk heterojunction as well as in lead halide perovskite solar cells.[30,31] Herein, depositing P3HT layer without dopants didn't corrode the Ag_3BiI_6 layer as can be seen from Fig. 6.1.1 d and hence device fabrication was carried out with deposition of P3HT (without dopants) as HTM followed by thermal evaporation of Au. Cross-sectional SEM image of complete device (Fig. 6.1.4 a) reveals that around ~200 nm thick Ag_3BiI_6 layer is formed and a thin P3HT layer is visible. Also, many voids have been observed in Ag_3BiI_6 stacked layer (Fig. 6.1.4 a). Current density (J) - voltage (V) characteristic curve shows enhancement in short-circuit current (J_{sc}) leading to enhancement in conversion efficiency up to 1.6% in backward scan with high reproducibility as shown in histogram plot (Fig. 6.1.4 b, c) which can be due to better charge extraction via P3HT HTM contrasting spiro-OMeTAD (without and with dopants). Also, the device J-V characteristic curve shows hysteresis attributing to presence

of voids in Ag_3BiI_6. The low efficiency compared to previous report[10] can be due to the presence of voids and additionally Ivan et al.[10] employed PTAA as HTM which has better hole mobility than P3HT and can extract charge carriers effectively. Additionally, PTAA HOMO level matches well with Ag_3BiI_6.[10]

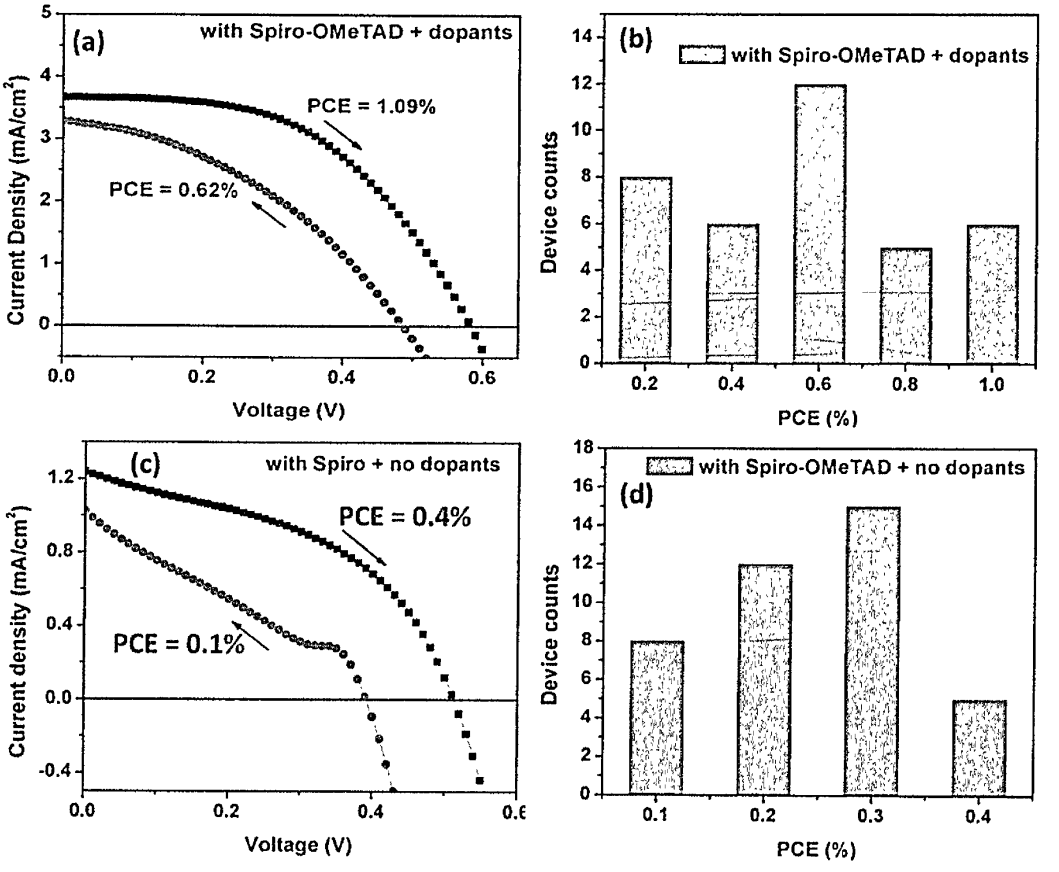

Figure 6.1.3: J-V characteristic curve of best performing Ag_3BiI_6 device with spiro-OMeTAD (a) with dopants, (b) its corresponding histogram plot, (c) without dopants and (d) its corresponding histogram plot.

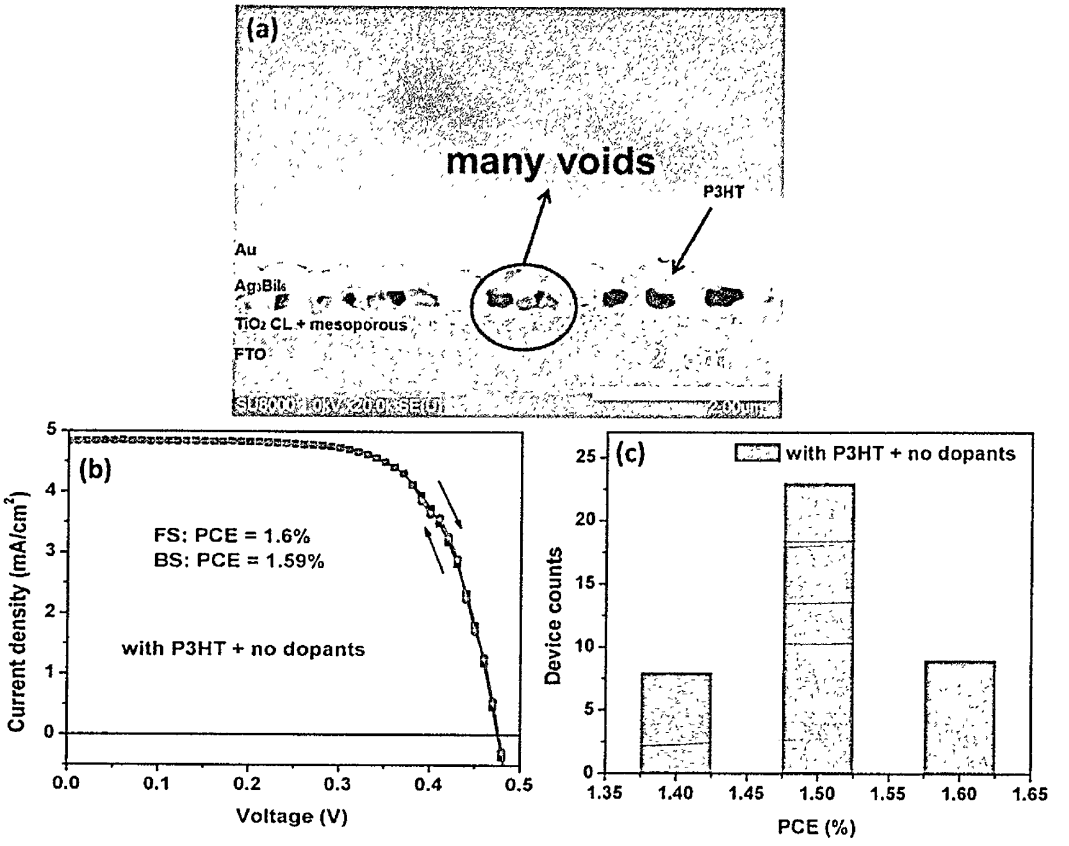

Figure 6.1.4: (a) Top surface SEM image of Ag_3BiI_6 device with P3HT without dopants as HTM, its corresponding (b) J-V characteristic curve (c) PCE histogram plot.

Further long term stability test was performed by exposing the devices to ambient atmosphere. From Fig. 6.1.5 it can be seen that the device performance is quite stable, however, with time the colour of metal electrode changes from yellow to yellowish green (Fig. 6.1.5 inset) resulting in degradation of performance. This change in colour can be due to the reaction of Au with AgI which is present as impurities at room temperature.

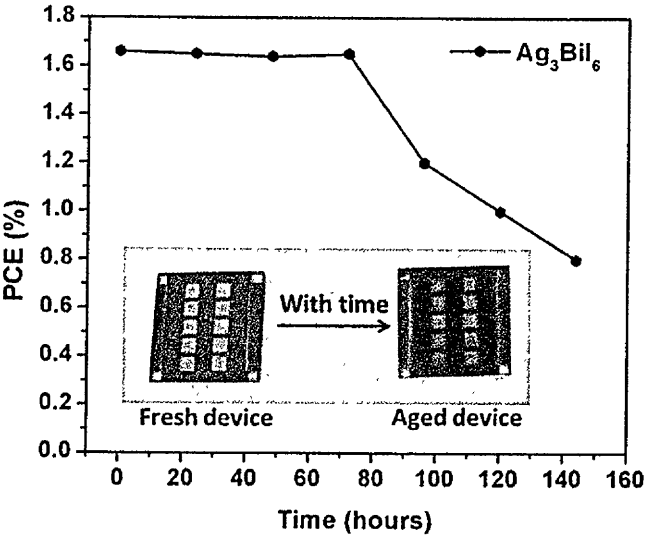

Figure 6.1.5: Long term performance stability test of Ag_3BiI_6 device with P3HT HTM layer.

Based on the obtained results, performance of Ag_3BiI_6 rudorffite perovskite like material can be improved by solvent engineering technique[32] to improve the morphology by mitigating the voids. Ag_3BiI_6 exist as a single phase only at elevated temperature and at room temperature lots of AgI impurities are present, hence, eliminating the impurities via low temperature solution route can further help to enhance the efficiency.[10] Also, suitable choice of HTM with deep HOMO level can help to enhance the V_{oc} and can be applied in tandem architecture. Ag_3BiI_6 material bandgap of 1.79 eV corresponds to photoconversion efficiency of 18% by assuming V_{oc} of 1.2 V and typical assumptions about optical losses and fill factor for optimized solar cells. The degradation of device performance also suggests that interfacial modification and/or change in metal electrode or architecture can further enhance device performance and retain its long term stability.[33]

6.3.2 Second part: Studies on effect of precursor solvent on the photovoltaic performance of $AgBi_2I_7$ and Ag_2BiI_5.

6.3.2.1 Thin film characterization of $AgBi_2I_7$ and Ag_2BiI_5.

Kim et al. fabricated photovoltaic device with $AgBi_2I_7$ as an active layer and reported champion PCE of 1.2%.[26] However, Johansson et al. reported non-reproducibility in the device performance of $AgBi_2I_7$ with 0.4% PCE and further demonstrated Ag_2BiI_5

based solar cells with 2.1% PCE.[25] Previously, Kim et al. dissolved Ag-Bi-I in butylamine as AgI is not soluble in polar aprotic solvents such as DMF and/or DMSO which are commonly used solvents to dissolve BiI_3 and lead halide perovskites.[26] Even though AgI is not soluble independently in DMSO, here in this study, it was found that the mixture of AgI and BiI_3 readily gets dissolve in DMSO with stirring at 80 ^{O}C for 1 hour. DMSO is a well-known two-electron donor (Lewis base) ligand and BiI_3 is reported to form adducts or coordination complex with range of Lewis base ligands.[22] The dissolution of AgI and BiI_3 in DMSO indicates that the formed BiI_3-DMSO complex[10] or $[BiI_{3+x}]^{x-}$ complex ions can dissolve AgI (as AgI is not independently soluble in DMSO) resulting in complete dissolution. The Ag-Bi-I material is sandwiched between TiO_2 mesoporous electron transporting layer (ETL) and poly(3-hexylthiophene-2,5-diyl) (P3HT) (without dopants) hole transporting layer (HTL) due to observed beneficial effect (as discussed in part 1). The best device show PCE of ~1.7% under 100 mW/cm^2, AM 1.5 G solar illumination. Additionally, the results were compared with Ag-Bi-I compound dissolved in butylamine and also with recently reported Ag_2BiI_5 (dissolved in both butylamine and DMSO). X-ray diffraction (XRD), UV-vis spectra, photoluminescence (PL), scanning electron microscope (SEM) were used to compare (two different Ag-Bi halide materials) and investigate their properties.

Herein it is observed that BiI_3 and AgI (independently as well as 20 wt.% mixtures) are soluble in butylamine at room temperature whereas only BiI_3 is soluble in DMSO at room temperature and AgI gets dissolve into the DMSO-BiI_3 solution only after increasing the solution temperature to 80 ^{O}C with constant stirring. After spin coating the Ag-Bi-I solution and heating, the substrate visual colour of Ag-Bi-I obtained from butylamine and DMSO route appears dark grayish black and dark brown in colour respectively as shown in Figure 6.2.1 a. Even though butylamine has low boiling point (70 ^{O}C), heating at 150 ^{O}C leads to its complete removal from the spin coated film.[26] This is because butylamine forms strong complex with both BiI_3 and AgI and annealing at high temperature (150 ^{O}C) only can lead to complete cleavage of the intermediate complexes.[26] On the other hand, the decomposition of Bi-Ag-I-DMSO complex occurs as low temperature in comparison to butylamine case as the colour of the substrate transitioned from yellow to dark brown colour after heating at 100 ^{O}C. This infers that DMSO-BiI_3 coordinated complex is not strong as

compared to butylamine-BiI_3 one. It is also suspected that interaction of AgI with BiI_3-DMSO complex (as it gets dissolve) weakens the DMSO-BiI_3 interaction. Form this it can infer that crystallization process of $AgBi_2I_7$ thin film through butylamine route differs from that of DMSO one. The disparity in solvent evaporation and annealing temperature in addition to different crystallization route can cause variation in grain size and thus change in the visual colour of the substrates. More details about the grain size will be discussed later. The crystal structure of $AgBi_2I_7$ thin film obtained from 20 wt.% solution were analyzed by XRD and the results are shown in Figure 6.2.1 b. The diffraction pattern of Ag-Bi-I (obtained from butylamine) on mesoporous TiO_2/FTO substrate exhibits major characteristic peaks of 2θ reflection at 12^O, 25^O, 29^O, 42^O corresponding to (111), (311), (400) and (440) orientation respectively.[26] XRD pattern obtained from DMSO route also shows same characteristic peaks except at $2\theta = 42^O$ where less intense doublet peak appears. As the doublet peak intensity (at $2\theta = 42^O$) is week, in order to enhance the intensity, XRD pattern of 40 wt.% $AgBi_2I_7$ (dissolved in DMSO) was measured and interestingly singlet peak (along with doublet with very less intensity) at $2\theta = 42^O$ is seen which contrasts with XRD pattern measured for 20 wt.% as shown in Fig. 6.2.1 e. Further increasing the concentration to 60 wt.% lead to complete disappearance of doublet peak and high intense peak corresponding to (440) appears.

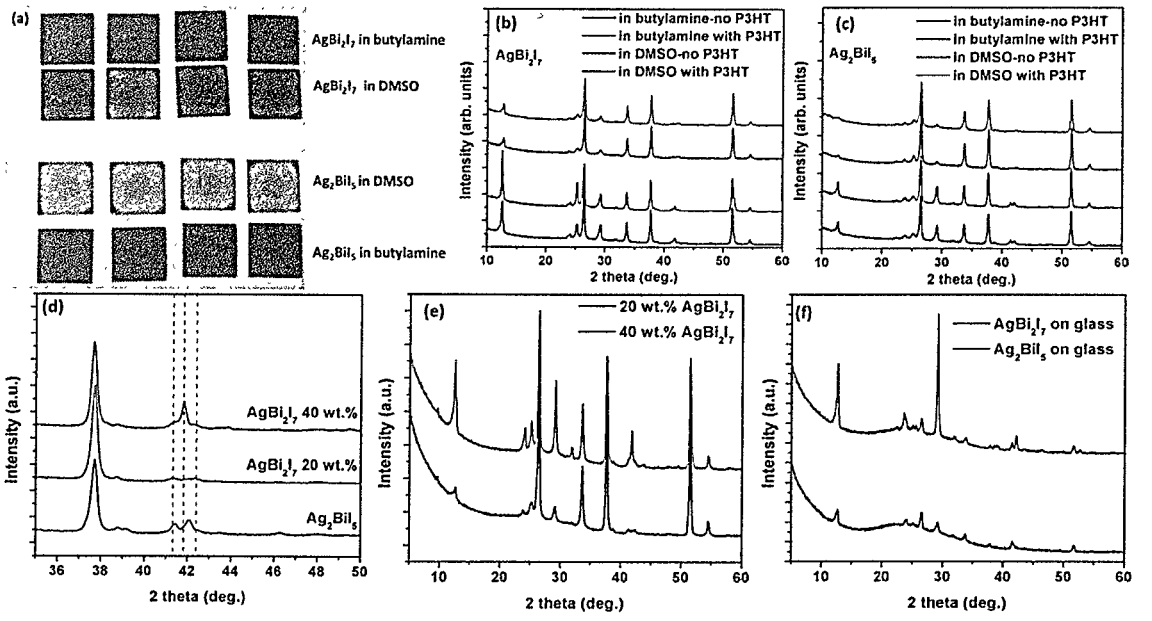

Figure 6.2.1: (a) Visual image of silver-bismuth halide materials, corresponding XRD pattern of (b) $AgBi_2I_7$ and (c) Ag_2BiI_5, comparing XRD pattern of (d) $AgBi_2I_7$ and Ag_2BiI_5 at 2 theta = 42^O, (e) 20 and 40 wt.% $AgBi_2I_7$ and (f) $AgBi_2I_7$ and Ag_2BiI_5 on glass.

There can be two possibilities for the formation of doublet peak of $AgBi_2I_7$ (for 20 wt.%) on TiO_2/FTO substrates: 1) formation of some other composition or 2) formation of some other phase. Very recently Zhu *et al.* reported doublet peak for Ag_2BiI_5 at $2\theta = 42^O$ corresponding to (108) and (113) orientation.[25] Hence in order to verify this, diffraction pattern of Ag_2BiI_5 was measured by dissolving AgI and BiI_3 in 2:1 molar ratio in butylamine and DMSO and compared it with $AgBi_2I_7$. From Fig. 6.2.1 c it can be seen that Ag_2BiI_5 dissolved either in butylamine or DMSO shows doublet peak at $2\theta = 42^O$ which are strikingly different from that of Ag-Bi-I as there is a slight shift in doublet peak (Fig. 6.2.1 d) of $AgBi_2I_7$ with that of Ag_2BiI_5. This significantly evidences that Ag_2BiI_5 is not formed when AgI and BiI_3 (in 1:2 molar ratio) are dissolved in DMSO. Further to study the presence of some other phase we deposited 20wt.% solution of $AgBi_2I_7$ on glass substrate and very surprisingly the XRD pattern shows single peak at $2\theta = 42^O$ corresponding to (440) orientation (Fig. 6.2.1 f). This further suggests that the mesoporous under layer is affecting the crystallization of 20 wt.% $AgBi_2I_7$ (obtained from DMSO route) when deposited on TiO_2/FTO coated substrates resulting in the formation of different phase. For the present state the exact reason for the appearance of doublet peak is not clear but it is suspected that

$AgBi_2I_7$ coexist in two different phase which can be distinguishable when lower wt.% with appropriate solvent such as DMSO, which do not form strong complex, is used. Also it is suspected that distinguishing such behaviour in butylamine case (with 20 wt.%) is difficult as it forms strong coordinated complex with both BiI_3 and AgI resulting in thicker film or large grains.

Previously Zhu et al. observed decrease in peak intensity of $AgBi_2I_7$ and Ag_2BiI_5 XRD pattern after exposing them to ambient atmosphere.[25] They also observed that upper P3HT layer protects it from degradation and attributed this degradation behaviour due to the effect of moisture. In this study the XRD pattern of $AgBi_2I_7$ (obtained from butylamine) shows same behaviour (Fig. 6.2.1 b), that is, shows higher peak intensity with P3HT upper layer contrasting without P3HT layer case. Interestingly, no change in peak intensity of 20 wt.% $AgBi_2I_7$ thin film with and without P3HT layer when routed through DMSO is observed as shown in Fig. 6.2.1 b. It is well known that BiI_3 and AgI are not soluble in water and the complex $AgBi_2I_7$ does not contain any hygroscopic organic component which can be sensitive to moisture. Thus it is infer that the degradation of $AgBi_2I_7$ when dissolved in butylamine is not due to exposure to moisture. From this it is suspected that the stability of $AgBi_2I_7$ is highly dependent on crystallization process and its root lies in the choice of precursor solvent. Also, prior report suggests that there are lots of vacancies in the $AgBi_2I_7$ compound[10] and these vacancies might not be present in different phase of $AgBi_2I_7$ observed on FTO/TiO_2 substrate. These vacancies can also be the reason for degradation and the formation route may minimize these vacancies leading to stabilization of the compound.

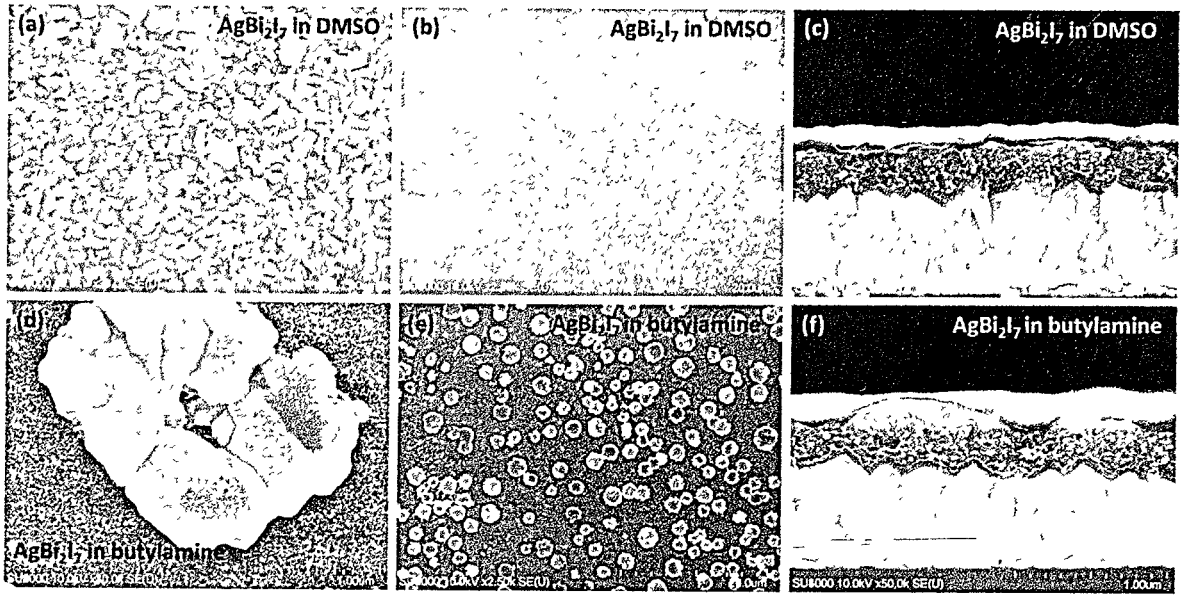

Figure 6.2.2: Top surface and cross-sectional SEM image of $AgBi_2I_7$ obtained from (a, b, c) DMSO and (d, e, f) butylamine

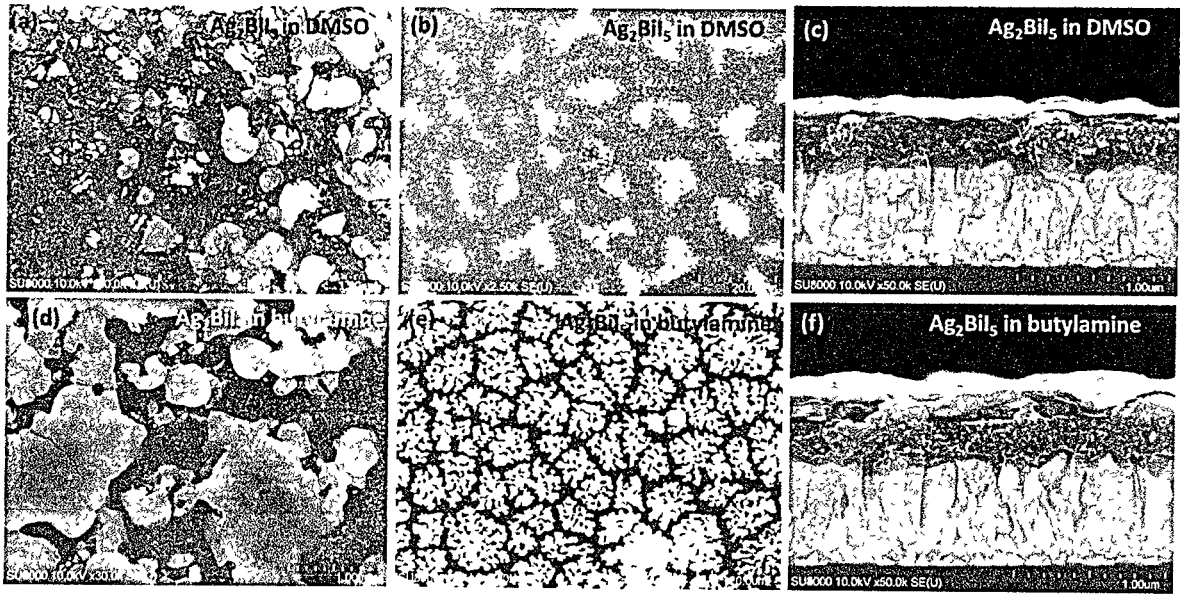

Figure 6.2.3: Top surface and cross-sectional SEM image of Ag_2BiI_5 obtained from (a, b, c) DMSO and (d, e, f) butylamine

Top surface scanning electron micrograph (SEM) was used to study the morphology of $AgBi_2I_7$ and Ag_2BiI_5 routed from DMSO and butylamine. From Fig. 6.2.2 a, it can be seen that $AgBi_2I_7$ routed from DMSO forms uniform grains however this uniformity is not

seen all over the substrate as shown in Fig. 6.2.2 b. On a contrary, $AgBi_2I_7$ routed from butylamine showed very large independent grains with large number of uncovered areas as can be seen from Fig. 6.2.2 d, e. These large grains and tuned morphology routed from different solvents is responsible for variation in visual colour of $AgBi_2I_7$ deposited on FTO/TiO_2 substrates. Fig. 6.2.2 c shows that $AgBi_2I_7$ routed from DMSO didn't show sufficient capping layer atop of TiO_2 mesoporous layer, however $AgBi_2I_7$ routed from butylamine shows large grains with large number of gaps through which the HTM (P3HT) and metal electrode (Au) is directly connecting porous TiO_2 layer. On the other hand, Ag_2BiI_5 thin film (Fig. 6.2.3 b, e) obtained from DMSO or butylamine shows shiny grains and with exposure of electron beam the shiny layer disappears and dark grains are seen as shown in Fig. 6.2.3 a, d. However, in both the cases (DMSO and butylamine), Ag_2BiI_5 shows poor coverage a top of mesoporous TiO_2 (Fig. 6.2.3 c, f) and is different from $AgBi_2I_7$ obtained from DMSO. Moreover, the grain size of Ag_2BiI_5 obtained from butylamine route is larger than DMSO (Fig. 6.2.3 a, d) and is the reason for difference in visible colour as seen in Fig. 6.1.1 a.

6.3.2.2 Photovoltaic characterization and long-term stability test

Devices were fabricated with $AgBi_2I_7$ and Ag_2BiI_5 as active layers in between mesoporous TiO_2 and P3HT layers as shown in the schematic representation (Fig. 6.2.4 d). From current density-voltage (J-V) curve (Fig. 6.2.4 a) of best performing devices it can be seen that $AgBi_2I_7$ showed better performance when routed from DMSO contrasting butylamine case. Even though, in case of $AgBi_2I_7$ dissolved in DMSO, a smooth uniform capping layer is not seen it is loaded completely in porous TiO_2 as can be seen from cross sectional view and better interfacial connection with P3HT lead to improved conversion efficiency up to 1.65% with high reproducibility (Fig. 6.2.4 c) whereas in case of butylamine large grains with improper interfacial connection leads to reduction in efficiency. The reason for high efficiency (for DMSO route) and low efficiency (for butylamine route) can also be due to the different phase of $AgBi_2I_7$ and sensitivity of $AgBi_2I_7$ (as it gets degrade) respectively. On the other hand, Ag_2BiI_5 showed improved conversion efficiency when dissolved in butylamine in comparison to DMSO route (Fig. 6.2.4 b, c). This can be due to high crystalline peaks and observed grains of Ag_2BiI_5 when dissolved in butylamine

whereas Ag_2BiI_5 film obtained from DMSO route shows poor intense peaks as well as the grains are not visible. Additionally among all the cases $AgBi_2I_7$ thin film obtained from DMSO showed null hysteresis owing to better interfacial connections and efficient charge extraction as can be seen in Fig. 6.2.4 c

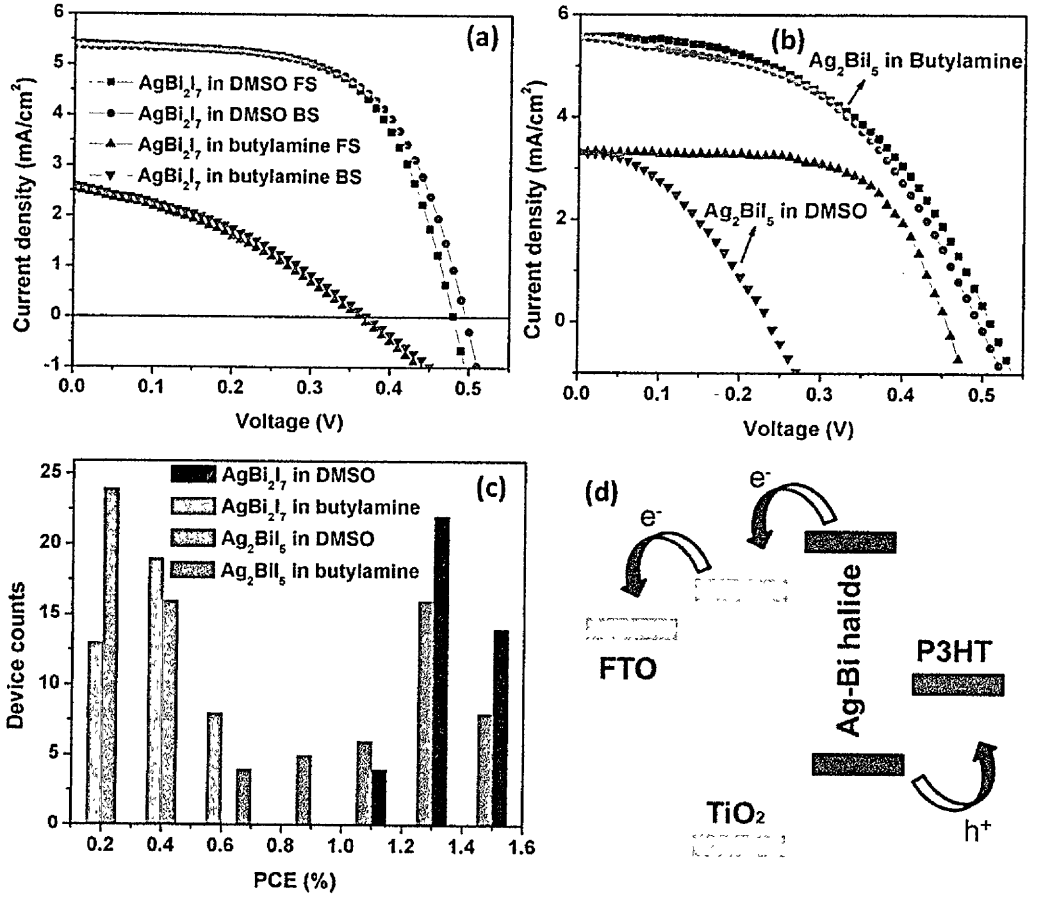

Figure 6.2.4: J-V characteristics of best performing devices incorporating (a) $AgBi_2I_7$, (b) Ag_2BiI_5 obtained from DMSO and butylamine, (c) their corresponding PCE histogram plot and (d) schematic illustration of complete device architecture.

Long term stability test was performed by exposing the devices to ambient atmosphere (relative humidity of 50%) and the efficiency was recorded with time. Fig. 6.2.5 shows that $AgBi_2I_7$ (routed from DMSO) devices shows high stability up to 360 hours compared to all other cases. The reduction in efficiency for $AgBi_2I_7$ (butylamine case) and Ag_2BiI_5 (DMSO and butylamine) can be due to its sensitivity when exposed to moisture.

Unlike Ag_3BiI_6, $AgBi_2I_7$ does not possess AgI impurities and exist as a single phase at room temperature[10] because of which no change in colour of Au is observed, hence better stability.

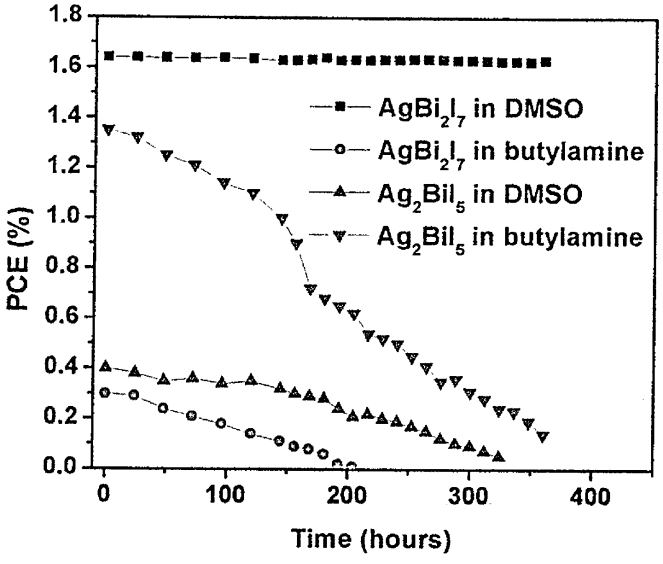

Figure 6.2.5: Long term stability test of best performing devices of all the cases studied.

Based on the obtained results, it can be infer that precursor solvent plays an important role in enhancing the efficiency, stability of silver bismuth halide materials. The conversion efficiency can be further improved by increasing the grain size and by obtaining a uniform capping layer which can be achieved by solvent engineering process. Additionally, identifying the different phase with the effect of TiO_2 porous layer in $AgBi_2I_7$ can further help to get deep insight in enhancing the PCE. The present study demonstrates initial efficiency of 1.7% for $AgBi_2I_7$ devices and here the device shows 0.48 V which is quite less with the bandgap of 1.8 eV further suggesting huge room for improvement of non-toxic $AgBi_2I_7$ materials for eco-friendly photovoltaic devices.

6.4 Conclusion

Part 1

Ag_3BiI_6 rudorffite perovskite material thin film showed lots of pinholes and poor morphology. Dopants added in spiro-OMeTAD corrode the Ag_3BiI_6 layer and pristine spiro-OMeTAD based device shows poor device performance due to poor conductivity. Employing P3HT (without dopants) as HTM improves the performance mainly due to enhancement in short-circuit current (J_{sc}). Cross-sectional SEM images shows presence of voids which also impedes the device performance. Improving the morphology by eliminating the voids and low temperature solution deposition process can further pave path towards enhancing the efficiency. In addition to it, interface engineering and/or different device architecture can also further enhance the stability along with long term stability of non-toxic three dimensional iodobismuthate perovskite-like materials.

Part 2

$AgBi_2I_7$ cubic perovskite like materials show change in orientation when obtained from DMSO and butylamine route. Further XRD pattern of $AgBi_2I_7$ is strikingly different from that of Ag2BiI5, further revealing a different phase of $AgBi_2I_7$ material exist at lower concentration, when dissolved in DMSO. Also, the XRD peak intensity of $AgBi_2I_7$ didn't show any change even without P3HT upper layer contrasting other cases. The morphology of $AgBi_2I_7$ and Ag2BiI5 obtained from DMSO and butylamine route shows variation and among all $AgBi_2I_7$ obtained from DMSO route shows better morphology at some places. Photovoltaic performance reveals $AgBi_2I_7$ from DMSO improved Jsc of the cell and over PCE up to 1.65% contrasting all the other cases which demonstrated poor conversion efficiency (<1%). Also, $AgBi_2I_7$ demonstrates long term stability against exposure to ambient atmosphere (relative humidity of ~50%) in comparison to other cases studied. Present study signifies the role of solvent in tuning morphology, PCE enhancement and stability of non-toxic silver-bismuth halide perovskite-like materials.

6.5 References

1 Kojima, A.; Teshima, K.; Miyasaka, T.; Shirai, Y., *Proc. 210th ECS Meeting*, **2006**, 397.

2 Kojima, A.; Teshima, K.; Shirai, Y.; Miyasaka, T., *J. Am. Chem. Soc.* **2009**, *131*, 6050-6051.

3 Best solar cell efficiency chart. Available at http://www.nrel.gov/ncpv/images/efficiency_chart.jpg accessed on (9th Dec. 2017).

4 S. D. Stranks, G. E. Eperon, G. Grancini, C. Menelaou, M. J. P Alcocer, T. Leijtens, L. M. Herz, A. Petrozza and H. J. Snaith, *Science*, **2013**, *342*, 341.

5 G. C. Xing, N. Mathews, S. Y. Sun, S.S. Lim, Y. M. Lam, M. Grätzel, S. Mhaisalkar and T.C. Sum, *Science*, **2013**, *342*, 344.

6 Pazos-Outon, A. M.; Szumilo, M.; Lamboll, R.; Richter, J. M.; Crespo-Quesada, M.; Abdi-Jalebi, M.; Beeson, H. J.; Vrucinic, M.; Alsari, M.; Snaith, H. J.; Ehrler, B.; Friend, R. H.; Deschler, F., *Science*, **2016**, *351 (6280)*, 1430-1433.

7 S. Y Sun, T.Salim, N. Mathews, M. Duchamp, C. Boothroyd, G. C. Xing, T. C. Sum and Y. M. Lam, *Energ. Environ. Sci*, **2014**, *7*, 399.

8 Legitens, T.; Bush, K.; Cheacharoen, R.; Beal, R.; Bowring, A.; McGehee, M. D., *J. Mater. Chem. A*, **2017**, *5*, 11483-11500.

9 Kadro, J., M.; Hagfeldt, A., *Joule*, **2017**, *1*, 29-46.

10 Turkevych, I.; Kazaoui, S.; Ito, E.; Urano, T.; Yamada, K.; Tomiyasu, H.; Yamagishi, H.; Kondo, M.; Aramaki, S., *ChemSusChem*, **2017**, DOI: 10.1002/cssc.201700980

11 Babayigit, A.; Ethirajan, A.; Muller, M.; Conings, B., *Nature Materials*, **2016**, *15*, 247-251.

12 Saliba, M.; Matsui, T.; Seo, J-Y.; Domanski, K.; Correa-Baena, J-P.; Nazeeruddin, M. K.; Zakeeruddin, S. M.; Tress, W.; Abate, A.; Hagfeldt, A.; Gratzel, M., ***Energy Environ. Sci.***, **2016**, *9*, 1989-1997.

13 Chaudhary, B.; Kulkarni, A.; Jena, A. J.; Ikegami, M.; Udagawa, Y.; Kunugita, H.; Ema, K.; Miyasaka, T., *ChemSusChem*, **2017**, DOI: 10.1002/cssc.201700271.

14 Binek, A.; Petrus, M. L.; Hyber, N.; Bristow, H.; Hu, Y.; Bein, T.; Docampo, P., *ACS Appl. Mater. Interfaces*, **2016**, *8* (20), pp 12881–12886.

15 Niu, G.; Li, W.; Li, J.; Liang, X.; Wang, L., *RSC Adv.*, **2017**, *7*, 17473-17479

16 Konstantakou, M.; Stergiopoulous, T., *J. Mater. Chem. A*, **2017**, *5*, 11518-11549.

17 Krishnamoorthy, T.; Ding, H.; Yan, C.; Leong, W. L.; Baikie, T.; Zhang, Z.; Sherburne, M.; Li, S.; Asta, M.; Mathews, N.; Mhaisalkar, S. G., *J. Mater. Chem. A*, **2015**, *3*, 23839-23832.

18 M. Lyu, J-H. Yun, M. Cai, Y. Jiao, P. V. Bernhardt, M. Zhang, Q. Wang, A. Du, H. Wang, G. Liu and L. Wang, *Nano Res.*, DOI: 10.1007/s12274-015-0948-y.

19 Kulkarni, A.; Singh, T.; Ikegami, M.; Miyasaka, T., *RSC Adv.*, **2017**, *7*, 9456-9460.

20 Park, B.-W.; Philippe, B.; Zhang, X.; Ransmo, H.; Boschloo, G.; Johansson, E. M. J., *Adv. Mater.*, **2015**, *27*, 6806-6813.

21 Zhang, Z.; Li, X.; Xia, X.; Wang, Z.; Huang, Z.; Lei, B.; Gao, Y., *J. Phys. Chem. Lett.*, **2017**, *8 (17)*, 4300-4307.

22 Hamdeh, U. M.; Nelson, R. D.; Ryan, B. J.; Bhattacharjee, U.; Petrich, J. W.; Panthani, M. G., *Chem. Mater.*, **2016**, *28 (18)*, 6567-6574.

23 Slavney, A. H.; Hu, T.; Lindenberg, A. M.; Karunadasa, H. I., *J. Am. Chem. Soc.*, **2016**, *138 (7)*, 2138-2141.

24 Savory, C. N.; Walsh, A.; Scanlon, D. O., *ACS Energy Lett.*, **2016**, *1 (5)*, 949-955.

25 Zhu, H.; Pan, M.; Johansson, M., B.; Johansson, E., M. J., *ChemSusChem*, **2017**, *10*, 2592– 2596

26 Kim, Y.; Yang, Z.; Jain, A.; Voznyy, O.; Kim, G.-H.; Liu, M.; Quan, L., N.; Arquer, A., P., G.; Comin, R.; Fan, J., Z.; Sargent, E., H., *Angew. Chem.*, **2016**, *128*, 1-6.

27 Xiao, Z.; Meng, W.; Mitzi, D., B.; Yan, Y., *J. Phys. Chem. Lett.*, **2016**, *7* (19), 3903–3907

28 Baranwal, A., K.; Masutani, H.; Sugito, H.; Kanda, H.; Kanaya, S.; Shibayama, N.; Sanehira, Y.; Ikegami, M.; Numata, Y.; Yamada, K.; Miyasaka, T.; Umeyama, T.; Imahori, H.; Ito, S., *Nano Converg.*, **2017**, *4(1)*, 26.

29 Bach, U.; Lupo, D.; Comte, P.; Moser, J., E.; Weissörtel, F.; Salbeck, J.; Spreitzer, H.; Graetzel, M., *Nature*, **1998**, *395*, 583-585.

30 Winands, T.; Boeckmann, M.; Schemme, T.; Ly, P.-M., T.; Jong, D., H.; Wang, Z.; Denz, C.; Heuer, A.; Doltsinis, N., L., *Phys. Chem. Chem. Phys.*, **2016**, *18*, 6217-6227.

31 Zhang, Y.; Elawas, M.; Yu, Z.; Jiang, X.; Lai, J.; Sun, L., *RSC Adv.*, **2016**, *6*, 108888-108895

32 Shi, Y.; Wang, X.; Zhang, H.; Li, B.; Lu, H.; Ma, T.; Hao, C., *J. Mater. Chem. A*, **2015**, *3*, 22191-22198.

33 Domanski, K.; Correa-Baena, J.-P.; Mine, N.; Nazeeruddin, M. K.; Abate, A.; Saliba, M.; Tress, W.; Hagfeldt, A.; Gratzel, M., *ACS Nano*, **2016**, *10* (6), 6306–6314.

Chapter 7

Future Scope

7.1 Lead Perovskite Materials

Organic-inorganic lead halide perovskite solar cells have demonstrated certified 22.7% power conversion efficiency (PCE). Short-circuit current (J_{sc}) and fill factor (FF) has already reached saturation limit in accordance with the band gap of the material (~1.6 eV). However, to date open-circuit voltage (V_{oc}) of ~1.2 V has been achieved and there is a room for efficiency enhancement by increasing the V_{oc}. As discussed in chapter 2 and also in accordance to prior reports, presence of TiO_2 electron transport layer (ETL) helps in enhancing J_{sc} and FF, however, it does not essentially help to enhance V_{oc} and devices without TiO_2 ETL demonstrated high V_{oc} up to ~1.1 eV. The results obtained in chapter 2 revealed that TiO_2 ETL based perovskite solar cells undergoes trap assisted recombination at TiO_2/FTO interface which can be the reason for limitations for V_{oc} which can be further enhanced by:

1. Modification of FTO/TiO_2 interface by incorporating UV-resistive materials, and/or thin insulating materials.
2. FTO/TiO_2 interfacial modification can also enhance perovskite device stability against UV-light.
3. Developing novel non-UV sensitive inorganic and organic ETLs.
4. Developing novel conductive electrodes based on organic molecules.

The above mentioned directions can further help to enhance the V_{oc} of the device and concomitantly enhancement in conversion efficiency and long-term stability of perovskite solar cells.

7.2 Lead-free Materials

7.2.1 Bismuth Perovskite

Methylammonium iodobismuthate (MIB) – a zero dimensional bismuth perovskite material demonstrated exceptional long-term stability against moisture, however, their poor efficiency (less than 1%) was credited to poor morphology, high intrinsic carrier densities, low charge carrier mobility and high exciton binding energy. The results obtained in chapter 3 and 4 revealed that MIB ($(CH_3NH_3)_3Bi_2I_9$) thin film morphology is highly sensitive to the nature of ETL. Additionally, tuning the morphology of $(CH_3NH_3)_3Bi_2I_9$, by slowing down the rate of crystallization, does not effectively improve the conversion efficiency. Further PCE of $((CH_3NH_3)_3Bi_2I_9$ can be enhanced by

1. Tuning the intrinsic optoelectronic properties by doping, for instance with sulfur, which can reduce the bandgap and enhance the charge carrier mobility.
2. Employing novel organic/inorganic cations to increase the dimensionality of the material such as use of bulky [py][BiI_4] moieties (py = pyridine).
3. Exploring alternate ETL and hole transporting layer (HTL).

7.2.2 Non-perovskite Bismuth Iodide

In addition to suitable band gap of ~1.78 eV, bismuth iodide (BiI_3) possess exceptional optoelectronic properties suitable for photovoltaic applications. To date, planar structured device of BiI_3 material demonstrated 1% efficiency with inorganic HTL. Chapter 5 results reveal that BiI_3 materials are also quite suitable for mesostructured architecture, however, the morphology and crystal orientation of BiI_3 is highly sensitive to annealing temperature. The results of chapter 5 demonstrated 0.5% efficiency in TiO_2 mesostructured configuration with organic HTL (spiro-OMeTAD). Conversion efficiency of BiI_3 material based device can be further improved by

1. Eliminating the pinholes and improving the grain size by solvent engineering and/or vapour deposition technique.
2. Incorporating alternate ETL such as SnO_2, ZnO, to extract photo-generated carriers effectively at BiI_3/ETL interface.
3. Incorporating novel HTL having low lying HOMO level for well matching with HOMO of BiI_3 and for efficient charge extraction and transportation.

7.2.3 Silver-bismuth Halide – Perovskite like materials

Three dimensional materials show superior optoelectronic properties compared to lower dimensional one owing to lower exciton binding energy and high charge carrier mobility. Silver-bismuth halide (Ag-Bi-I) materials possess three dimensional cubic structures with edge sharing octahedra. Chapter 6 presents results of various Ag-Bi-I materials such as Ag_3BiI_6, Ag_2BiI_5 and $AgBi_2I_7$ perovskite-like materials.

Part 1: Ag_3BiI_6 material corrodes in the presence of dopants (TBP and Li-TFSI) that are used in spiro-OMeTAD and device with P3HT (high hole mobility HTL) demonstrated 1.6% efficiency. Also, many voids were observed in the bulk of Ag_3BiI_6 layers which limit its PCE. Additionally, metal electrode (Au) layer changes with time due to the possible reaction of free AgI with Au.

Part 2: $AgBi_2I_7$ and Ag_2BiI_5 showed variation in the morphology with the change in the precursor solvent. At lower wt. %, a secondary phase of $AgBi_2I_7$ (deposited on TiO_2 mesoporous layer) was observed in XRD pattern. Devices with $AgBi_2I_7$ in DMSO showed best PCE of 1.65% compared to other studied materials. Also, the stability of $AgBi_2I_7$ and Ag_2BiI_5 is highly dependent on the precursor solvent used.

The efficiency and stability of silver-bismuth halide materials can be improved by

1. Eliminating the voids and enhancing the grain size of Ag_3BiI_6 by solvent engineering protocols.
2. Eliminating the free AgI impurities by developing low temperature solution method.
3. Interfacial modification of Ag_3BiI_6 and HTM or Au to avoid corrosion of metal electrode (OR) exploring alternate device architecture based on carbon counter electrode.
4. Improving the morphology of $AgBi_2I_7$ and Ag_2BiI_5 by choice of appropriate solvents.
5. Identify the secondary phase of $AgBi_2I_7$ in the presence of mesoporous TiO_2.
6. Developing HTM with high hole mobility and with well matching energy level.

Acknowledgements

First and foremost, I would like to thank my supervisor, Prof. Tsutomu Miyasaka, for giving me the opportunity to work on perovskites during their golden-era, and more importantly, allowing me boundless freedom in my research. His sheer excitement and enthusiasm for science has been a constant source of inspiration, and I couldn't hope for a better example. It's been a great honour to be part of his research team.

I would like to thank all the other Prof. Miyasaka's lab members, both current and past, for making life in lab not just productive but also a lot of fun. It's been great to work with you all. Special thanks go to Prof. Masashi Ikegami, Dr. Ajay K. Jena, Dr. Trilok Singh and Mr. Peerathat Pinpithak for their constant support and valuable discussion over the time period of my stay.

I would like to thank all my friends, in particular, Ankit Rupda, Arti Rupda, Dr. Hema Bora Bhandari, Dr. Trupti Bahera Jena, Pooja Makwana, Dr. Himadri Pathak, and for all the tasty food, constant support, travelling partner, and generally being a great household. A further special thanks to Miss Bhumika Chaudhary (*Kuchi Puchi*) and Usha Chaudhary for being a part of my special Japan journey.

I specially acknowledge my parents (*Pappa, Aai)*, Abhishek Kulkarni (*Anna*), Arun Kulkarni (*Chacha)*, Arti Kulkarni (Chachi), Anil Deshpande (Kaka), Sunanda Deshpande (Maushi), Chaitanya Deshpande (dada), Nikita Kulkarni (Rani), Namratha Kulkarni (Chinni), Vedanth Deshpande (Vedu), Vaishnavi Deshpande (Chinni), and last but not the least Sushila Deshpande (*aaji*), late. Suresh Deshpande (*ajoba*), and late. Indumati Kulkarni (*aaji*), and late. Sudhakar Kulkarni (*ajoba*) for their love, constant affection and blessings.

I would like to thank all my teachers from primary school till my master's degree for imbibing good values and knowledge in me.

Lasts but by no means least I thank Tuljabhawani Aai (*Kuladevi*), Venkataramana Govinda (*Kuladevta*), Guru mauli (*ajoba*) for making my life so special.

Finally, I dedicate my thesis to Anil Kulkarni (*Pappa*), Padmaja Kulkarni (*Aai*) and Abhishek Kulkarni (*Anna*).

List of Publications

In First Author (related to thesis)

1. **A. Kulkarni**, A. K. Jena, H.-W. Chen, Y. Sanehira, M. Ikegami, T. Miyasaka, Revealing and Reducing the Possible Recombination Loss within TiO_2 compact layer by incorporating MgO layer in Perovskite Solar Cells, *Solar Energy*, **2016**, *136*, 379-384.
2. T, Singh, **A. Kulkarni**, M. Ikegami, T. Miyasaka, Effect of Electron Transporting Layer on Bismuth-Based Lead-Free Perovskite $(CH_3NH_3)_3Bi_2I_9$ for Photovoltaic Applications, *ACS Appl. Mater. Interfaces*, **2016**, *8 (23)*, 14542–14547. **(TS and AK contributed equally).**
3. **A. Kulkarni**, T. Singh, M. Ikegami, T. Miyasaka, Photovoltaic enhancement of bismuth halide hybrid perovskite by N-methyl pyrrolidone-assisted morphology conversion, *RSC Adv.*, **2017**, 7, 9456.
4. **A. Kulkarni**, M. Ikegami, T. Miyasaka, Morphology evolution of non-toxic $MA_3Bi_2I_9$ based lead-free perovskite solar cells, *TOIN Bulletin*, **2017**, *39*, 149-154.
5. **A. Kulkarni**, T. Singh, A. K. Jena, P. Pinpithak, M. Ikegami, T. Miyasaka, Vapour Annealing Controlled Crystal Growth and Photovoltaic Performance of Bismuth Triiodide Embedded in Mesostructured Configurations, *under revision.*
6. **A. Kulkarni**, A. K. Jena, M. Ikegami, T. Miyasaka, Enhancing the Efficiency and Stability of Lead Free Silver-Bismuth Halide Solar Cells: A Prominent Role of Precursor Solvent, *Manuscript in preparation.*

In Co-author (not related to thesis)

1. A. Jena, **A. Kulkarni**, M. Ikegami, T. Miyasaka, Steady state performance, photo-induced performance degradation and their relation to transient hysteresis in perovskite solar cells, *Journal of Power Source,* **2016**, *309*, 1-10.
2. P. Pinpithak, H.-W. Chen, **A. Kulkarni**, Y. Sanehira, M. Ikegami, T. Miyasaka, Low-Temperature and Ambient Air Processes of Amorphous SnOx-based Mixed Halide Perovskite Planar Solar Cell, *Chem. Lett.*, **2017**, *46 (2)*, 382-384.
3. B. Chaudhary, **A. Kulkarni**, A. K. Jena, M. Ikegami, Y. Udagawa, H. Kunugita, K. Ema, T. Miyasaka, Poly(4-vinylpyridine)-based Interfacial Passivation to Enhance Voltage and

Moisture Stability of Lead Halide Perovskite Solar Cells, *ChemSusChem*, **2017**, *10*, 2473-2479.

4. P. Pinpithak, **A. Kulkarni**, H.-W. Chen, M. Ikegami, T. Miyasaka, Light Harvesting Improvement in Indoline (D149) Based Solid-State Type Dye-Sensitized Solar Cell by Co-Sensitization of Methylammonium Lead Bromide ($MAPbBr_3$), *Bull. Chem. Soc. Jpn.*, DOI: 10.1246/bcsj.20170423.

List of Awards

1. **Award for Encouragement of Research** at 15th International Conference on Advanced Materials (IUMRS-ICAM), Kyoto, Japan, 2017.
2. **Best poster award** at 11th Aseanian Conference on Nano-Hybrid Solar Cells (NHSC-11), Himeji, Japan, 2017.
3. **Best oral presentation award** at Toin BME, 2015.
4. **Best oral presentation award** at Toin BME, 2017.

Grant

Apr. 2017 – Mar. 2019. Japan Society for the Promotion of Science (JSPS) Research Fellowships for Young Scientist (DC2)

List of Conferences (Domestic and International)

1. "Characteristics of Perovskite Solar Cells Based on New Polymer Type Hole Transporting Material" **A. Kulkarni**, H.-W. Chen, M. Ikegami, T. Miyasaka, *Electrochemical Society of Japan (ECS-J)*, **2015** (Oral talk).
2. "Revealing and Reducing The Possible Recombination Loss at FTO/TiO_2 Interface in Perovskite Solar Cell" **A. Kulkarni**, A. Jena, M. Ikegami, T. Miyasaka, *Toin BME*, **2015** (Oral talk).
3. "Role of Thin MgO Layer in Suppressing Interfacial Recombination Loss at FTO-TiO_2 Interface in Perovskite Solar Cells" **A. Kulkarni**, A. Jena, M. Ikegami, T. Miyasaka, *MRS Fall Meeting, Phoenix, Arizona, US* , **2016** (Poster talk).
4. "Lead Free Bismuth Based Perovskite $(CH_3NH_3)_3Bi_2I_9$ for Optoelectronic Applications" **A. Kulkarni**, T. Singh, T. Miyasaka, *1st AP-HOPV*, **2017** (Poster talk).
5. "Bismuth Based Light Absorbing Materials for Photovoltaic Applications" **A. Kulkarni**, M. Ikegami, T. Miyasaka, *Electrochemical Society of Japan (ECS-J)*, **2017**, (Oral talk)
6. "Methylammonium iodobismuth $(CH_3NH_3)_3Bi_2I_9$ Based Materials for Photovoltaic Applications" **A. Kulkarni**, M. Ikegami, T. Miyasaka, *9th International Conference on Materials for Advanced Technologies (ICMAT)*, Singapore, **2017,** (Poster talk)
7. "Non-toxic Bismuth Based Lower and Higher Dimensional Light Absorbing Materials for Photovoltaic Applications" **A. Kulkarni**, T. Miyasaka, *15th International Conference on Advanced Materials (IUMRS-ICAM)*, Kyoto, Japan, **2017** (Oral talk).
8. "Effect of Solvent Engineering and Interfacial Modification of Silver-Bismuth Halide Compound For Efficient Lead Free Perovskite Solar Cells" **A. Kulkarni**, A. Jena, M. Ikegami, T. Miyasaka, *11th Aseanian Conference on Nano-Hybrid Solar Cells (NHSC11)*, Himeji, Japan, **2017** (Poster talk).
9. "Eco-friendly Bismuth Halide and Silver-Bismuth Halide Based Materials for Lead-Free Perovskite Solar Cells" **A. Kulkarni**, M. Ikegami, T. Miyasaka, *27th Photovoltaic Science and Engineering Conference (PVSEC-27)*, **Nov. 2017, Japan,** (Poster talk).
10. "Silver-Bismuth Based Materials for Lead Free Perovskite Solar Cells" **A. Kulkarni**, M. Ikegami, T. Miyasaka, *Toin BME*, Nov. 2017 (Oral talk).

11. "Bismuth Based Perovskite and Non-Perovskite Materials for Lead-Free Solar Cells" **A. Kulkarni**, T. Singh, M. Ikegami, T. Miyasaka, *XIX International Workshop on the Physics of Semiconductor Devices (IWPSD)*, **Dec. 2017, India**, (Oral talk).
12. "Solvent Engineering to Improve the Morphology and Enhance the Conversion Efficiency of Silver-Bismuth Halide Light Absorbing Materials for Efficient Lead Free Perovskite Solar Cells" **A. Kulkarni**, M. Ikegami, T. Miyasaka, *2nd AP-HOPV*, **2018** (Poster talk).